

CHEMICAL CHARACTERIZATION OF MASS-SELECTED IONS BY INFRARED
MULTIPLE PHOTON DISSOCIATION SPECTROSCOPY

By

WARREN KARL MINO, JR

A DISSERTATION PRESENTED TO THE GRADUATE SCHOOL
OF THE UNIVERSITY OF FLORIDA IN PARTIAL FULFILLMENT
OF THE REQUIREMENTS FOR THE DEGREE OF
DOCTOR OF PHILOSOPHY

UNIVERSITY OF FLORIDA

2011

© 2011 Warren Karl Mino, Jr.

To Mom, Dad, Jessica, Jacqueline, Christopher, and Kyle

ACKNOWLEDGMENTS

I would like to thank several people for their support and guidance throughout my graduate career. Thanks go out to my advisor, Nick Polfer, for all his guidance and preparation. His patience, ability to teach, and passion for science have driven my success in graduate school and have made me into the scientist I am today. John Eyler is acknowledged for his advice and guidance. He was always willing to take time to help explain problems that I encountered and was a wonderful mentor. Dave Powell is thanked for the use of his lab and instrument. He was always available for help and willing to teach me about fixing and optimizing the instrument. Thanks to W. Lee Pearson and Jan Szczepanski for their help in understanding and performing experiments early in my graduate career. They both took time from their own experiments to give me guidance and help me perform my experiments successfully. Thanks go out to Robert C. Dunbar (Case Western Reserve University) and Peter B. Armentrout (University of Utah) for their collaborations and helpful discussions. Thanks to the entire Polfer Group, past and present, for their scientific discussions and aid in designing and executing experiments. Finally, thanks to my wife, Kyle, for her editing expertise and captivating scientific conversations.

TABLE OF CONTENTS

	<u>page</u>
ACKNOWLEDGMENTS.....	4
LIST OF TABLES.....	8
LIST OF FIGURES.....	9
ABSTRACT.....	13
CHAPTER	
1 BACKGROUND	16
Introduction	16
Amino Acids	17
Protein Identification	18
Edman Degradation	19
Mass Spectrometry	20
Amino Acid and Peptide Identification	21
Mass Spectrometry (MS).....	21
Electrospray ionization (ESI).....	22
Tandem mass spectrometry.....	23
Infrared multiple photon dissociation (IRMPD).....	24
Infrared Multiple Photon Dissociation Spectroscopy	25
Overview.....	25
2 INSTRUMENTATION	31
Introduction	31
Fourier Transform Ion Cyclotron Resonance Mass Spectrometry	31
History	31
Fourier Transform Ion Cyclotron Resonance Theory	33
Cyclotron motion	33
Mass detection.....	35
Trapping motion	36
Magnetron motion	36
Space charge effects	37
Fourier Transform Ion Cyclotron Resonance Instrumentation.....	38
Ion optics and vacuum system.....	39
Magnet.....	40
Analyzer cell.....	40
Data system	41
Instrumentation Operation.....	41
Quadrupole Mass Filter, Quadrupole Ion Trap, Time-of-Flight Mass Spectrometer	45

Quadrupole Mass Filter Theory	45
Quadrupole Ion Trap	48
Time-of-Flight Mass Spectrometry	51
Optical Parametric Oscillator Lasers.....	52
History	53
Optical Parametric Oscillator Theory.....	54
Nonlinear optics	54
Periodic poling	57
Resonance cavity.....	57
OS 4000 Alignment	59
OS 4000 Operation	62
Carbon Dioxide Lasers	63
Carbon Dioxide Laser Operation	63
3 VIBRATIONAL SIGNATURE OF ZWITTERIONIC AND CHARGE-SOLVATED STRUCTURES FOR ALKALINE EARTH TRYPTOPHAN DIMER COMPLEXES IN THE GAS PHASE	74
Introduction	74
Procedure	76
Materials	76
Mass Spectrometry and Ion Spectroscopy	77
Calculations.....	79
Results and Discussion.....	80
Experimental Optimization.....	80
Ba ²⁺ Tryptophan Monomer Complex.....	81
Alkaline Earth Tryptophan Dimer Series	84
Ba ²⁺ Tryptophan Dimer Complex	86
Ca ²⁺ Tryptophan Dimer Complex	88
Metal Binding Effects on Z Stabilization	90
Conclusions	92
4 VIBRATIONAL SIGNATURE OF ZWITTERIONIC AND CHARGE-SOLVATED STRUCTURES FOR ALKALINE EARTH METHIONINE DIMER COMPLEXES IN THE GAS PHASE	103
Introduction	103
Experimental	105
Materials	105
Mass Spectrometry and Photodissociation.....	105
Calculations.....	106
Results and Discussion.....	108
Ba ²⁺ Methionine Monomer Complex.....	108
Alkaline Earth Methionine Dimer Series	109
Mg ²⁺ Methionine Dimer Complex	110
Ca ²⁺ Methionine Dimer Complex	111
Ba ²⁺ Methionine Dimer Complex	112

Comparison of Methionine and Tryptophan.....	112
Conclusions	114
5 INFRARED MULTIPLE PHOTON DISSOCIATION SPECTROSCOPY OF IONS IN PENNING AND QUADRUPOLE ION TRAPS	126
Introduction	126
Experimental.....	127
Materials.....	127
Mass Spectrometry and Ion Spectroscopy	127
Penning trap.....	128
Custom-built instrument equipped with a quadrupole ion trap	128
Calculations.....	134
Results and Discussion.....	135
Laser Set-up in the Penning trap.....	135
Effect of Trapping Condition on IRMPD	136
Dual-laser IRMPD yield	138
Protonated Tryptophan IRMPD Spectrum in the Penning Trap.....	139
Protonated Tryptophan IRMPD Spectrum in the Quadrupole Ion Trap	140
IRMPD of the $[Trp+H-NH_3]^+$ Fragment Ion	144
IRMPD of the $[Trp+H-NH_3-CH_2CO]^+$ Fragment Ion.....	145
Conclusions	146
6 STRUCTURAL ELUCIDATION OF METAL-TAGGED PEPTIDES VIA LOW- ENERGY RESONANT COLLISION-INDUCED DISOOCIATION	167
Introduction	167
Slow Heating Techniques.....	167
Disulfide Bond Cleavages in Mass Spectrometry.....	168
Rationale for Experiments	169
Experimental.....	169
Results and Discussion.....	170
Nomenclature	170
Product Ions From CID Spectra	171
Neutral loss from the precursor ion (1).....	172
Fragmentation from the peptide backbone tail (2).....	173
Cleavage of the disulfide bridge (3)	173
Loss of internal amino acids through b/y fragmentation (4)	174
Conclusions	175
7 CONCLUSIONS AND FUTURE DIRECTIONS	186
LIST OF REFERENCES	189
BIOGRAPHICAL SKETCH.....	201

LIST OF TABLES

<u>Table</u>		<u>page</u>
4-2	Relative product ion intensities for the alkaline earth complexed series of tryptophan and methionine.....	123
5-1	Water cluster absorption bands for the signal and idler beams of the optical parametric oscillator laser.....	152
5-2	Summary of centroid band positions and spectral assignments for the experimental IRMPD spectra.....	157
5-3	Electronic, zero-point corrected and Gibbs free energies calculated by density functional theory.....	159
6-1	Relative product ion intensities for the five CID spectra of oxytocin.....	185
6-2	Relative ion intensities for the five CID spectra of oxytocin	185

LIST OF FIGURES

<u>Figure</u>		<u>page</u>
1-1	The twenty standard amino acids grouped by polarity and charge.....	27
1-2	Amino acid chemical structure in the presence of a polar solvent.....	28
1-3	Illustration of the Edman degradation process.....	28
1-4	Flow chart for mass spectrometry in proteomics.	29
1-5	Illustration of an electrospray ionization source.....	29
1-6	Illustration of the infrared multiple photon dissociation mechanism.....	30
2-1	The cyclotron motion of negative and positive ions in a uniform magnetic field.....	65
2-2	Illustration of the different excitation experiments that can be performed in the ion cyclotron resonance cell.	65
2-3	Motion of ions in an ion cyclotron resonance mass spectrometer.	66
2-4	An illustration of the basic components of the Bruker Apex II Fourier transform ion cyclotron resonance mass spectrometer.....	66
2-7	Screenshot from Xmass™ software workflow to illustrate basic components of experiment.....	68
2-8	A schematic of a quadrupole mass filter.....	68
2-9	Stability diagram of a linear quadrupole mass filter.	69
2-10	Schematic of a quadrupole ion trap.....	69
2-11	Stability diagram of the quadrupole ion trap.	70
2-12	Visualization of the electric field applied in the quadrupole ion trap.....	70
2-13	Cartoon illustrating the general operation of the optical parametric oscillator laser.....	71
2-14	Photograph of the optical parametric oscillator cavity.....	72
2-15	Plot of signal (top) and idler (bottom) wavelength dependence on temperature of the crystal through all the poling periods of the OPO laser.	73
3-1	Four of the lowest-energy calculated structures for the Ba ²⁺ Trp complex.	93

3-2	Three lowest-energy calculated structures for the $M^{2+}Trp_2$ complex.....	94
3-3	Fragmentation yield dependence on OPO irradiation time for the $Ba^{2+}Trp$ monomer irradiated at 3328 cm^{-1}	95
3-4	Comparison of the dissociation yield of $Ba^{2+}Trp$	96
3-5	Mass spectra of $Ba^{2+}Trp$ after isolation (top) and after MS/MS (bottom).....	97
3-6	IRMPD spectrum of $Ba^{2+}Trp$ ($3000\text{-}3700\text{ cm}^{-1}$) with calculated vibrational spectra.....	98
3-7	IRMPD spectra of the $M^{2+}Trp_2$ alkaline earth series in N-H and O-H stretching regions.....	99
3-8	Tandem mass spectra of the $M^{2+}Trp_2$ where $M=Mg, Ca, Sr,$ and Ba	100
3-9	IRMPD spectra of $Ba^{2+}Trp_2$ with calculated vibrational spectra for the two lowest-energy conformers.....	101
3-10	IRMPD spectra of $Ca^{2+}Trp_2$ with calculated vibrational spectra for the three lowest-energy conformers.....	102
4-1	Nine of the lowest-energy calculated structures for the $M^{2+}Met$ monomeric complex.....	116
4-2	Screenshot of Gabedit program, showing $Ba^{2+}Met$ Z conformer.....	117
4-3	IRMPD spectra of the Ba^{2+} methionine complex over the 3200 cm^{-1} to 3650 cm^{-1} range.....	118
4-4	IRMPD spectra of the alkaline earths complexed with the methionine dimer in the N-H and O-H stretching regions.....	119
4-5	IRMPD mass spectra of $M^{2+}Met_2$ under conditions of maximum IRMPD yield.....	120
4-6	IRMPD spectrum of $Mg^{2+}Met_2$ in the hydrogen stretching region along with calculated vibrational spectra for the four lowest-energy conformers.....	121
4-7	IRMPD spectra of $Ca^{2+}Met_2$ in the hydrogen stretching region along with calculated vibrational spectra for the three lowest-energy conformers.....	122
4-8	IRMPD spectra of $Ba^{2+}Met_2$ in the hydrogen stretching region along with calculated vibrational spectra for the three lowest-energy conformers.....	123
4-9	Plot of the photofragmentation pathways relative to the complexed metal ion ionic radius.....	124

4-10	Cartoon of the energy wells and barriers for dissociation chemistry of each metal amino acid complex.....	125
5-1	Illustration of the OPO and CO ₂ lasers tethered to the QIT of a custom built instrument.....	148
5-2	Schematic of the timing events used for the IRMPD experiments in the QIT ..	149
5-3	Illustration of the mass spectrometric methods for both the custom built and commercial FT-ICR instruments.....	149
5-4	Screenshot of the data analysis software built in LabVIEW.	150
5-5	Set-up of the OPO and CO ₂ lasers tethered to the Penning trap of a FT-ICR mass spectrometer.....	151
5-6	Illustration of the effect of changing the trapping voltages on the potential field in the Penning trap.....	153
5-7	Plot of the change in reduced trapping potential versus the measured ion abundance in the Penning trap.....	153
5-8	A plot of fragmentation yield of the Ba ²⁺ Met complex versus the trapping potential.....	154
5-9	A plot of the IRMPD yield of the Ba ²⁺ Met complex versus the irradiation time for experiments using the OPO laser alone or using a combination of the OPO and CO ₂ lasers.....	154
5-10	The full experimental IRMPD spectrum of TrpH ⁺ from 2950 cm ⁻¹ to 3650 cm ⁻¹ recorded in the Penning trap of the FT-ICR mass spectrometer..	155
5-11	The full experimental IRMPD spectrum of TrpH ⁺ from 2950 cm ⁻¹ to 3650 cm ⁻¹ recorded in the QIT of the custom built mass spectrometer..	156
5-12	Experimental IRMPD spectrum of TrpH ⁺ recorded in the QIT compared computational spectra.	158
5-13	Experimental IRMPD spectrum of TrpH ⁺ recorded in the QIT compared computational spectra.	160
5-14	The mass spectrum of TrpH ⁺ (a) without and (b) with laser irradiation.	161
5-15	Experimental IRMPD spectra of TrpH ⁺ , [Trp+H-NH ₃] ⁺ , and [Trp+H-NH ₃ -CH ₂ CO] ⁺	162
5-16	Experimental IRMPD spectrum of [Trp+H-NH ₃] ⁺ compared to the computational spectra of the lowest energy structural conformers.....	163

5-17	Schematic representation of suggested dissociation pathways for NL of NH ₃ from the precursor TrpH ⁺ ion (<i>m/z</i> 205 → <i>m/z</i> 188).....	164
5-18	Experimental IRMPD spectrum of [Trp+H-NH ₃] ⁺ compared to the computational spectra of the lowest energy structures.....	165
6-1	Illustration of a multiple-quadrupole ToF-MS instrument.	177
6-2	Diagram of possible cleavages along a peptide backbone labeled with Roepstorff-Fohlman-Biemann nomenclature.....	178
6-3	Low amplitude multiple resonance excitation CID tandem mass spectrum of [OT+2H] ²⁺	179
6-4	Low amplitude multiple resonance excitation CID tandem mass spectrum of [OT+Cu ²⁺] ²⁺	180
6-5	Low amplitude multiple resonance excitation CID tandem mass spectrum of [OT+Zn ²⁺] ²⁺	181
6-6	Low amplitude multiple resonance excitation CID tandem mass spectrum of [OT+Fe ²⁺] ²⁺	182
6-7	Low amplitude multiple resonance excitation CID tandem mass spectrum of [OT+Fe ³⁺ -2H] ⁺	183
6-8	An overview of typical fragmentation observed in CID of metal-complexed OT	184

Abstract of Dissertation Presented to the Graduate School
of the University of Florida in Partial Fulfillment of the
Requirements for the Degree of Doctor of Philosophy

CHEMICAL CHARACTERIZATION OF MASS-SELECTED IONS BY INFRARED
MULTIPLE PHOTON DISSOCIATION SPECTROSCOPY

By

Warren Karl Mino, Jr

May 2011

Chair: Nick C. Polfer

Major: Chemistry

Infrared multiple photon dissociation (IRMPD) spectroscopy is a powerful tool in identifying ion structures in mass spectrometry. In recent years, most IRMPD studies have been conducted at free electron laser (FEL) facilities, which offer tunability and high spectral brightness over the mid-IR range (500-2000 cm⁻¹). Here, we implement a tunable benchtop optical parametric oscillator (OPO) laser in combination with trapping mass spectrometers to carry out IRMPD spectroscopy in the hydrogen stretching range (3000-4000 cm⁻¹). In the Penning trap of a Fourier transform ion cyclotron resonance mass spectrometer, more weakly bound metal-chelated amino acid complexes can be successfully photodissociated. For a series of group II metals (Mg²⁺ – Ba²⁺) complexed with the amino acids tryptophan (Trp) and methionine (Met), the O-H and N-H stretching vibrations readily allow distinction between the zwitterionic (Z) (i.e., NH₃⁺-CHR-CO₂⁻) and charge solvated (C) (i.e., NH₂-CHR-COOH) forms of the amino acid (where R denotes the side chain). It is thus determined that for the M²⁺(Trp)₂ dimers, the smaller cations favor the Z form. Conversely, for the M²⁺(Met)₂ dimers, the opposite trend is observed. These trends are complemented by quantum-chemical calculations to

rationalize the findings. It is proposed that the bulky indole side chain in tryptophan accounts for the unusual trend in favoring Z structures for smaller cations.

The IRMPD yield is shown to be increased by irradiating the ion cloud with a second non-resonant CO₂ laser at a fixed frequency of 10.6 μm, following OPO laser irradiation. Moreover, the trapping voltages of the Penning trap can be adjusted to improve the overlap between the ion cloud and the laser beam, and hence enhance the IRMPD yield. These approaches are found to be particularly useful in boosting the IRMPD yield of weaker modes. Nonetheless, photodissociation of more strongly-bound ions is found to be much more challenging.

A custom-built mass spectrometer is presented, where the ions are irradiated in a reduced pressure (10⁻⁵ mbar) “Paul-type” quadrupole ion trap (QIT). The compact ion cloud is subjected to focused laser beams. Comparison of IRMPD of protonated tryptophan in the Penning and Paul traps shows that required laser irradiation times are considerably shorter and that weaker modes become visible. Furthermore, the fragmentation pathways of protonated tryptophan in collision-induced dissociation conditions are interrogated by IRMPD spectroscopy, assisted by quantum-chemical calculations. The loss of NH₃ is shown to be mediated by a nucleophilic attack from carbon C3 on the indole side chain. The subsequent CH₂CO loss product is also structurally characterized.

These results demonstrate that strongly-bound ions and reaction products from collision-induced dissociation in particular, can now be routinely characterized by IRMPD spectroscopy using a benchtop infrared laser. It is expected that these developments will make the technique of IRMPD spectroscopy more accessible to the

wider mass spectrometry community, as opposed to being limited to a few user facilities.

CHAPTER 1 BACKGROUND

Introduction

Mass spectrometry (MS) has become an indispensable analytical tool in the biosciences. While knowledge of the mass of a compound usually does not allow unambiguous identification, there is an array of fragmentation techniques that aid in structural identification. Electron capture dissociation,^{1,2} electron transfer dissociation,³⁻⁵ collision induced dissociation,⁶⁻⁸ and infrared multiple photon dissociation (IRMPD)⁹ have been shown to be particularly useful in the structural analysis of peptides and proteins. The structure of the precursor ion can then be “pieced together” based on the fragmentation products. However, a limiting factor of these approaches is that the structural information is rather indirect. Specifically, in the dissociation mechanism, rearrangement processes may take place that could alter the original structure. Further, different precursor structures may nonetheless give rise to the same fragment masses.

In order to obtain more direct information, techniques are required that probe an inherent property of the precursor ion. In infrared multiple photon dissociation (IRMPD) spectroscopy a tunable infrared (IR) laser is employed to induce photodissociation.¹⁰⁻¹⁴ As the absorption of multiple photons is mediated by the vibrational resonance, the IRMPD spectrum is a reflection of the infrared absorption spectrum of the ion.¹⁵ The vibrational spectrum carries information on the presence (or absence) of chemical groups, the location of the charge (e.g. proton) and hydrogen bonding interactions, and can hence serve as an important benchmark for structural information in addition to the mass information.

Amino Acids

Chemical knowledge of amino acids is essential to understanding biochemistry, since amino acids are the basic building blocks of peptides, polypeptides and proteins. The twenty standard amino acids are depicted in Figure 1-1. They are all similar in that they contain two functional groups, an amine group (NH_2) and an acidic group (COOH) and differ by their side chain. The side chain is often denoted as each amino acid's 'R group', which is attached to the alpha carbon. The carboxylic acid is labeled carbon one, the alpha carbon is carbon two, and subsequent carbons are labeled along the R group. The structure of the amino acids described above and shown in Figure 1-1 is known as charge solvated (C); however, in the presence of a polar solvent, such as water, an amino acid exists as a zwitterion (Z), where the proton from the carboxylic acid is shifted to the amine group, giving a net negative charge on the carboxylic acid group and net positive charge on the amine (i.e., the overall charge on the molecule is neutral). An example of the difference between Z and C can be seen in Figure 1-2.

The twenty standard amino acids are sub-divided into four classes: nonpolar-aliphatic, aromatic polar-uncharged, polar-positively charged, and polar-negatively charged. The nonpolar-aliphatic amino acids are glycine, alanine, valine, leucine, isoleucine, and methionine. Because they are nonpolar, they typically work to stabilize protein structure via hydrophobic interactions. The aromatic amino acids are phenylalanine, tyrosine, and tryptophan. Just as the nonpolar aliphatic amino acids, these tend to exist in the interior of proteins for stabilization. The polar uncharged amino acids are serine, threonine, cysteine, proline, asparagine, and glutamine. Although they are uncharged, most have a lone pair of electrons that is available for hydrogen bonding interactions. Cysteine can also readily oxidize to dimerize with another cysteine to form

a disulfide bond. Disulfide bonds are strongly hydrophobic and play a key role in linking within peptides/proteins or two separate peptide/protein chains. Positively charged amino acids are lysine, arginine, and histidine. Due to their inherent hydrophilicity, they are often found on the surface of proteins. Furthermore, histidine is known to be a key component in hemoglobin, involved in the exchange of CO₂ and O₂. The last group is the negatively charged amino acids, aspartate and glutamate. They are involved in cell transport and also have a role in neurotransmitters. Amino acids are involved in many different biological functions, especially involving metal complexation.

Protein Identification

A protein is made up of polypeptides, each of which is composed of amino acid residues that uniquely define the protein and its corresponding function. By convention, a protein's amino acid sequence is given from N-terminus to C-terminus, terminated by an amine and a carboxylic acid, respectively.¹⁶ The amino acid sequence of protein is determined by the genetic information encoded by DNA (deoxyribonucleic acid). The human genome project, which officially began in 1990, amassed a wealth of knowledge on the blueprint of the human genome in efforts to develop medication and health care. Among genetic information, predicted protein expression was also investigated and is available in DNA/protein databases.

Although the human genome project discovered the genes that underpin human life, it is proteins that are responsible for the majority of cellular activities and biological functions.¹⁷ The general study of protein structure and function, and how they are related, is defined as proteomics.^{18,19} Proteomics has gained significant attention as it is a natural progression from understanding the human genome. Therefore, it is becoming increasingly important to be able to identify proteins in highly complex biological

systems. Thus, analytical techniques are required to structurally identify protein structure.

The two analytical techniques associated with protein identification are Edman degradation and mass spectrometry (MS). Edman degradation pioneered protein identification;^{20,21} however, it was later replaced by MS with the development of two soft ionization methods, electrospray ionization (ESI)²² and matrix assisted laser desorption/ionization (MALDI).^{23,24} These methods allow for large, nonvolatile analytes to be ionized and brought into the gas-phase without unwanted fragmentation. MS offers many analytical advantages over Edman degradation—it is more sensitive, has a faster cycle time, does not require purification, and is not hindered by blocked or modified proteins.

Edman Degradation

Edman degradation was developed by Pehr Edman in 1950 to systematically cleave the amide bond of a peptide or protein in order to identify the sequence.²⁰ The general mechanism is illustrated in Figure 1-3. In this method, phenylisothiocyanate reacts with a terminal alpha amino group of a peptide or protein to generate a phenylthiocarbamyl adduct. Under acidic conditions, the sulfur group from the phenylthiocarbamyl adduct attacks the carbonyl component of the closest amide bond, resulting in specific cleavage. The resulting fragment is then extracted by organic solvent and identified by ultra-violet absorption spectroscopy. The remaining peptide or protein is exposed to the same procedure, resulting in step-wise sequence identification.

The Edman degradation process was significantly improved in 1973 when it was automated by Huge Niall²¹ and it was the primary analytical technique for protein identification until the 1990's.

Mass Spectrometry

Since the 1990's mass spectrometry (MS) has replaced Edman degradation as the most popular analytical tool for peptide/protein identification in biological samples.²⁵ Comparatively, MS is more sensitive; it can identify a single peptide in as little as a few seconds, and does not require a purification step for analysis. These figures of merit, along with developments in computational approaches, have led a surge in biological MS.

The basic procedure for MS within proteomics is illustrated in Figure 1-4. The process begins by removing proteins from a biological sample by sodium dodecyl sulfate polyacrylamide gel electrophoresis (SDS-PAGE). Bands of protein aggregates that are unique to individual proteins are formed in the gel. The individual bands are removed and enzymatically digested into peptides. These peptides are the building blocks of the protein and are ionized by ESI or MALDI for mass analysis. It should be noted that a purification step is not required; however, further separation by liquid chromatography is often performed to reduce sample complexity. The ionized peptides are analyzed by the mass spectrometer, isolated, and subjected to tandem MS, where the isolated peptide is broken into smaller pieces for analysis. The information generated from the broken peptide contains sequence specific information that can be used to identify the peptide under investigation.²⁵ Furthermore, the peptide-sequencing information generated for all the peptides from the protein can be compared with mass

spectra from online protein databases using one of a number of database-searching programs.²⁵

The aforementioned method is classified as the ‘bottom-up’ approach, as the peptide sequencing information identified by MS gives rise to the identification of the initial protein. Although this approach is applicable to all mass analyzers, challenges remain—the identification of a protein depends on complete identification of every peptide in the protein. Peptides with low ionization efficiencies may not be detected, thus correct assignments are not possible.^{26,27} Alternative approaches, such as ‘top-down’ approaches, are also possible. In this case, an entire protein is fragmented in the mass spectrometer.^{1,28-30} However, given the complexity of the mass spectra, high resolution and high mass accuracy MS is required. Thus, the ‘bottom-up’ approach remains the most popular method for protein identification.

Amino Acid and Peptide Identification

The identification of amino acids and peptides is crucial to the identification of a protein. Thus, understanding the fragmentation chemistry of amino acids and peptides can aid in the development of the ‘bottom-up’ approach. This section will focus on the work flow of the mass spectrometric technique, including general concepts and theory of mass spectrometry as well as fragmentation techniques and structural identification methods.

Mass Spectrometry (MS)

Mass spectrometry (MS) is one of the most widely used analytical techniques. This technique can perform elemental analysis of samples, structural interrogation of any type of analyte, qualitative and quantitative analysis of complex mixtures, and isotopic ratios elucidation of atoms in a sample.³¹ A typical mass spectrometer is composed of

three main components: an ionization source, a mass analyzer and a detector. The ionization source is used to generate analyte ions and introduce them into the mass spectrometer. Typically, ion optics are used to guide the analyte ions to be measured by the mass analyzer, the measurement results in the identification of an analyte ion's mass-to-charge ratio (*m/z*). Finally, a detector is used to measure the abundance of each ion at a specific *m/z* value. The abundance versus the *m/z* is then plotted to generate a mass spectrum.

Electrospray ionization (ESI)

Since the implementation of electrospray ionization (ESI) in mass spectrometry by Fenn et al. in 1984,²² the field of biological mass spectrometry has become increasingly popular.³²⁻³⁴ ESI offers the advantage that it can be coupled with separation techniques. For example capillary electrophoresis (CE) and high performance liquid chromatography (HPLC) are suitable for the separation of small organic/inorganic molecules/complexes, peptides, proteins, DNA, and synthetic polymers. In addition to ESI, matrix-assisted laser desorption/ionization (MALDI) was introduced in 1991 by Hillenkamp et al. for the analysis of biomolecules.²³ Both ionization techniques are capable of transferring intact, large molecules to the gas-phase; however, ESI was the only ionization source used for this work and will be the focus of this section.

ESI is one of the softest ionization techniques available and is capable of transferring intact macromolecules (>1 MDa) into the gas phase.^{22,35} The process begins with an analyte dissolved ($\sim 10^{-3} - 10^{-6}$ M) in a volatile solution (e.g., 50:50 methanol:H₂O). Figure 1-5 is an illustration of a typical ESI set-up. The solution is pumped through a small needle tip in the low microliter per minute range and is positioned to flow toward (or orthogonal to) a capillary entrance into a mass

spectrometer. A high voltage drop is applied between the capillary entrance and the needle, typically on the order of 3–4kV. The large electric field induced by the high potential causes the solution leaving the needle to form a Taylor cone, which emits droplets of the analyte containing solvent.³⁶ Only a small percentage of the droplets actually make it into the entrance of the capillary and continue on into the mass spectrometer. The capillary is typically heated to promote desolvation as the droplets travel into the mass spectrometer. The solvent evaporation causes the droplets to undergo Rayleigh explosions; this is due to the Columbic repulsion overcoming the surface tension of the solvent droplets. The desolvation process can be enhanced by a heated nebulizing gas, typically N₂.^{37,38} The process of desolvation and Rayleigh explosions continues until the analyte is brought into the gas phase. The final step of the ionization mechanism is still not completely understood, but it is generally accepted that small ions may be able to escape the solvent surface; whereas larger ions require that all solvent molecules be evaporated.^{39,40}

Tandem mass spectrometry

Once in the gas-phase, charged analyte ions generated by the ESI source are guided toward the mass analyzer. The mass analyzer, briefly, will separate the ions based on mass-to-charge (*m/z*) so they can be detected. Further detail of the mass analyzer instrumentation will be discussed in Chapter 2. The mass analyzer can be operated in different modes, depending on the information needed from the sample. The mass analyzer can measure all of the ions in a sample, or a single ion can be isolated and measured. Furthermore, if more chemical information is required from a sample, ions can be fragmented and measured through multiple stages of mass spectrometric selection; this process is referred to as tandem mass spectrometry (MS).

All tandem MS experiments in the work reported here were performed in product ion scan mode. In this mode, a precursor ion is isolated from all other ions generated from the ESI source. The isolated precursor undergoes a fragmentation process and all product ions are measured by the mass analyzer. Other tandem MS methods exist,^{17,41} such as precursor ion scan, neutral loss scan,⁴² and selected reaction monitoring;³⁶ however, these techniques were not performed in this research and will not be discussed here.

Infrared multiple photon dissociation (IRMPD)

Infrared multiple photon dissociation (IRMPD) is a useful fragmentation method for trapped ions.⁴³ Since IRMPD was first demonstrated by Beauchamp et al. with CO₂ lasers in the late 1970's,^{10,44,45} it has grown as an alternative to traditional collision induced dissociation. IRMPD involves tethering infrared lasers, in our case, both a carbon dioxide laser and optical parametric oscillator laser, to the trapping component of a mass spectrometer. The IR laser is directed into the vacuum chamber of a mass spectrometer through an IR transmissive window (e.g., ZnSe) to overlap the laser beam with the ion cloud. The mechanism of fragmentation is illustrated in Figure 1-6.

IRMPD utilizes the inherent property that ions absorb energy, via interactions with IR photons, based on the inherent characteristics of the ions.⁹ In order to absorb a photon, the frequency of the light must be in resonance with a vibrational mode of the analyte ion. Upon absorption, the ion can undergo intramolecular vibrational redistribution (IVR),^{11,46-48} where the energy is rapidly randomized throughout all of the normal modes of the ion.¹² This recycling of the ground vibrational state is crucial in allowing efficient absorption of subsequent photons at the fundamental frequency. Since the dissociation requires the absorption of multiple infrared photons, given that mid-IR

photons contain anywhere between 0.1 to 0.5 eV per photon, historically only CO₂⁴⁹⁻⁵¹ and recently free electron lasers (FELs),⁵² have been employed. Over the course of many milliseconds, sufficient amounts of energy can be pumped into the molecule via IR absorption (mediated by IVR), resulting in dissociation of the ion.

Infrared Multiple Photon Dissociation Spectroscopy

Infrared multiple photon dissociation (IRMPD) spectroscopy¹⁰⁻¹⁴ makes use of the sequential photon absorption mechanism used in multiple photon dissociation, but goes a step further and measures the dissociation yield as a function of irradiation frequency. Since the dissociation yield is related to the efficiency of IR absorption, an IRMPD spectrum can be thought as an indirect measure of an IR absorption spectrum. Anharmonic coupling of normal modes ($\nu=0$) with other modes in the excited state of the ion can result in a red shift of a band, complicating the interpretation of the IRMPD spectrum. However, numerous experiments have shown that the photodissociation spectra can be compared to calculated linear absorption spectra, in order to obtain chemically specific information.⁵³

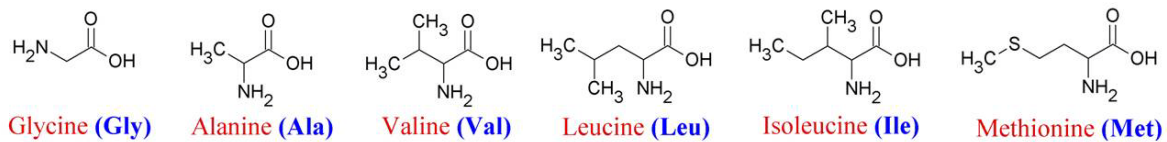
Direct absorption spectroscopy cannot be performed on ions trapped in a mass spectrometer, due to the inherently low concentration of ions. Thus, IRMPD spectroscopy offers an alternative method to performing IR spectroscopy on gas-phase ions. Furthermore, in addition to yielding chemical information from IR active components, IRMPD spectroscopy results in dissociative information that can be used to identify gas-phase structure of the analyte ions.

Overview

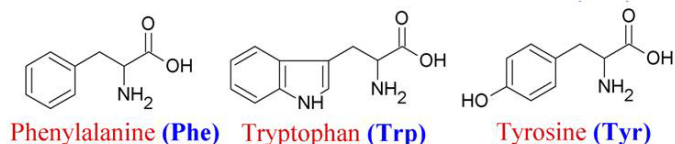
The objective of this research was to illustrate the use of IRMPD spectroscopy for gas-phase structural analysis of biologically relevant analytes. Chapter 2 introduces the

instrumentation used for all experiments: a Fourier transform ion cyclotron resonance mass spectrometer and a custom built mass spectrometer—consisting of a quadrupole mass filter, quadrupole ion trap, and time-of-flight mass analyzer. Chapter 2 also examines the irradiation sources used for the IRMPD experiments, specifically an optical parametric oscillator (OPO) and a CO₂ laser. Chapter 3 demonstrates the application of IRMPD spectroscopy to the amino acid tryptophan in the N-H and O-H stretching regions (3000 cm⁻¹ through 3700 cm⁻¹). This allows a distinction between zwitterionic (Z) or non-zwitterionic (charge-solvated, C) structures in the presence of metals in the gas-phase. Chapter 4 investigates the effect of metal size on the stabilization of Z structure for methionine complexes. The experiments in Chapter 5 focus on the comparison of IRMPD spectroscopy in the Penning trap of the FT-ICR and the quadrupole ion trap of the custom built instrument. Protonated tryptophan was used as a standard analyte to compare the IRMPD efficiency on both instruments. In addition to the comparison of instruments, the dissociation pathway of protonated tryptophan was investigated on the custom built instrument. Investigation of dissociation through a simple system, such as tryptophan, can yield information on dissociation through larger systems, such as peptides, Chapter 6 investigates the effect of metals on the dissociation pathways of peptides in the gas-phase. Specifically oxytocin was complexed with Cu²⁺, Zn²⁺, Fe²⁺, and Fe³⁺, which yielded different fragmentation information for each complex. Future application of IRMPD spectroscopy on peptides will also be discussed here. Chapter 7 summarizes the research completed in this dissertation.

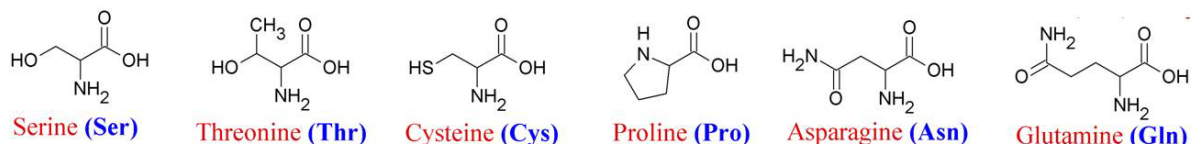
Nonpolar Aliphatic R Groups



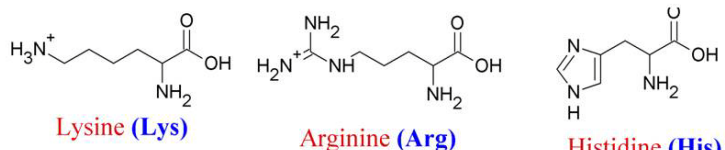
Aromatic R Groups



Polar Uncharged R Groups



Positively Charged R Groups



Negatively Charged R Groups

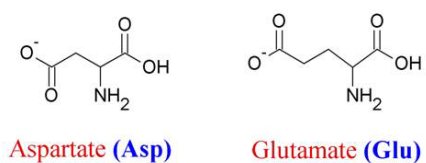


Figure 1-1. The twenty standard amino acids grouped by polarity and charge.

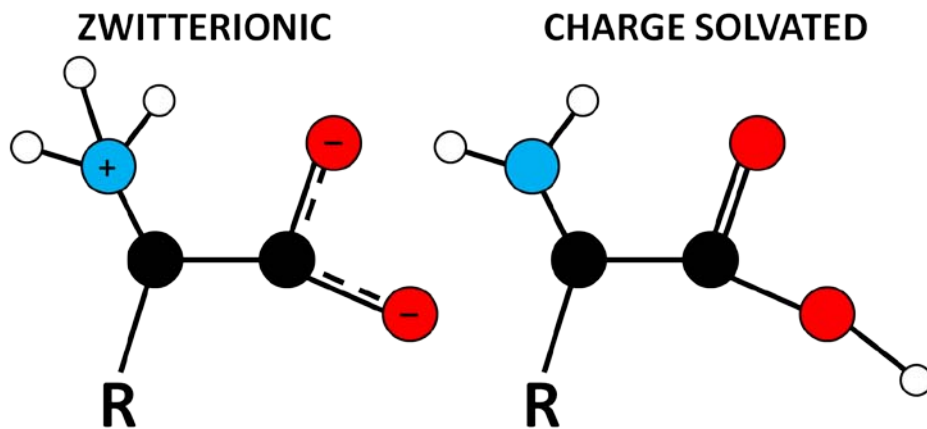


Figure 1-2. Amino acid chemical structure in the presence of a polar solvent, (zwitterionic - Z) or in the absence of a polar solvent (charge-solvated, nonzwitterionic - C)

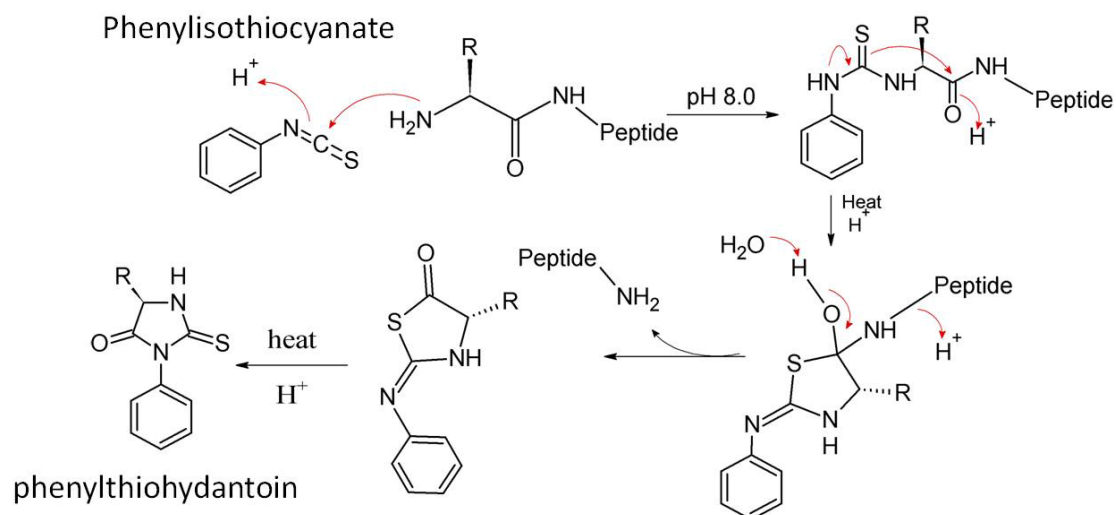


Figure 1-3. Illustration of the Edman degradation process.

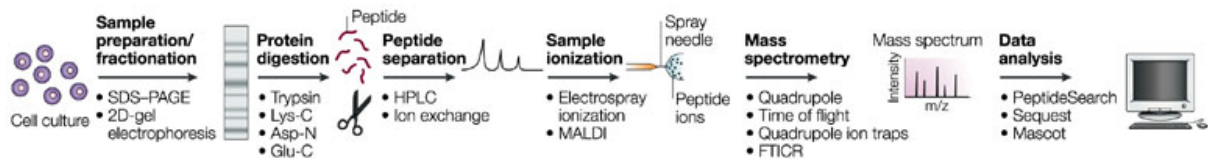


Figure 1-4. Flow chart for mass spectrometry in proteomics. [Reprinted with permission from Nature Publishing Group. Steen, H.; Mann, M.; 2004. The abc's (and xyz's) of Peptide Sequencing. *Nature Rev. Mol. Cell Biol.* (Volume 5, Page 700, Figure 1)]

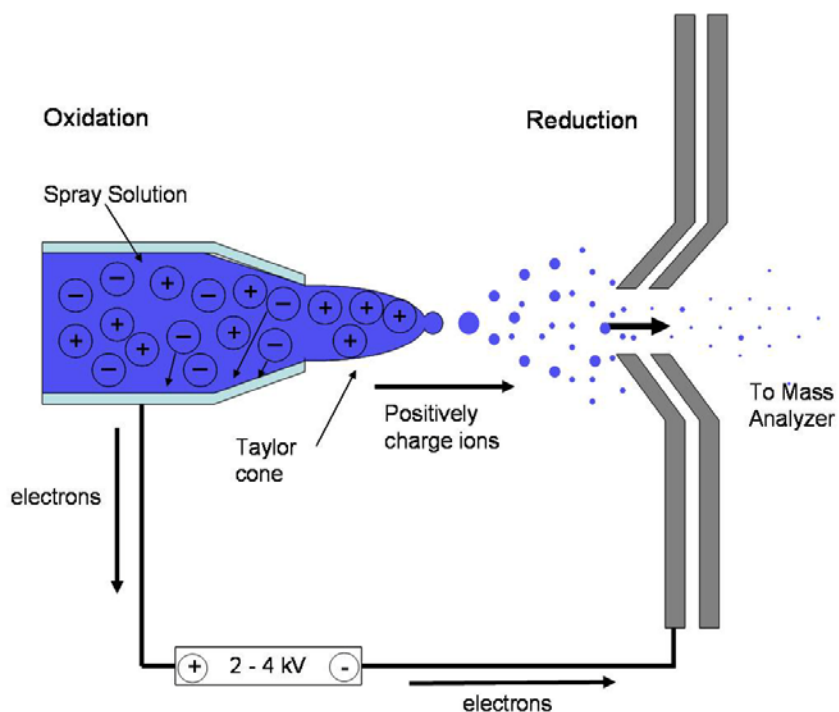


Figure 1-5. Illustration of an electrospray ionization source.

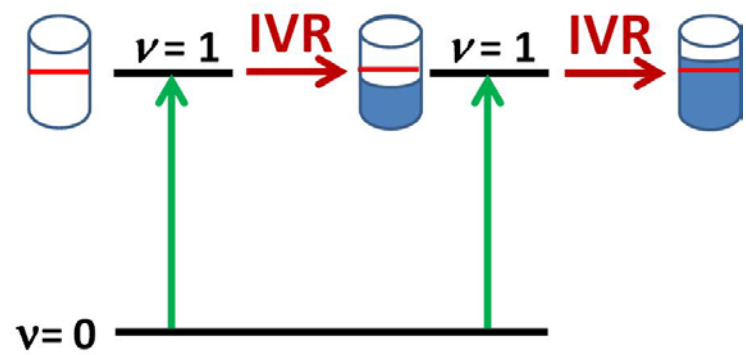


Figure 1-6. Illustration of the infrared multiple photon dissociation mechanism.

CHAPTER 2 INSTRUMENTATION

Introduction

This chapter will focus on the history, theory and general operation of the instrumentation used for the experiments presented in this dissertation. The instrumentation focus will be primarily on Fourier transform ion cyclotron resonance (FT-ICR) and optical parametric oscillator (OPO) lasers; however, fundamentals of quadrupole mass filters, three-dimensional ion traps, time-of-flight (ToF) mass spectrometers, and CO₂ lasers will also be covered.

Fourier Transform Ion Cyclotron Resonance Mass Spectrometry

Fourier transform ion cyclotron resonance (FT-ICR) mass spectrometry (MS) is the premier mass spectrometry technique, because of its ultra-high mass resolution and mass accuracy. Furthermore, with the evolving development in superconducting magnets, mass range, resolution and accuracy capabilities are constantly improving.

History

The development of the FT-ICR mass spectrometer has its roots in the seminal work by Ernest O. Lawrence and Stanley M. Livingston in 1932, where they demonstrated that the circular angular frequency of ions moving perpendicular to a constant magnetic field, or cyclotron motion, is independent of the radius the ion is traveling.⁵⁴ This phenomenon is described by the following equation:

$$\omega_c = \frac{qB}{m} \quad (2-1)$$

In equation 2.1, the cyclotron angular frequency, ω_c , is solely dependent on the ions charge, q , and mass, m , and the applied magnetic field, B . Ions can be either positively or negatively charged, and will move clockwise or counter-clockwise,

respectively, to the perpendicular magnetic field directed upwards from the paper. This principle is especially relevant for mass spectrometry, because at a constant magnetic field, frequency of motion can be directly correlated with m/z .

Lawrence et al. also demonstrated that the cyclotron motion of an ion can be excited to a larger orbital radius, without changing the cyclotron frequency, by applying a transverse alternating electric field of the same frequency as the ion's cyclotron frequency.⁵⁴ It was from this discovery that the first ICR based mass spectrometer was developed. Measurement of the first mass spectrum was done by exciting the ions at a fixed frequency until the ions hit a detector plate.⁵⁵ Later, ICR-MS relied on measuring the power absorption from an exciting rf frequency and plotted as power absorption vs. magnetic field strength.⁵⁶ This required scanning the magnetic field, in analogy to a magnetic sector mass spectrometer. Two further advancements in the early 1970's allowed the development of FT-ICR, as the technique that we know today. McIver and co-workers showed that electrostatic trapping voltages could trap the ions in the direction of the magnetic field, so that ions of different m/z could be trapped simultaneously. With the advancement of computers and the fast Fourier transform algorithm,⁵⁷ applications in nuclear magnetic resonance (NMR) showed that multiple frequency components could be resolved. The same idea was implemented by Comisarow and Marshall^{58,59} to develop FT-ICR. Since these breakthroughs, FT-ICR MS has improved steadily—the application of superconducting magnets has allowed FT-ICR MS to reach mass resolutions and mass accuracies not possible with other MS instrumentation.⁶⁰

Fourier Transform Ion Cyclotron Resonance Theory

Cyclotron motion

In the presence of a magnetic field B , an ion is subject to the Lorentz force, which is expressed as the scalar product:

$$\text{Force} = \text{mass} \times \text{acceleration} = m \frac{dv}{dt} = q\vec{v} \times \vec{B}, \quad (2-2)$$

where m is mass, q is charge, and v is the velocity of the ion. The Lorentz force is perpendicular to the plane determined by v and B . For the special case that v and B are perpendicular, the magnitude of this force becomes $F = qvB$. The resulting motion is circular and is denoted as the ion cyclotron motion, illustrated in Figure 2-1. If the plane perpendicular to the magnetic field is defined as x and y , then the velocity of the ion in that plane can be defined as

$$v_{xy} = \sqrt{v_x^2 + v_y^2} \quad (2-3)$$

and angular acceleration is

$$\frac{dv}{dt} = \frac{v_{xy}^2}{r} \quad (2-4)$$

equation 2-2 becomes

$$\frac{mv_{xy}^2}{r} = qv_{xy}B_0 . \quad (2-5)$$

Since angular velocity, ω (rad s⁻¹), around the z -axis (parallel to the magnetic field), is defined by

$$\omega = \frac{v_{xy}}{r} , \quad (2-6)$$

equation 2-5 becomes

$$m\omega^2 r = qB_0\omega r . \quad (2-7)$$

This simplifies to equation 2-1, the cyclotron equation.

$$\omega_c = \frac{qB}{m} \quad (2-1)$$

The key feature of this equation is that the frequency is independent of the velocity the ion and thus is independent of the radius of the ion. Thus, given a magnetic field, in our case 4.7 T, a singly charged ion, such as protonated tryptophan, has a *m/z* of 205 and a frequency of 351 kHz:

$$\frac{4.7T}{2\pi \times (205u \times 1.661 \times 10^{-27} kg u^{-1} / 1.602 \times 10^{-19} C)} = 351 kHz$$

The radius is, however, dependent on the ion velocity and can be solved by rearrangement of equation 2-5.

$$r = \frac{mv_{xy}}{qB_0} \quad (2-8)$$

This equation is known as the ion cyclotron orbital radius, and the ions can be excited to exact radii based on the *m/z* and the velocity of the ions. This is key to many concepts of FT-ICR, since it is by this relationship that ions can be excited out of the trap for mass isolation, excited to larger kinetic energies for collisions with background gas to induce collision induced dissociation (CID), and excited to larger radii for detection on the plates of the ICR cell. An example of these conditions in an ICR cell can be seen in Figure 2-2.

To excite an ion in an ICR cell, a uniform sinusoidal electric field can be applied perpendicular to the magnetic field. This field can be defined by the voltage difference across the two plates at a fixed distance *d*.

$$E_0 = \frac{V_{p-p}}{d} \quad (2-9)$$

An ion will absorb power, $A(t)$, based on the following dot product

$$A(t) = \text{Force} \cdot \text{velocity} = qE(t) \cdot v_{xy} . \quad (2-10)$$

It can be shown that the post-excitation radius is given by^{61,62}

$$r = \frac{V_{p-p} t_{\text{excite}}}{2dB_0} . \quad (2-11)$$

Crucially, the ion radius after excitation is independent of the ion's m/z . Rather, all ions can be excited to the same cyclotron radius, provided that the magnitude of the sinusoidal wave does not change as a function of rf frequency.⁶⁰

In addition to exciting the ions to a useful cyclotron radius, the excitation waveform also creates a coherent ion packet (for ions of a particular m/z). Prior to excitation, the phase of the cyclotron motion is random. The orbiting of a coherent ion packet at a sufficiently large radius allows detection in the form of an image current on the detection plates. As a result of collisions and space charge effects, the ion packet will de-phase with time, giving rise to the well-known damped ion signal or transient.

Mass detection

Mass detection in an ICR cell is performed with two plates at some distance, d , from each other, with ions at an excited radius circulating in the ICR cell. As an ion moves past each of the plates, the ion can induce a charge on the plate, at a rate dependent on the frequency of its cyclotron motion. If enough data points are taken, the frequency of motion can be determined, and that frequency is directly related to the m/z based on equation 2-1. The image current detected on the plates is defined as the difference in charge detected on the two plates ΔQ

$$\Delta Q = -\frac{2qy}{d} , \quad (2-12)$$

thus, the ICR signal is independent of the magnetic field and increases linearly with the velocity component, y , and increases as the ion cyclotron radius is increased.

Furthermore, the current detected is proportional to the charge of the ion, which means multiply charged ions, such as the ions generated by electrospray ionization, also increase the sensitivity of the detection.

Trapping motion

Thus far, the motion of the ions in the ICR cell has been described by the cyclotron motion in the x-y plane of the trap governed by the uniform magnetic field perpendicular to the z-direction plane. However, the ions also undergo a z-direction oscillation based on the trapping potentials applied at the end caps of the ICR cell. The z-dimension potential is delivered by the voltages at the end caps and is defined as the quadratic potential in the z-direction, $\Phi_z \sim z^2 / 2$. However, the ions do have x and y motion, therefore a three-dimensional trapping potential must be considered. The resulting oscillating frequency, ω_z , is derived elsewhere⁶³ and is described in equation 2-13,⁶³

$$\omega_z = \sqrt{\frac{2qV_{trap}\alpha}{ma^2}}, \quad (2-13)$$

where m is the mass of the ions q is the charge, a is the trap size, α is a constant that depends on the trap design, and the voltage applied is V_{trap} .

Magnetron motion

Combination of the motion in the x-y plane dictated by the cyclotron motion and the motion of the ions in the z-plane dictated by the end caps in the ICR cell generates a third type of motion called magnetron motion. Equation 2-14 is the frequency that correlates to the reduced cyclotron frequency of the ion that is observed in the presence of the trapping voltage of the ICR cell. Equation 2-15 is the frequency that correlates to

the magnetron frequency and is the circular motion of the ions that is superimposed onto the cyclotron motion.

$$\omega_+ = \frac{\omega_c}{2} + \sqrt{\left(\frac{\omega_c}{2}\right)^2 - \frac{\omega_z^2}{2}} \quad (2-14)$$

$$\omega_- = \frac{\omega_c}{2} - \sqrt{\left(\frac{\omega_c}{2}\right)^2 - \frac{\omega_z^2}{2}} \quad (2-15)$$

The cyclotron motion is far greater than the magnetron and trapping motion and is thus the only motion that is useful for detection.^{60,64} However, the cyclotron motion is reduced by the magnetron motion and the mass spectrometer must be calibrated to account for this effect. The trapping motion is parallel to the detection plates, thus it is not registered. The three frequencies described above are illustrated in Figure 2-3.

Space charge effects

In addition to the ion's cyclotron, magnetron, and trapping motions in the ICR cell, the ion motion is also affected by space charge. In short, the phenomenon can be understood as charged species coming within proximity of one another; their interactions can have an effect on the motion inside the trap. This interaction can result in a shift of the cyclotron motion, thus resulting in an incorrect recorded mass spectrum.⁶⁵ The theory of space charge was developed by Jeffries and co-workers by considering frequency shifts with ions of known masses and necessitated a mass calibration to account for the space charge effects.⁶⁶ Equation 2-16 is the angular frequency, ω_+ , of a single ion's natural mode in a cubic cell

$$\omega_{\pm} = \frac{\omega_c}{2} \left\{ 1 \pm \left[1 - 4 \frac{\left(\frac{2qV_T G_T}{m} + \frac{\rho q^2 G_T}{\epsilon_0 m} \right)}{\omega_c^2} \right]^{1/2} \right\}, \quad (2-16)$$

where ω is the angular frequency, ω_c is the cyclotron frequency, q is the ions charge, m is the ion mass, V_T is the trapping voltage, G_T and G_i are geometry factor of the ICR cell, and ρ is the charge density. By comparison with the cyclotron frequency, an effective frequency can be calculated by equation 2-17.

$$\omega_{eff} = \omega_c - \frac{2\alpha V_T}{a^2 B} - \frac{\rho q G_i}{\epsilon_0 B}, \quad (2-17)$$

Thus, the frequency difference between two ions of different mass can be calculated in equation 2-18.

$$\omega'_{eff} - \omega''_{eff} = qB \left(\frac{1}{m'} - \frac{1}{m''} \right) \quad (2-18)$$

Given a known magnetic field, B , measuring the values of ω'_{eff} and ω''_{eff} the mass of an unknown ion can be determined based on comparison to a reference ion.

Fourier Transform Ion Cyclotron Resonance Instrumentation

In order to use FT-ICR MS for gas-phase studies, ions need to be generated and guided to the ICR cell for analysis. In order to couple high-pressure ion sources, such as electrospray ionization (ESI) (discussed in Chapter 1), with a high-vacuum ICR cell, an FT-ICR mass spectrometer must contain ion guiding optics with a differentially pumped vacuum system. A diagram of the instrument used for work reported in this thesis is given in Figure 2-4, showing the ion source, transfer optics, a superconducting magnet and an analyzer cell for mass analysis. Moreover, a data collection system is required to convert the analog signals into a digitally encoded mass spectrum.

Ion optics and vacuum system

In the ESI source, the ions travel through a heated glass capillary and a skimmer, and are then accumulated in a hexapole for a certain time, e.g., 0.5-3 s. Upon pulsed extraction from the hexapole, the ion packet is guided to the Penning trap of the FT-ICR via electrostatic lenses. In this process, the ions are accelerated to ~3 kV, and hence ion transfer times on the order of 700-1500 μ s are expected. While some of the electrostatic lenses act as deflection plates to adjust the direction of the beam, the focusing Einzel lens is particularly important to overcome the fringing magnetic field. In the fringing magnetic field, there is a substantial radial magnetic field component, which applies a force contrary to ion motion, the so-called magnetic “bottle” effect. This radial field component is zero on-axis, and hence ion transmission is optimized for focused ions.

Ions are generated at ambient pressures with electrospray ionization, but are transferred to the Penning trap, held at an ultra-high vacuum (i.e., 10^{-9} to 10^{-10} Torr). These low pressures are required to avoid collisions, in order to minimize de-phasing of the excited ion packet. The effect of pressure on the number of collisions can be determined by the mean free path, λ , of the ion

$$\lambda = \frac{k_B T}{\sqrt{2\pi} d^2 p} , \quad (2-19)$$

where k_B is the Boltzmann constant, T is the temperature, d is the diameter of the ion, and p is the pressure of the system. Given an ion's approximate diameter of 1 nm, a pressure of 10^{-10} Torr, and T of 298 K, the mean free path is calculated to be $\sim 6.8 \times 10^1$ km, i.e., an ion will travel this distance before it has a collision.

Magnet

In FT-ICR MS either electromagnets or superconducting magnets are employed to achieve high magnetic fields. Electromagnets offer magnetic field strengths of up to 3.0 T. To achieve ultimate resolution and resolving power, higher magnetic field strengths are essential, which requires the use of superconducting magnets. The superconducting magnet used in these experiments was a 4.7 T actively shielded magnet. Meanwhile, magnets up to 14.5 T have been used in combination with FT-ICR at the High Magnetic Field National Lab (NHMFL) (Tallahassee, FL) to achieve mass resolutions of 200,000 at $m/\Delta m_{50\%}$ for an ion of 400 m/z and a transient time of merely 1 s.⁶⁷ Figure 2-5 illustrates the increase in FT-ICR performance with increasing magnetic field strength. Some characteristics scale linearly, such as scan speed, whereas others scale as with to a square of the field strength, such as upper mass limit and trapping times. Larger magnets result in significant performance gains; however, caveats remain for these types of magnets. Initial cost is expensive and liquid nitrogen and helium replenishment is required to keep the magnet at liquid helium temperatures. Furthermore, the overall size of the magnet is large and thus significant lab space for the instrument is required.

Analyzer cell

The Penning trap or analyzer cell is located within the homogenous portion of the high magnetic field. The analyzer cell can be considered the most important part of the FT-ICR instrument, as the ions are trapped, mass isolated, dissociated, and detected here. The analyzer cell contains three basic components: DC trapping plates, excitation plates, and detection plates, which are depicted in Figure 2-6 for a closed cylindrical cell design. While the magnetic field constrains ion (cyclotron) motion in a plane perpendicular to its direction, an electrostatic field is required to trap the ions in the

direction of the magnetic field. The Penning trap is thus an electromagnetic trap. An rf voltage is applied to the excitation plates to excite ions in the trap. This rf voltage can be used to: (1) excite ions out of the trap for mass isolation, (2) excite ions to larger radii to increase their kinetic energy for collision induced dissociation, or (3) excite the ions to a large enough radius that the ion packet produces an image current on the detection plates. The frequency at which the ions move past the detection plates is constant, and thus performing a Fourier transform on the current induced on the detection plates is the physical detection that leads to a frequency spectrum, which can be mathematically converted to a mass spectrum with equation 2-1.

Data system

The data system is necessary to convert the physical information of the induced current on the detection plates to a mass spectrum that is viewable in the software package. The data system provides a broadband rf generator for the excitation plates, the voltages to the trapping plates and the ion optics for guiding the ions into the mass spectrometer. The data system also includes a pulse generator for experiment timing, a fast transient digitizer for data conversion, and a computer system for process and software control.⁶⁴ The software provides an interface between the data system and the operator such that voltages and experimental conditions can easily be modified by changing numerical values or adding events. This is crucial for MS experiments, as voltages need to be adjusted readily for isolating different ions of interest—changing experimental parameters are as simple as turning events on and off.

Instrumentation Operation

A major advantage of the FT-ICR mass spectrometer is that other than ionization, all other mass spectrometric techniques occur in the Penning trap. Although other

experimental events can be added to the entire experimental sequence, an FT-ICR experiment requires some basic components. The events that need to occur are a quench of the cell, ionization and optimized ion optics to bring the ions to the ICR cell, an excitation event, followed by detection of the ion packet. An illustration of the workflow can be seen in Figure 2-7.

The first step of the experimental workflow is quenching. Quenching is required to empty the Penning trap prior to injecting new ions into the trap for detection. This is done by adjusting the trapping potentials on the trapping plates such that all ions are destabilized along the z-axis. This process has a duration on the order of milliseconds, which is sufficient to evacuate the cell of any ions that are left from previous experiments.

The second step of the experimental workflow involves ionization and guiding the ions into the Penning trap. The ionization fundamentals have been covered in Chapter 1 and the methods for driving the ions into the cell have been covered earlier in this chapter. However, the timing of the extraction pulse from the hexapole and the timing of applying the Penning trap potentials are crucial for efficient trapping of ions. Another advantage of this setup is the ability to accumulate ions in the hexapole multiple times during one experiment. This is effective for increasing the number of ions trapped. The disadvantage of this technique is that ions already stored in the Penning trap can escape while the front trapping potential is lowered to bring new ions in. For ions that are difficult to generate, this is extremely useful for increasing their abundance, thus increasing the sensitivity of the MS experiments.

Once inside the trap, ions are subject to the cyclotron motion as described earlier. The cyclotron motion is controlled by the magnetic field in the x-y plane, and the trapping motion is dictated by the trapping voltages on the end plates. Trapping voltages are typically around 0.5 V – 5 V, for positive ions (-0.5 V to -5 V for negative ions). For the FT-ICR instrument in these experiments, a trapping voltage of 1.40 V was used for PV2, the back trapping plate, and PV1, the front trapping plate. The actual experimental values are given for trapping positive ions.

While ions are stored in the Penning trap, a number of optional steps can be employed. For example, to perform mass isolation, ions can be removed by exciting them to larger radii than the dimensions of the trap. This is typically completed by applying a correlated sweep excitation pulse.⁶¹ A broadband excitation of rf frequencies is carried out, while isolating a user specified window of frequencies. Thus, all ions, except for the ion of interest can be excited to radii larger than the trap (i.e., removed), while the ion of interest is left in the trap for either detection or further MS analyses.^{60,64} In fact, the user specifies a *m/z* window for mass isolation, which is then automatically converted into the frequency domain by the software. Furthermore, dissociation experiments can be performed while ions are stored in the Penning trap. For IRMPD experiments, the software sends a transistor–transistor logic (TTL, +5 V) pulse to an electromechanical shutter, which opens for the duration of laser irradiation. This allows for user-defined irradiation times in the experiment.

The third step of a basic FT-ICR experiment involves excitation of the ions in the Penning trap. This is required to bring the ions that are radially close to the center of the trap to a larger, detectable radius. To bring the ions to a larger radius, an rf sweep is

applied to the excitation plates of the Penning trap. This is done by sweeping through the cyclotron frequencies of all of the possible ions that could be in the trap. This method of applying multiple frequencies in a single, short, high intensity signal is known as a ‘chirp’.⁶⁰ When the applied frequency matches the cyclotron motion frequency, the ion absorbs energy and is accelerated into a larger orbit in the trap. Optimization of the chirp is important because the sensitivity of the experiment is directly related to ion packet distance from the plates. However, if the ions are brought too close to the detection plates, it is possible to lose ions due to collisions with the trap boundaries. Thus optimizing the amplitude of the applied rf field is crucial to efficient MS experiments.

The fourth step of the experimental workflow is the ion detection. The detection step immediately follows the broadband excitation of all frequencies to excite the ions of interests to a detectable radius for mass analysis. As mentioned earlier in the chapter, the radius of the ions does not affect the cyclotron motion. Thus, current is induced on the detection plates at a frequency based on the cyclotron motion of different m/z ion packets that are present in the mass spectrometer. Furthermore, the number of ions in each packet is directly proportional to the intensity of the signal at that given frequency. The induced current is recorded for a set amount of time and the packet of ions will pass the detection plates multiple times for detection. This spectrum is called the time domain spectrum, and by conducting a Fourier transform on the time domain, the frequencies of ion oscillation can be mathematically extracted to form the frequency spectrum. Given a known uniform magnetic field, the frequency spectrum can be easily converted into a mass spectrum.

An advantage of FT-ICR MS is that ions are not destroyed during detection. Other mass spectrometers, excluding orbitraps, destroy ions during the detection process. Thus, FT-ICR MS offers the advantage of being able to detect ions, perform other mass analyses, and redetect the same set of ions afterwards (although this procedure is not performed here). Furthermore, sensitivity is increased by increasing the acquisition time, rather than needing more total ions, which is needed in other mass spectrometers.

The entire sequence of the experiment can also be repeated in the software for a user determined number of times. The scans maintain the exact experimental conditions and allow for the signal-to-noise to increase, improving the resolution of the mass spectrum.

Quadrupole Mass Filter, Quadrupole Ion Trap, Time-of-Flight Mass Spectrometer

This section will cover the basic principles of operating the custom-built quadrupole mass filter, quadrupole ion trap, time-of-flight (QMF-QIT-ToF) mass spectrometer, specifically toward performing infrared multiple photon dissociation (IRMPD) tandem MS on this instrument. Details of this section include theory on quadrupole mass filter, quadrupole ion trap, and time-of-flight. The general operation of the QMF-QIT-ToF instrument is also presented.

Quadrupole Mass Filter Theory

Since its inception in the early 1950's by Paul and Steinwedel,⁶⁸ the quadrupole mass filter (QMF) remains among the most popular mass analyzers in mass spectrometry, due to its compactness and low price. A QMF consists of four rods in a square geometry extending in the z-direction, as illustrated in Figure 2-8. Direct and alternating currents (DC and AC), are applied to the rods, which give rise to time-dependent fields that are mass-selective. Ions enter the quadrupole mass filter along

the z-axis and are exposed to attractive and repulsive forces in the x-y plane. At any moment in time, the same potential is applied to the x-axis rods, whereas an opposite potential is applied to the y-axis electrodes. If the potentials applied are defined as DC voltage, U , and rf voltage, V , at a frequency ω , then the total potential applied Φ_0 is given in equation 2-20.

$$\Phi_0 = U + V \cos(\omega t) \quad (2-20)$$

Thus, the equations of motion can be expressed in terms of x and y directions as equations 2-21 and 2-22.

$$\frac{d^2x}{dt^2} + \frac{e}{m_i r_0^2} (U + V \cos \omega t)x = 0 \quad (2-21)$$

$$\frac{d^2y}{dt^2} - \frac{e}{m_i r_0^2} (U + V \cos \omega t)y = 0 \quad (2-22)$$

The periodic field is inhomogeneous due to the opposite polarity applied in the x and y directions, so there is a region in the trap where the field is effectively zero in the x and y planes. This is depicted in Figure 2-8 as the dotted lines between the four rods. Thus, ions can pass through the QMF, provided that their amplitudes in the x -y plane is smaller than the geometry of the trap. The required conditions to drive a packet of ions through a QMF can be derived from the Mathieu equation shown in equation 2-23.⁶⁹

$$\frac{d^2f}{d\tau^2} = -[a - 2q \cos 2\tau]f \quad (2-23)$$

Thus comparing the Mathieu equation, with the equations of motion 2-21 and 2-22 in the x and y directions, the parameters a and q can now be solved in equations 2-24 and 2-25.

$$a_x = -a_y = \frac{4eU}{m_i r_0^2 \omega^2} \quad (2-24)$$

$$q_x = -q_y = \frac{4eV}{m_i r_0^2 \omega^2} \quad (2-25)$$

By appropriately choosing the DC voltage U , rf amplitude V , and rf frequency ω , a narrow m/z range has stable trajectories in x-y, while traveling through the QMF, whereas all other m/z are filtered out. The region in parameter space that allows transmission of a particular m/z range, known as the stability diagram, is generally expressed using the dimensionless parameters a and q as shown in Figure 2-9.⁷⁰

If the ratio of a/q is defined as $2U/V$ and is set to $0.237/0.706 = 0.336$, the x-y stability region is reduced to one point on the stability diagram in Figure 2-9, namely the apex. Thus, by lowering a at a constant q , or by reducing the DC potential with constant AC, the isolation width of the stability diagram can be increased for a given m/z . Note that if the QMF is operated in rf-only mode, a wide range of m/z will be transmitted, as the stability diagrams of many ions overlap with this position on the a vs. q plot.

The QMF used for the studies done in Chapter 5 is composed of four spherical rods of 9 mm in diameter and 8 inches in length. The power supply feeding the QMF is capable of a maximum rf amplitude of 5,000 Vpp, the r_0 is 8.5 mm and given an rf frequency of 1MHz and a maximum q value of 0.908, the lower mass limit of the filter is 0.37 m/z .

$$\frac{2 \times 1.6022 \times 10^{-19} C \times 5000V}{0.908 \times 1.661 \times 10^{-27} kg u^{-1} \times (8.5 \times 10^{-3})^2 \times (2\pi \times 10^6)^2} = 0.37 m/z$$

As q approaches 0 the upper mass limit reaches infinity. Thus, theoretically a large mass range can be transferred through the QMF; however, actually mass ranges that can be transferred mass selectively are typically 20 m/z to 4000 m/z .⁷¹ For mass selection, the QMF will be operated at the apex, to filter out all ions other than the ions

of interest. It is in this part of the instrument where the mass selection is accomplished. This is one of the major differences between the custom built instrument and the FT-ICR mass spectrometer discussed earlier. All mass selection, storage and detection are done in the Penning trap in the FT-ICR mass spectrometer, whereas the QMF-QIT-ToF has different regions responsible for each stage of the experiment.

Quadrupole Ion Trap

Similarly to the QMF, the quadrupole ion trap (QIT) was also invented by Paul and Steinwedel in the early 1950's,⁷² however, it was not until the 1980's that QITs began to gain wider recognition in mass spectrometry.⁷³⁻⁷⁵ The QIT, illustrated in Figure 2-10, is made of two hyperbolic electrodes, which act as the endcaps, for control in the z-direction, and a ring electrode, which contains the ions in the x-y plane; however, due to symmetry considerations, in the case of QITs the x-y plane is typically discussed as the r plane.⁷⁶

In the QIT the rf potential is exclusively applied to the ring electrode, while a DC potential is applied to the endcaps.⁷³ The electric field in the QIT can be described in cylindrical coordinates and is expressed in equation 2-26.^{73,77}

$$\Phi_{x,y,z} = \frac{\Phi_0}{r_0^2} (r^2 - 2z^2) \quad (2-26)$$

Therefore, the motion of ions can be described in the z plane and the r plane.

$$\frac{d^2z}{dt^2} - \frac{4e}{m_i r_0^2} (U - V \cos \omega t) z = 0 \quad (2-27)$$

$$\frac{d^2r}{dt^2} - \frac{4e}{m_i r_0^2} (U - V \cos \omega t) r = 0 \quad (2-28)$$

Solving the differential equations via the Mathieu equation (equation 2-23), the ion motion can be expressed in terms of a and q in equations 2-29 and 2-30.

$$a_z = -2a_r = -\frac{16eU}{m_i r_0^2 \omega^2} \quad (2-29)$$

$$q_z = -2q_r = -\frac{8eU}{m_i r_0^2 \omega^2} \quad (2-30)$$

The DC voltage applied is expressed in U , and the rf frequency applied is via ω , where $\omega = 2\pi f$, and f is the rf frequency. The stability diagram for a QIT is shown in Figure 2-11. Note that U refers to the DC voltage difference between the ring electrode on one hand, and the endcaps on the other. A QIT is typically operated at $a_z = 0$, which means that $U=0$. An ion is trapped in the QIT, provided that it's q_z value < 0.908 . Since q_z scales inversely with m/z , there will be a low-mass cut-off which cannot be trapped in the QIT. The typical operation of a QIT involves trapping all ions, and then scanning these ions out of the trap (in the z-direction) in the rf-only instability mode. This entails increasing the rf amplitude V to progressively eject larger m/z ions.

The trapping of ions in a QIT can be compared to a marble kept in the center of a saddle point by rotating the saddle at some frequency, as shown in Figure 2-12. If the saddle is rotated too slowly, the marble will fall off by rolling down one of downhill slopes; however, at faster rotation speeds, the marble is trapped in the center – by the time that the marble starts rolling down a downhill slope, this is replaced by an uphill slope. The actual motion of an ion in a QIT is much more complex, involving Lissajous-type trajectories. Typically, a light buffer gas such as He, is used in the QIT to dampen the motion of ions. This is used to keep ions closer to the center of the trap, which enhances the sensitivity and resolution of the QIT.

The QIT used in these experiments reported here was simply used as a trap and not a mass analyzer. This was the region where ions were subjected to IRMPD

experiments. There are some advantages and disadvantages of tandem MS in the QIT compared to the Penning trap of the FT-ICR mass spectrometer—the main disadvantage is the operating pressure of the traps. The Penning trap is typically four to five orders of magnitude lower in pressure than a typical QIT. This is because the QIT relies on collisions to relax ions to the center of the trap for stability, which is not necessary in the Penning trap. Collisions result in ion ‘cooling’ (or relaxation), thus for IRMPD experiments, it may be more difficult to dissociate. This is because as photons are absorbed by the ion in resonance with a vibrational mode, the absorbed energy can be dissipated by collisions. The collisional cooling makes reaching dissociation thresholds difficult causing ions to remain intact, rather than dissociating due to the IRMPD mechanism described in Chapter 1.

One way to overcome this limitation is to add a light buffer gas in a pulsed fashion, rather than operating the trap at a constant high pressure. Helium gas can be introduced with a TTL pulse, timed with the ion packet entering the QIT. Thus, trapping efficiencies are increased initially, and a time delay allows the lighter He gas to be pumped away, lowering the pressure conditions in the trap. This is the method that was employed in the QIT to perform IRMPD experiments and it is explained in detail in Chapter 5.

The major advantage of the QIT compared to the Penning trap is improved ion cloud overlap with the laser beam. In the QIT, the ion packet is restrained to a much smaller volume compared to the Penning trap. Thus, a complete overlap of the laser beam and the ion cloud is possible. Furthermore, laser focusing lenses are employed in the QIT apparatus with known focal distance to achieve optimal overlap. Experiments

were performed in the Penning trap to manipulate the ion packet along the z-axis by adjusting the trapping potentials. This procedure will be discussed further in Chapter 5; however, it was shown that IRMPD yield could be significantly enhanced by squeezing the packet in the z-direction, as well as holding the packet closer to the back trapping for the irradiation experiment. Chapter 5 will discuss the details of IRMPD in both the Penning trap and QIT further and cover whether an increase in the laser overlap with the ion cloud can overcome the limitations introduced by performing IRMPD at higher pressures.

Time-of-Flight Mass Spectrometry

The first ToF instrument was introduced by Stephens⁷⁸ and eventually was commercialized for coupling with gas chromatography.^{79,80} The underlying principle of ToF-MS is that ions of different *m/z* will disperse in time during their flight in a field free region of a given length.

By applying an electric field between two plates, ions are biased to a high potential energy, E_{el} , which is then converted into kinetic energy, E_{kin} , and hence translational motion, according to the relationship:

$$E_{el} = ezU = \frac{1}{2}m_i v^2 = E_{kin}, \quad (2-31)$$

where e is the elemental charge, z is the charge state of the ion, U is the electric potential, m is the mass of the ion, and v is the velocity of the ion. Assuming the ions start without any prior kinetic energy, then the velocity, v , of the ions can be derived as

$$v = \sqrt{\frac{2ezU}{m_i}}, \quad (2-32)$$

and the drift time, t , that an ion of a given *m/z* requires to travel a distance, s is given by

$$t = \frac{s}{v}; t = \frac{s}{\sqrt{\frac{2eU}{m_i}}} \quad (2-33)$$

Rearrangement of equation 2-33 allows for a clearer relationship that the time it takes to transverse the drift tube is proportional to the square root of the m/z .

$$t = \frac{s}{\sqrt{2eU}} \sqrt{\frac{m_i}{z}} \quad (2-34)$$

The ions are injected into the ToF drift tube and are detected by measuring the time it takes for them to reach the microchannel plate at the end of the drift tube. The major advantages of ToF mass spectrometer are the high throughput capabilities, the sensitivity of detection and the very high speed, as a mass spectrum can be obtained in 100's of μ s. Physical detection of ions on a plate is a much more sensitive process than detecting an induced current in the FT-ICR approach. Although ToF offers relatively high resolving power ($>10,000$), the FT-ICR resolving power can be increased by lengthening the detection time. Finally, the relative cost of ToF is much less than that of the magnet and cryogenics required for operating an FT-ICR mass spectrometer.

Optical Parametric Oscillator Lasers

Using optical parametric oscillator (OPO) lasers for photodissociation experiments is becoming increasingly popular. While OPO lasers have lower continuous power than the two other lasers typically used for photodissociation, free electron lasers and CO₂ lasers, they offer significant advantages. The OPO is a wavelength tunable, tabletop laser that can be installed in any lab. Free electron lasers (FELs), while being continuously tunable over wide wavelength ranges, are only available at user facilities. CO₂ lasers are tabletop lasers; however, tunable CO₂ lasers are limited to narrow tuning ranges (9.2 – 10.8 μ m).

The general premise of an OPO laser rests on a non-linear process where a photon at one wavelength, the pump photon, can be split into two product photons at different wavelengths, the ‘signal’ and ‘idler’. The law of conservation of energy requires that the energy of the two photons must equal the energy of the photon they were generated from. The OPO laser wavelengths are tuned by either changing the pump photon, or changing the interaction with the material, which results in a change in wavelength. The history, theory and general operation will be discussed further in this chapter.

History

The development of OPO lasers began in 1961 when Franken et al. discovered that passing photons from a high-powered pump laser through a material with nonlinear optical properties generates second harmonic light.⁸¹ This discovery led to the development of photon tunability by optical parametric amplification and oscillation⁸²⁻⁸⁷ and the first tunable OPO laser was introduced in 1965 by Giordmaine and Miller.⁸⁸ Since that introduction in 1965, advances in pump sources, nonlinear materials, and cavity designs have increased tunability and fluence.⁸⁹⁻⁹⁷ The OPO used in experiments discussed here is a continuous wave LINOS OS4000 OPO laser tethered to a Fourier transform ion cyclotron resonance (FT-ICR) mass spectrometer. The wavelength range produced by the LINOS OPO is 1.38–2.0 μm for the signal beam and 2.28–4.67 μm for the idler beam, pumped by a 2 W Nd-YAG (neodymium-doped yttrium aluminium garnet), 1064 nm laser. This results in 25–75 mW of continuous power per beam, with narrowband radiation (< 1 cm⁻¹).⁹⁸

Optical Parametric Oscillator Theory

The idea of splitting a pump photon into two new photons, signal and idler, can be visualized in Figure 2-13. When a pump beam, ω_p , is placed in a cavity with a nonlinear optical material, such as a periodically polled lithium niobate (LiNbO_3) crystal, two new beams are generated, the signal, ω_s , and idler ω_i . The relationship between the three beams is shown in equation 2-35.

$$\omega_p = \omega_s + \omega_i \quad (2-35)$$

In the crystal, the pump beam is depleted as the signal and idler beams are generated, thus amplifying the overall fluency of the two generated beams. Furthermore, the beams resonate in the cavity until they reach a certain power threshold (~200 mW). The laser beams can then exit the cavity to be used for experiments.⁹⁹ The generation of light and amplification can be explained by nonlinear optics and quasi-phase matching, discussed below.

Nonlinear optics

When light interacts with a medium, the result can be described by conventional, linear optics. However, when the light interaction deviates from conventional optics, it is then referred to as nonlinear optics. To describe nonlinear optics, it is easier to first think of a few equations based on linear optics. The first is based on the electric polarization induced in a medium.

$$P = \epsilon_0 \chi E \quad (2-36)$$

Equation 2-36 displays a simple linear relationship of the electric polarization vector to the electric field, E , where ϵ_0 is the free-space permittivity, and χ is the susceptibility of the given medium. Thus, based on this relationship, there is no coupling between beams of monochromatic light through a medium.

The second is the intensity of light propagating in an absorptive medium can be described as a function of the initial intensity

$$I(l) = I(0) \cdot e^{-\alpha x} , \quad (2-37)$$

where I is the beam intensity, x is the variable along the propagation direction, and α is a constant for the medium the beam is traveling through.

The third is related to transmission of light through a medium and is based on a Fabry-Perot interferometer. Consider two equations

$$T = \frac{1}{1+F \sin^2(\delta/2)} \quad (2-38)$$

$$\delta = \frac{4\pi}{\lambda} n_0 d \cos \theta , \quad (2-39)$$

where T is transmission, F is the reflectivity of the two mirrors of the interferometer, δ is the phase-shift factor, which is calculated by λ , the wavelength of the light, d the spacing between the two mirrors, θ , the angle between the beam and mirrors, and n_0 , the refractive index of the medium. The transmission intensity I_t , is linearly proportional to the initial intensity, I_0 , since T is a constant based on the characteristics of the medium.

$$I_t = T \cdot I_0 \propto I_0 \quad (2-40)$$

It is by the relationships shown in equations 2-36, 2-37, and 2-40 that linear optics is defined. However, after the development of the first laser source in the Hughes Research Laboratory in 1960,¹⁰⁰ it was soon discovered that the simple linear relationships could not describe all situations in which intense laser light was interacting with certain types of optical media.

The OPO laser described here rests on a second-order susceptibility effect, in analogy to second-harmonic generation, sum-frequency generation, difference-

frequency generation, and third harmonic generation.¹⁰¹ Although linear optics could not explain these phenomena, it was realized that the nonlinear effects could be explained by the electric polarization induced in a medium (equation 2-41) expressed as a power series.

$$P = \varepsilon_\alpha [\chi^{(1)}E + \chi^{(2)}EE + \chi^{(3)}EEE + \dots] \quad (2-41)$$

Considering the first order susceptibility, just as equation 2.36 shows, this is the linear behavior of light. The second order susceptibility represents the start of the nonlinear behavior. It is from the second order susceptibility that the optical parametric oscillation occurs, i.e., the pump photon is converted into signal and idler photons by interacting with a medium.

The nonlinear conditions account for the electromagnetic field of the light and the interaction with the electron cloud of atoms or molecules in the medium. In the case of the LiNbO₃ crystal in the OPO laser, a field stimulated change in the electron cloud excites the LiNbO₃ molecule to a virtual state via the destruction of a pump photon. When the molecule relaxes, this generates two photons, the signal and idler photons.^{102,103} Furthermore, amplitude of the generated photons can be increased by meeting the phase matching conditions, $\Delta k = 0$. The phase matching conditions have been derived elsewhere,^{102,103} however, the interaction between the pump, signal and idler can be expressed as a function in the change in wave vector relative to the refractive index and wavelength of each photon.

$$\Delta k = k_p - k_s - k_i = \left(\frac{n_p}{\lambda_p} - \frac{n_s}{\lambda_s} - \frac{n_i}{\lambda_i} \right), \quad (2-42)$$

where k is the amplitude scalar to the wave vector, n is the nonlinear refractive index, and λ is the wavelength of light. As long as phase conditions are met, and $\Delta k = 0$, then

energy can be transferred from the pump beam to the signal and idler beams. This interaction describes the parametric amplification within the crystal and allows for significant gain in fluence of the signal and idler beams. Furthermore, other wavelengths of light result from the non-linear optical conditions and can be seen in the OPO laser cavity. For example a visible green light, 532 nm, is a result from the non-phase-matched second harmonic generation of the pump beam frequency inside the PPLN crystal at pump resonance. In addition to the green light, other visible red light (600 nm - 700 nm) is seen and results from the coupling of the pump and signal beams.

Periodic poling

Periodic poling of the crystal refers to altering the crystal structure during growth of the crystal so that there are spaces between points of phase divergence, to effectively bring the fields back into phase, also known as quasi-phase matching.^{102,104} Since there is a phase lag as light travels through the medium, changing the spacing of the medium keeps the light in phase. If the light stays in phase, parametric amplification can occur throughout the medium, thus significantly increasing the gain of the second harmonic light. The maximum overlap of parametric amplification is known as the phase coherence length, and is determined at the point the signal and idler beams are 180° out of phase. The crystal can then be grown^{105,106} to keep the light in coherence and thereby allow significant increase in overall depletion of the pump into the signal and idler, but also keep the signal and idler in phase as they enter the resonance cavity.

Resonance cavity

The OPO laser can be thought of as containing two separate cavities, one for maintaining pump resonance and the other for amplifying the signal and idler beams. An illustration of the OPO laser cavity is shown in Figure 2-14. The different parts are

labeled 1 through 18. To keep the pump beam in resonance the Pound, Drever, and Hall (PDH) technique is employed in the OPO.^{107,108} This is done by modulating the Nd:YAG pump beam to produce two 12 MHz side bands on each side of the principal beam. With the cavity properly aligned, the side bands resonate in the cavity, just as the principal beam. The resonance travels back toward the pump beam source and is separated by a Faraday isolator (4) – which allows light transmission in one direction only. The reflected beam is then focused onto a photodiode (5) for comparison and an error signal is generated. If the error signal is zero, the cavity is in resonance and signal and idler beams can be generated. Conversely, if the error signal is not zero, the electronics send a signal to the piezoelectric mirror (16) to try to modify the cavity to bring the error signal back to zero. The electronics can be operated in *scan* and *lock* modes. In scan modes, the piezoelectric mirror resonates to find multiple modes to lock into. In lock mode, the electronics fix the piezoelectric mirror to a distance that makes the error signal go to zero and thus generation of the signal and idler beam occurs, by building the cavity length.

The second cavity that needs to be in resonance is based on the position of the crystal (13) and the filtering of the etalon (15). Once the pump beam is in resonance, the crystal position needs to be optimized without the etalon. Although the etalon helps the electronics lock onto a particular mode, it can also increase the complexity of tuning. Sequential optimization of crystal position, followed by etalon tuning, typically yields the most intense signal and idler beams. Alignment is crucial to operation of the OPO laser; it is for this reason that the alignment procedure will be discussed in more detail below.

OS 4000 Alignment

An illustration of the OPO laser is shown in Figure 2-14. The different parts are labeled 1 through 18. The Nd:YAG (2) housing should be previously aligned through the half-wave plate (6) and telescope (7) and onto the first steering mirror. Using an IR detection card, it can be verified that the laser is close to the center of the first steering mirror (8). Unless the OPO laser was physically impaired, this should still be at factory alignment. The IR detection card identifies the position of the beam by a color change on the card since the beam is invisible to the eye. The color change is opaque to green when the laser beamed is focused onto the card surface and can be used in all parts of the alignment process.

Before starting, there are a few things to keep in mind while aligning the cavity. 1) The beam needs to be perfectly horizontal from steering mirror 2 onward (10). 2) The beam going toward the crystal needs to be in perfect overlap with the returning beam. If the beam is not in perfect overlap, the return beam cannot reach the photodiode (5) and thus there is no error signal for the OPO to build the cavity. 3) It is recommended that the controls of the focusing lens (11) in the x and y direction, be close to the center of the possible range, this will give the user full range of focusing when the cavity is close to perfect alignment.

At this point, the laser needs to be turned on, which is done by turning the keys on the Nd:YAG control box and the OPO temperature control box. The set temperature should be at 50° C. It is imperative to allow the crystal to heat up, prior to turning the Nd:YAG laser on, as this could severely damage the crystal. Once the crystal reaches the desired temperature, the Nd:YAG laser can be turned on by the two green buttons

on the control box. After the Nd:YAG laser is on, the lock amplifier can be switched on, making sure that the lock amplifier is run in scan mode.

With the laser on, the two back steering mirrors (8 and 10) should be adjusted to raise the pump laser, while being detectable on the other side of the crystal. This part of the alignment is tedious and requires constant checks with the IR detection card to ensure that the beam is being moved in the correct direction. Once the beam is completely overlapped and can transverse the crystal cavity, the beam can then be moved in such a way that it reflects off of the first folding mirror (14). At this point, it is possible to see flashing green light. This corresponds to the non-phase-matched second harmonic generation at pump resonance, which is a sign that the laser is approaching a good alignment.

If flashing green lights are not visible, it is possible that the piezoelectric mirror (16) is not at the correct position. Using the IR detection card, the pump beam should be aligned with the piezoelectric mirror (16). Ideally, the pump beam should be at the center of the piezoelectric mirror; however, this may be difficult to accomplish and is not necessary to generate the signal and idler beams. When the incoming beam is directed on the piezoelectric mirror, the mirror can then be adjusted so that the incoming beam and reflected beam overlap. During this process, all the steering elements, 8, 10, and 16 have to be adjusted simultaneously, as adjusting one mirror will affect the path of the other two.

At this point, a pulsing green light should be visible. Using an oscilloscope, the diode monitor should indicate two or three strong resonance peaks per scan of the piezoelectric element. Once an ideal alignment is found, all of the elements need to be

tuned to increase the height of the most intense resonance peak, while decreasing the other peaks. Furthermore, the position of the crystal should be adjusted to find the most intense resonant peak height.

After the different elements are in the optimal position, based on the feedback from the oscilloscope, the instrument should be changed from scan mode to lock mode and the power should be monitored. Two methods can be used for tuning from here; either a fine tune can be done by barely adjusting the mirrors for optimal power or a detune can be performed on one optic and corrected for by another optic. Since each optic is not independent of one another, an optic can be ‘detuned’ by adjusting the position, resulting in a lower power, followed by a ‘retune’ with a different optic. The ‘detune retune’ process is a particularly useful strategy for increasing the power of the laser, just be sure not to completely detune the cavity as bringing the cavity back without feedback is a difficult process.

When optimal conditions are reached, the etalon can be installed at position 15. The etalon can be rotated clockwise or counter-clockwise in the housing and the angle can also be adjusted. It is suggested to find the optimal angle first, i.e. the angle that produces the most power, and then rotate the etalon to see if the power output can be increased. At this point, the procedure of tuning the cavity should be repeated, with the addition of adjusting the etalon to find the best alignment. This should be done first in scan mode to find the most intense resonance peak, then move to the lock position to tune for power. Keep in mind that adjusting the steering mirrors can change the ideal position of the crystal and the etalon, thus all the elements 8, 10, 11, 13, 15, and 16 may need to be adjusted.

After the cavity is in proper alignment, everyday tuning can be accomplished by adjusting the crystal position and the etalon alone; the inside cavity mirrors should require no further adjustment. The OPO can now be temperature tuned throughout an entire poling period (i.e., typically 50° – 125° C).

OS 4000 Operation

The ideal position of the crystal can first be found in scan mode, as introduced above, the resonance peaks indicate ideal position in each poling period. Therefore, in scan mode, the position of the crystal can be adjusted and the resonance peaks will increase and decrease based on position. Once larger resonance peaks are observed, the user can turn the lock amplifier from scan to lock mode and monitor the signal wavelength with a wavemeter. By comparison with Figure 2-15, the user can determine the poling period alignment of the cavity. If this is not the desired poling period, switch to scan and continue to move the crystal position until the next position where the resonance peaks are large again, switch from scan to lock and check the wavelength. Once the desired poling period is found, fine tune the crystal position and etalon position to generate the most power for the idler beam.

The lowest temperature to operate the OPO crystal is 50° C. The idler output wavelength as a function of crystal temperature is shown for all the poling periods in Figure 2-15. Adjacent modes are separated by 1.4 – 1.6 nm for the signal beam, or roughly 5 cm⁻¹ for the idler beam. This usually corresponds to a temperature change of 2° C or 3° C; however, this effect is not linear, and at higher temperatures, the temperature difference between modes is smaller.

A limitation of this laser set-up is the long time (~45 minutes) that it takes the crystal oven to cool down from 125° C to 50°C. For the sake of efficiency, it is best to

scan through the temperature range in one poling period by increasing the temperature, while scanning down in temperature in the following poling period.

Carbon Dioxide Lasers

The CO₂ laser used for IRMPD was a Synrad J48-5W. The laser operates at a fixed wavelength of 10.6 μm and can produce a laser beam at a maximum power of 25W. The beam waist at the laser aperture is approximately 3.5 mm and the beam divergence is 4 mrad. A divergence of 4 mrad corresponds to the beam waist expanding by 4 mm for each meter traveled. For the current set-up, the CO₂ laser is fixed directly behind the FT-ICR and the path from the aperture to the entrance of the ICR cell is approximately 0.25 m. Therefore, the estimated beam diameter is 4.5 mm inside the ICR cell.

The CO₂ laser operates by exciting a plasma tube with an rf frequency. The mechanism of the plasma tube works by first generating electrons to interact with nitrogen gas in a sealed tube. The electrons excite the nitrogen gas molecules to higher energy. As the nitrogen collides with CO₂ gas molecules in the tube, energy is transferred from N₂ to vibrational energy states of CO₂. If this transfer is efficient, it can result in a population inversion for CO₂, and the lasing action can begin. Helium gas is employed to collisionally cool the nitrogen gas back to the ground state so that the overall process can be repeated. The instantaneous power can be controlled by a pulse width modulation (PWM) of the rf drive circuit, specifically by adjusting the PWM to a fixed modulation frequency.

Carbon Dioxide Laser Operation

The operation of the CO₂ laser involves a power control box (PCB), the PWM, and a water chiller. There are two switches located on the CO₂ laser to turn the laser on,

and there is one switch on the PCB. The water supply lines are located next to the water supply lines for the turbo pump, located on the far side of the FT-ICR, and they need to be opened before the CO₂ laser is operated. Once the laser is on, the pulse length of the CO₂ is controlled by a transistor-transistor logic (TTL, +5 V) pulse that is sent from the instrument to the PCB. The pulse can be turned on by selecting the CO₂ option in the FT-ICR experiment workflow. This will pulse the CO₂ after the ions have been stored in the ICR cell, but before they are excited and detected. The typical pulse length is from 150 ms to 500 ms, but multiple pulse lengths should be tried to find optimized conditions. When the TTL pulse is applied to the PCB, another voltage is applied to the CO₂ laser, corresponding to the power percentage selected on the PCB. Higher percentages will cause larger voltages to be applied, and will change the PWM to generate more power from the laser.

For CO₂ laser assisted photodissociation experiments, start the laser power at the lowest possible setting on the PCB and slowly increase the power until fragmentation is observed. Once, non-wavelength specific fragmentation is observed, turn the power of the CO₂ down until the fragmentation is no longer observed. This is crucial to the IRMPD spectroscopy experiment because the only fragmentation observed should be induced by wavelength specific photons from the OPO laser; any other fragmentations reduce the specificity of the experiment. Furthermore, nonspecific fragmentation can increase the noise of the experiment, and reduce the overall signal to noise. The settings described above optimize the experiment for the best possible signal to noise.

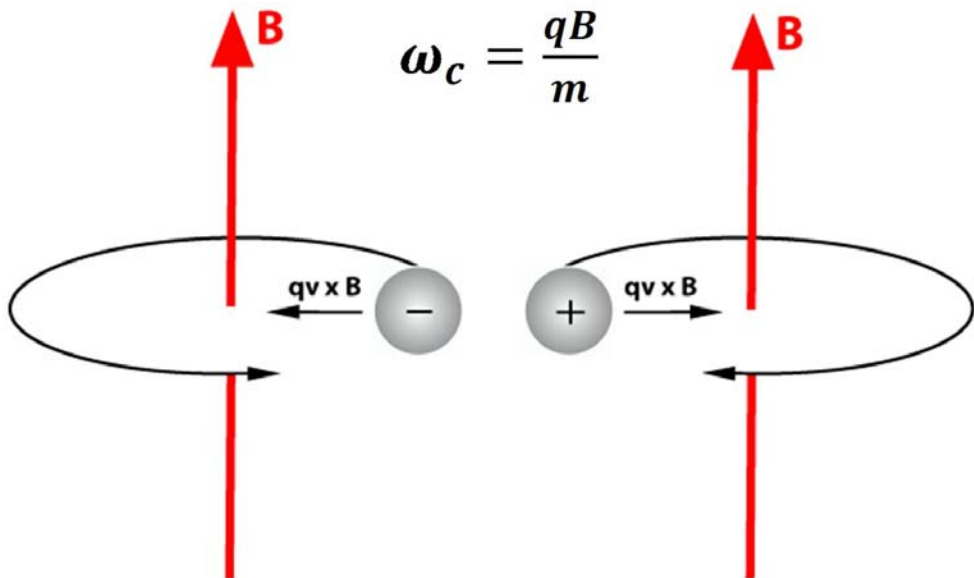


Figure 2-1. The cyclotron motion of negative and positive ions in a uniform magnetic field, B . The oscillation frequency is dependent on the charge of the ion, q , the magnetic field, B , and the mass of the ion, m . The inward force is the Lorentz magnetic force, defined by the charge of the ion, q , the magnetic field, B , and the velocity of the ion, v .

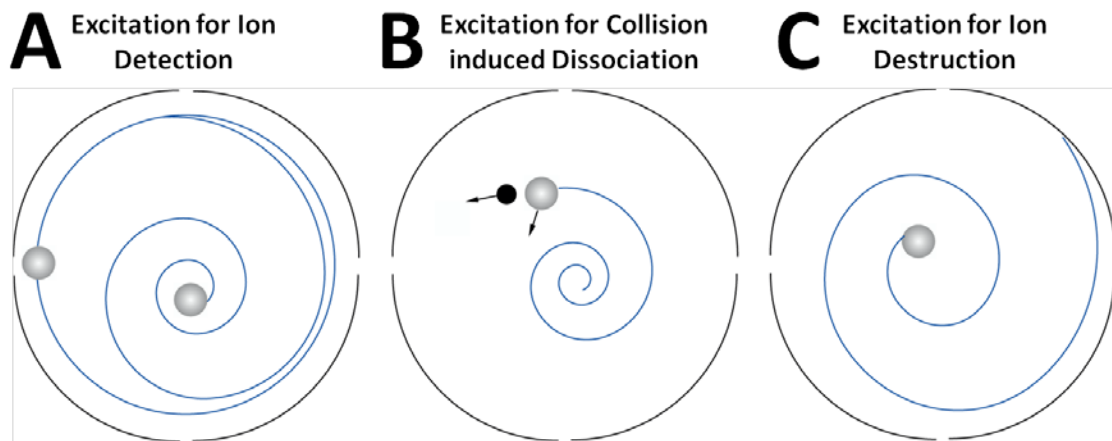


Figure 2-2. Illustration of the different excitation experiments that can be performed in the ion cyclotron resonance cell. A) Exciting the ions to a coherent radius for detection. B) Exciting the ions to a larger radius for collision induced dissociation. C) Exciting the ions to a radius larger than the cell radius to remove them.

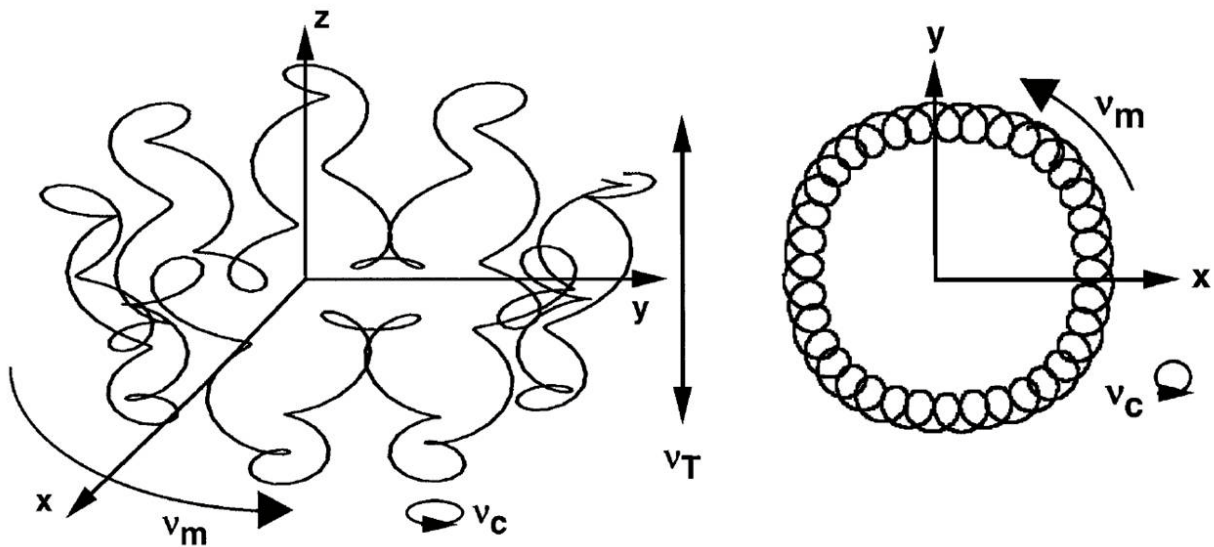


Figure 2-3. Motion of ions in an ion cyclotron resonance mass spectrometer. Left side: Three-dimensional motion of the ions inside the trap. Right side: Two-dimensional motion about the z axis in the trap. [Reprinted with permission from John Wiley & Sons, Ltd. Marshall, A.G.; Hendrickson, C.L.; Jackson, G.S. 1998. Fourier Transform Ion Cyclotron Resonance Mass Spectrometry: A Primer. Mass Spectrom. Rev. (Volume 17, Page 14, Figure 13).]

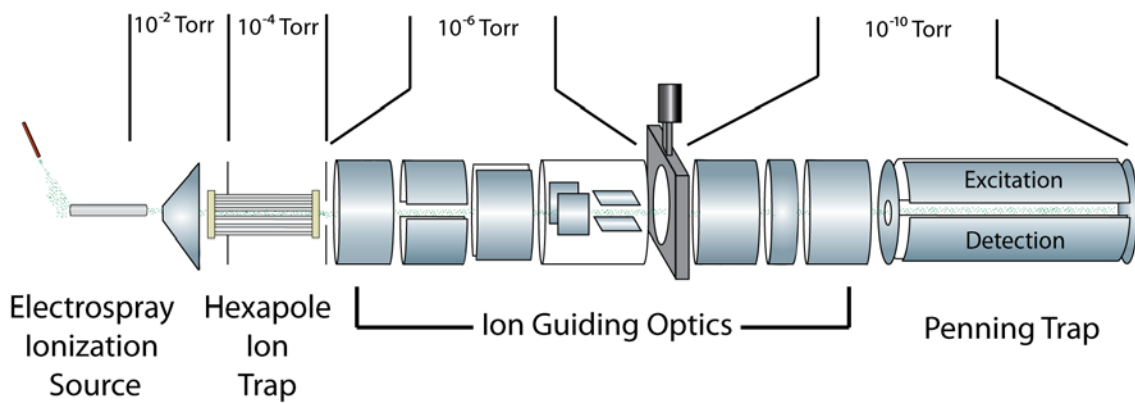


Figure 2-4. An illustration of the basic components of the Bruker Apex II Fourier transform ion cyclotron resonance mass spectrometer. The Penning trap is located inside the bore of the super-conducting magnet.

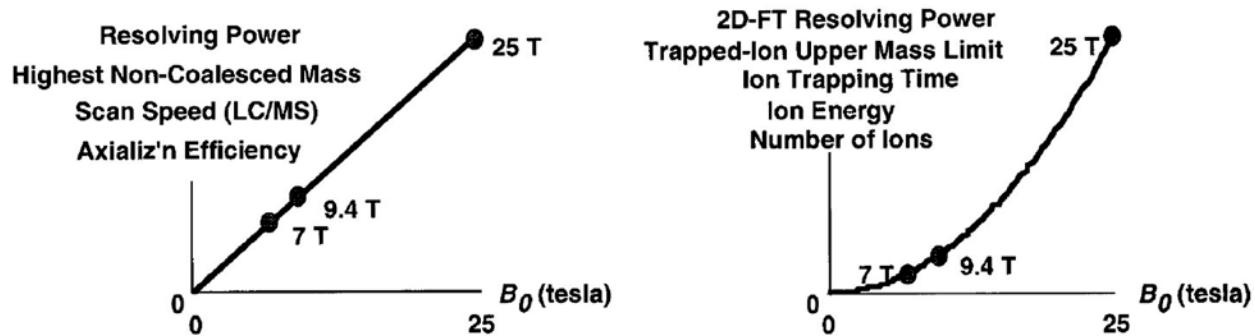


Figure 2-5. FT-ICR performance as a function of magnetic field strength. Left side displays parameters that increase linearly. Right side displays parameters that increase quadratically. [Reprinted with permission from John Wiley & Sons, Ltd. Marshall, A.G.; Hendrickson, C.L.; Jackson, G.S. 1998. Fourier Transform Ion Cyclotron Resonance Mass Spectrometry: A Primer. Mass Spectrom. Rev. (Volume 17, Page 22, Figure 19)]

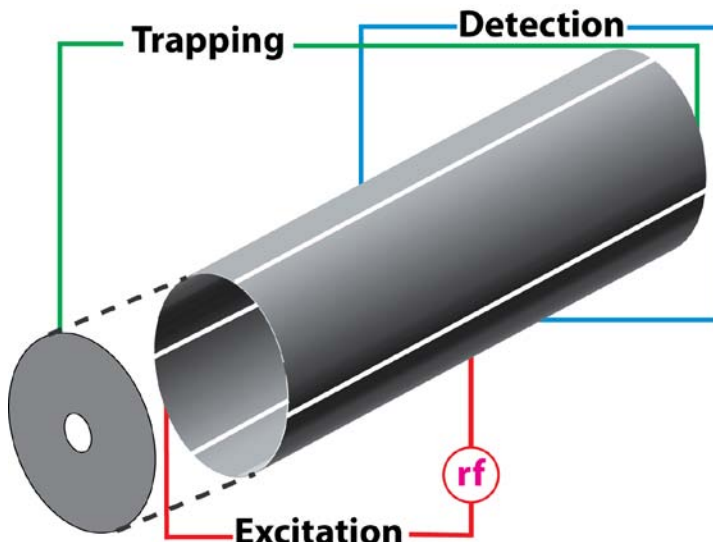


Figure 2-6. Schematic representation of a cylindrical ion cyclotron resonance cell. The cell contains 3 pairs of plates: trapping, excitation, and detection.

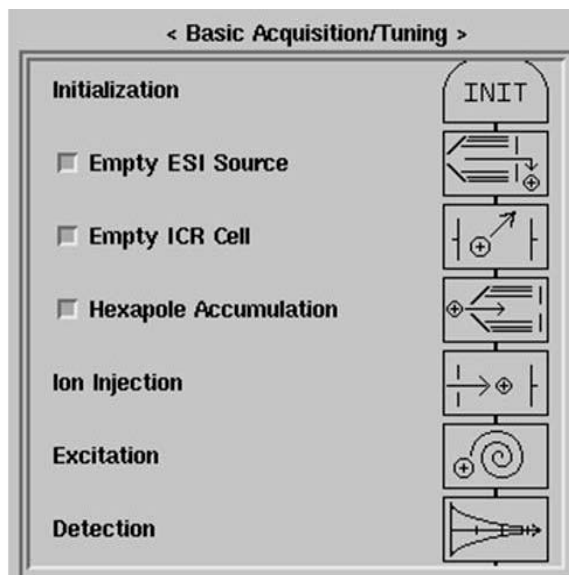


Figure 2-7. Screenshot from Xmass™ software workflow to illustrate basic components of experiment

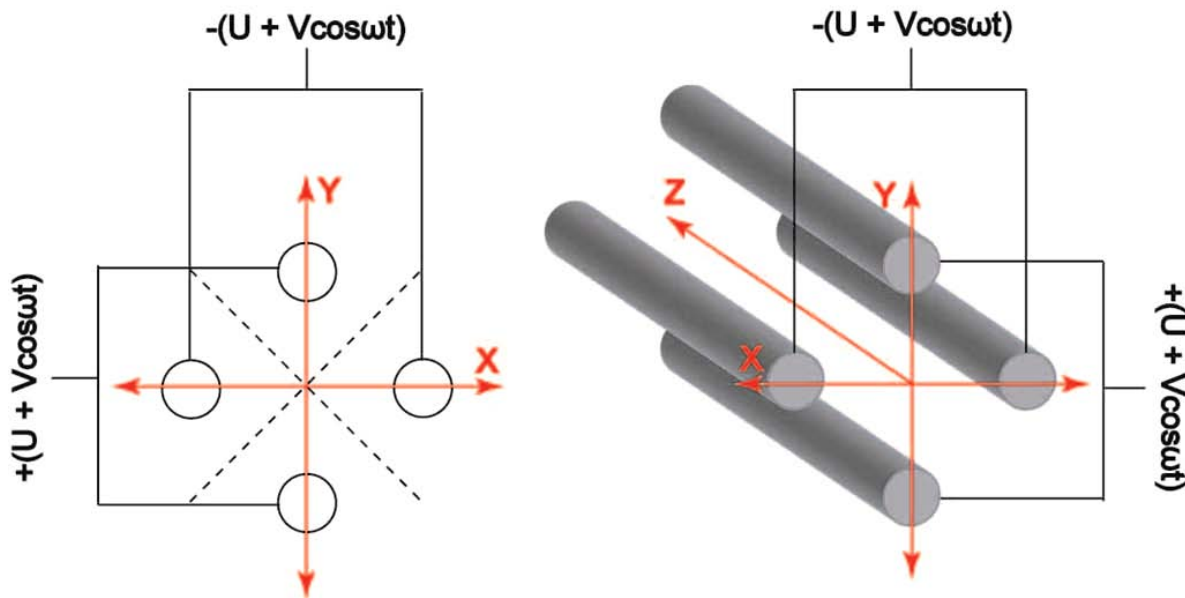


Figure 2-8. A schematic of a quadrupole mass filter. Left side: Looking down the z-axis of a quadrupole mass filter. The field applied is opposite polarity across the x and y planes. The dashed line indicates the field free region in the mass filter. Right side: Three-dimensional view of the quadrupole mass filter.

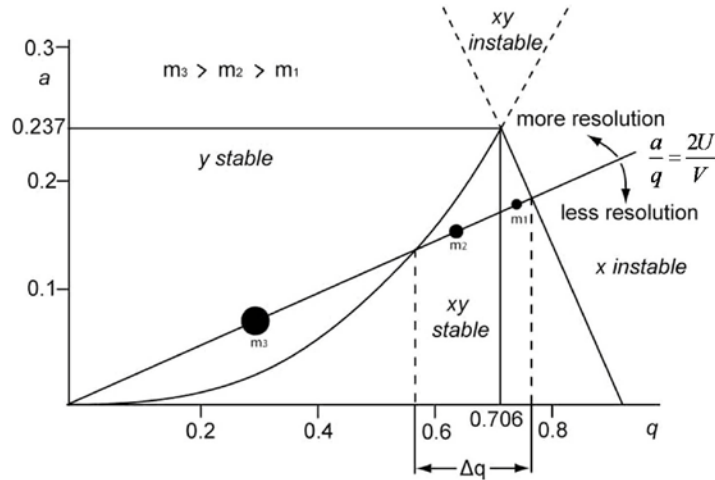


Figure 2-9. Stability diagram of a linear quadrupole mass filter. [Adapted with permission from John Wiley & Sons, Ltd. Dawson, P.H.. 1986. Quadrupole Mass Analyzers: Performance, Design, and Some Recent Applications. Mass Spectrom. Rev. (Volume 5, Pages 1-37)]

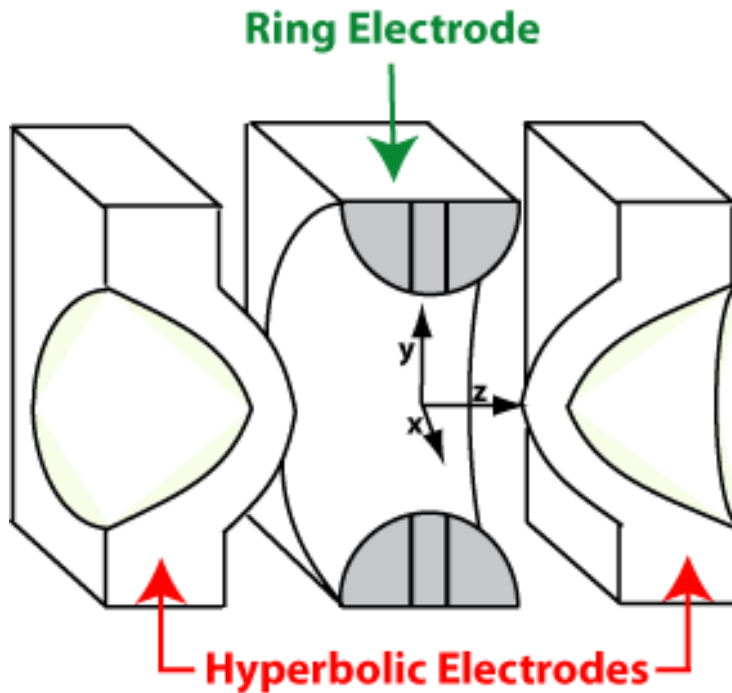


Figure 2-10. Schematic of a quadrupole ion trap (QIT). The QIT contains three electrodes: two hyperbolic end-cap electrodes and a ring electrode.

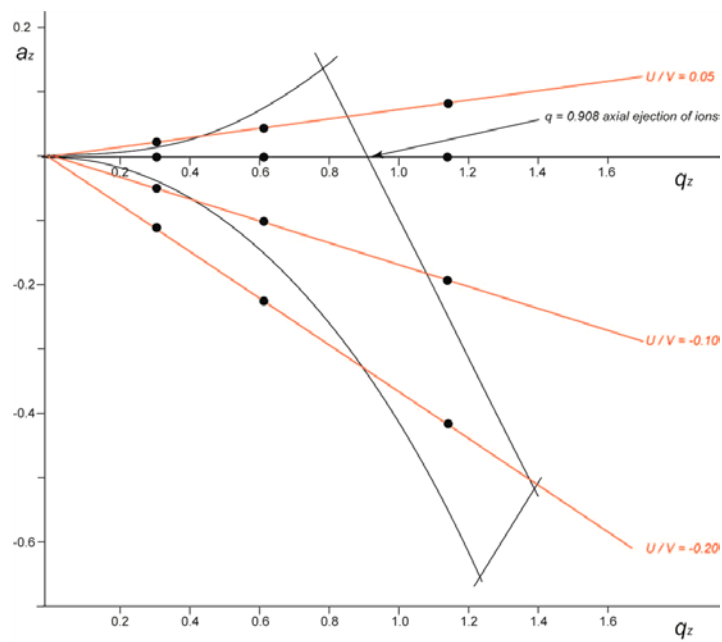


Figure 2-11. Stability diagram of the quadrupole ion trap. [Adapted with permission from John Wiley & Sons, Ltd. March, R.E. 1997. An Introduction to Quadrupole Ion Trap Mass Spectrometry. J. Mass Spectrom. (Volume 32, Pages 351-369)]

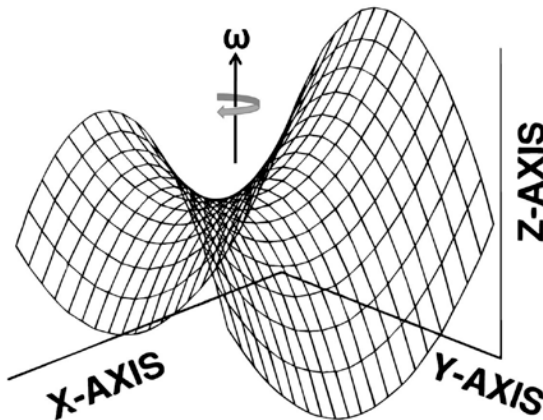


Figure 2-12. Visualization of the electric field applied in the quadrupole ion trap. [Taken with permission from John Wiley & Sons, Ltd. March, R.E. 1997. An Introduction to Quadrupole Ion Trap Mass Spectrometry. J. Mass Spectrom. (Volume 32, Pages 351-369)]

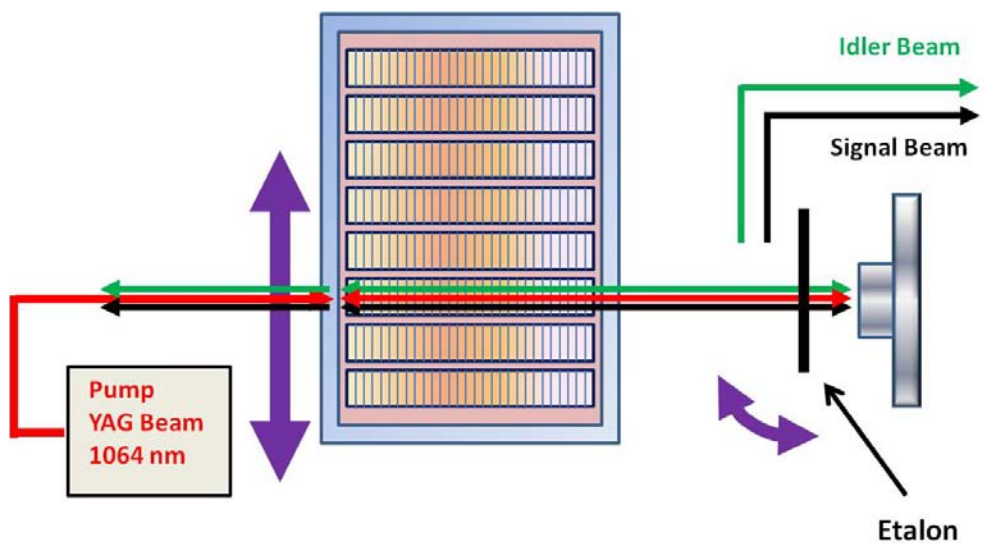


Figure 2-13. Cartoon illustrating the general operation of the optical parametric oscillator laser.

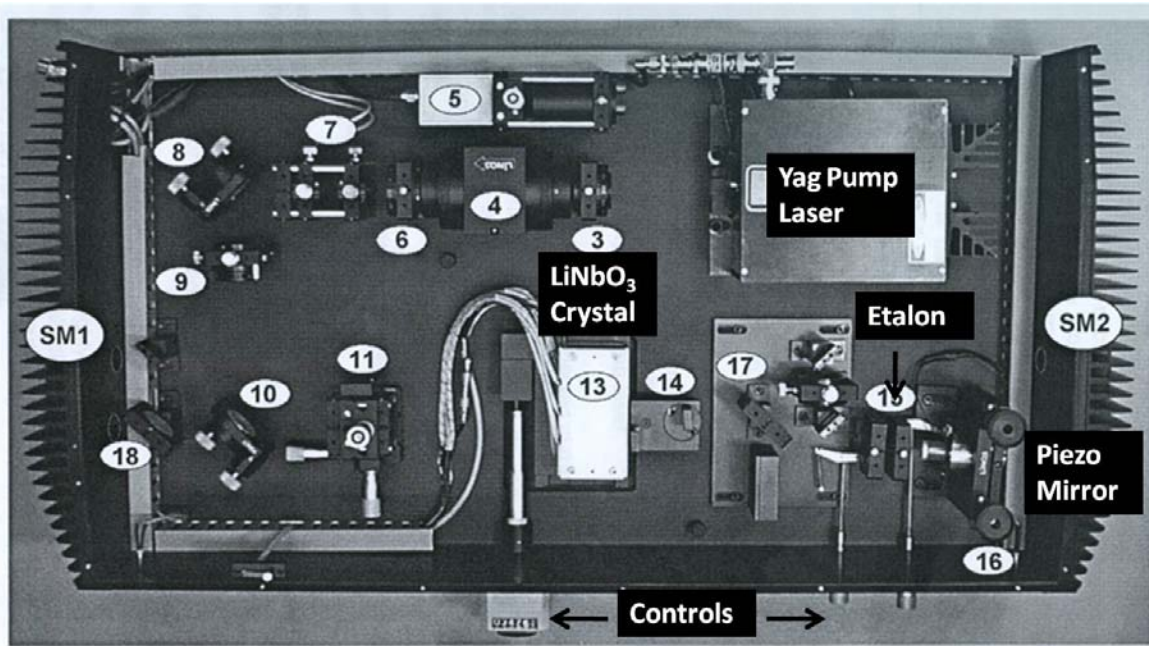


Figure 2-14. Photograph of the optical parametric oscillator cavity. Nd:YAG pump laser (3,6) quarter- / half- waveplate and half -wave plate polarizers (4) Faraday isolator (5) photodiode unit (7) telescope (8) pump beam steering mirror (9) iris (10) beam splitting steering mirror (11) three-stage focusing lens (13) oven with PPLN LiNbO₃ crystal (14) folding mirrors (15) etalon (16) piezo-mounted mirror (17,18) first and second beam separators and the controls for the crystal position (left) and etalon angle (right). [Adapted with permission from LINOS, LINOS OS4000 operators manual, Frank Mueller].

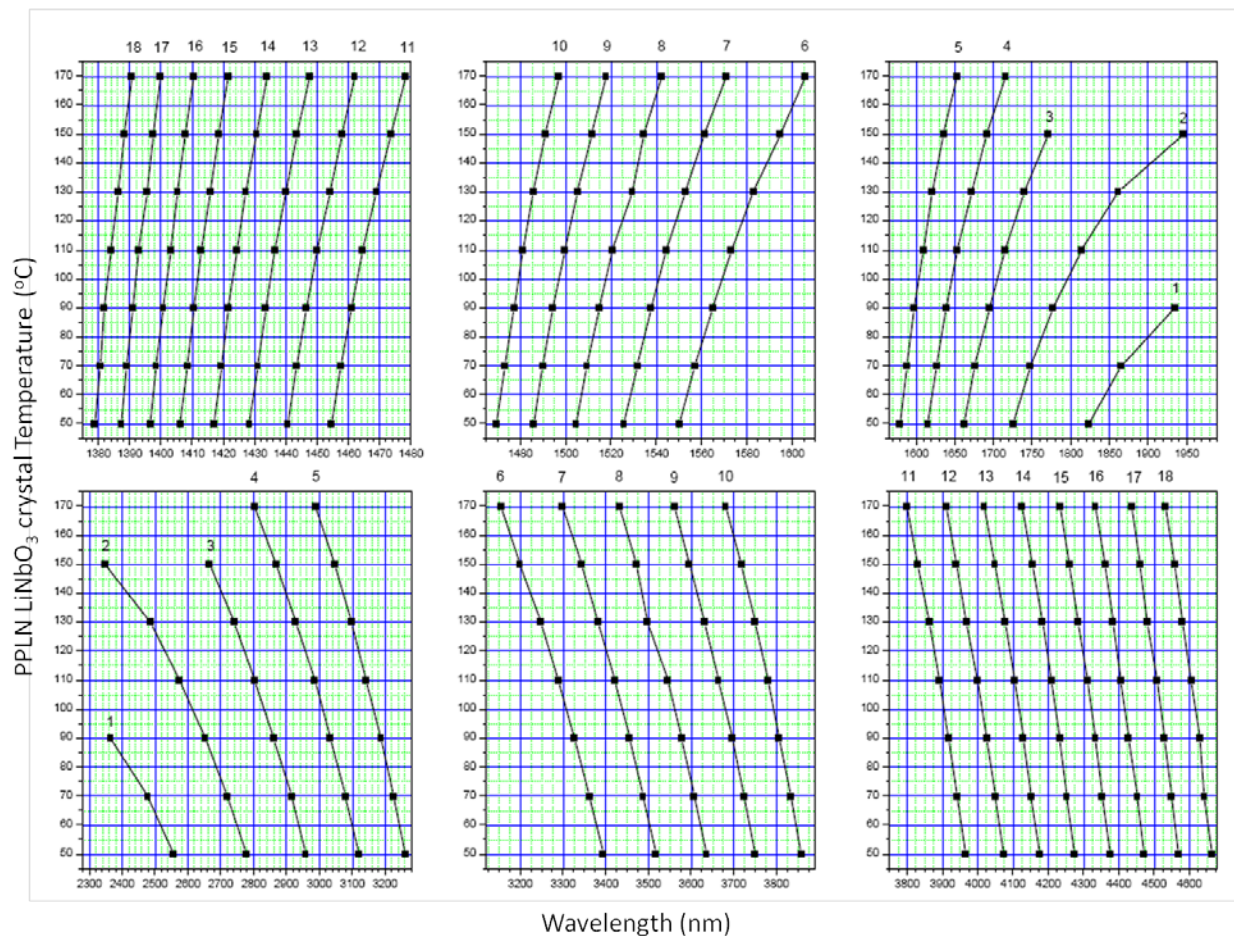


Figure 2-15. Plot of signal (top) and idler (bottom) wavelength dependence on temperature of the crystal through all the poling periods of the OPO laser.
[Adapted with permission from LINOS, LINOS OS4000 operators manual, Frank Mueller]

CHAPTER 3

VIBRATIONAL SIGNATURE OF ZWITTERIONIC AND CHARGE-SOLVATED STRUCTURES FOR ALKALINE EARTH TRYPTOPHAN DIMER COMPLEXES IN THE GAS PHASE

Introduction

Tryptophan-metal cation complexes are known to play key roles in biological function. For example, tryptophan exists in the entrance/exit¹⁰⁹ and selectivity filter¹¹⁰ regions of ion channel proteins. Furthermore, tryptophan has been shown to be associated with the gating function in gramicidin-A¹¹¹ and gramicidin-S ion channels,^{112,113} as well as the Ca²⁺ channel in N-methyl-D-aspartate.¹¹⁴

Gas-phase studies can characterize inherent amino acid-metal cation interactions without the presence of solvent effects. Tryptophan has multiple binding sites, such as electrostatic interactions with the three Lewis-basic heteroatoms (amino N and carboxylic acid O's) and a cation-π interaction with the aromatic indole side chain. In addition to binding patterns, tryptophan can bind in the zwitterionic or charge-solvated (non-zwitterionic) forms, leading to numerous conformations. Figure 3-1 and Figure 3.2 show the most stable binding motifs for the monomer Ba²⁺Trp and the dimers M²⁺Trp₂, where M is Mg, Ca, Sr, and Ba, calculated with density functional theory (DFT). For this chapter, structures will be referred to as either Z for zwitterionic or C for charge solvated, followed by a number. The number represents the ranking of the structures calculated energy. For example, the structure Z2 is zwitterionic, and is the second lowest energy structure. This nomenclature was adapted from the literature.¹¹⁵

Infrared multiple photon dissociation (IRMPD) spectroscopy¹¹⁶⁻¹²⁰ is a powerful tool in distinguishing Z and C forms. The majority of previous studies have made use of free electron lasers (FELs), which are continuously tunable and have high power throughout

the infrared spectrum (typically 500 cm^{-1} through 2000 cm^{-1}). This region of the IR spectrum includes the C-specific carboxylic acid C=O stretch, as opposed to the Z-specific anti-symmetric carboxylate CO_2^- stretch. Previous studies have shown amino acids and small peptides complexed with singly-charged metal cations predominantly adopt C gas phase structure.¹²¹⁻¹³⁵ Basic amino acids, such as arginine,^{121,125,136,137} proline,¹²⁰ and lysine,¹³⁸ have been shown not to follow this trend. Serine¹³⁴ and methionine¹³⁹ also have shown to be Z when bound to larger metal ions (i.e., Rb^+ and Cs^+). Although monovalent metal ions predominantly bind to C structure amino acids, divalent metal ions, specifically Ba^{2+} , have been shown to completely stabilize the gas phase Z form.^{140,141} These studies have since been expanded to investigating dimeric divalent metal ion complexes and the size effect of metal cation on Z stabilization.¹⁴⁰ Compared to the monomeric complexes, the dimer IRMPD spectra exhibit increased spectral congestion, complicating interpretation because the CO_2^- and C=O diagnostic stretching begin to overlap with other vibrational modes of the ion.

Initial studies suggested that the carboxylate group can solvate larger metals more effectively, thus promoting the Z structure.¹²¹ These trends were measured and confirmed by IRMPD spectroscopy.^{125,136} Similar trends were also shown for metal complexed serine¹³⁴ and methionine.¹⁴² Dunbar et al. also predicted that divalent metal cations would stabilize the Z form, based on the relative binding energies, i.e., Ca^{2+} , Sr^{2+} , and Ba^{2+} would favor Z, but Mg^{2+} would not.¹⁴⁰ Furthermore, studies by Bush et al. found that Ba^{2+} chelated arginine, glutamine, proline, serine, and valine all favored the Z structure.¹⁴³

In the work discussed in this chapter, a bench-top continuous-wave (cw) optical parametric oscillator (OPO) laser was employed to differentiate between C and Z $M^{2+}Trp_2$ structures by investigating the O-H and N-H stretching regions (3000 cm^{-1} – 3700 cm^{-1}). Despite the usefulness of this region to distinguish C and Z structures, based on the C-diagnostic carboxylic acid O-H and the Z-diagnostic NH_3^+ stretching modes, relatively few studies have made use of OPO lasers for IRMPD spectroscopy.^{141,144,145} Most of the infrared photodissociation experiments using OPO lasers have been on tagged complexes^{146–152} or solvated clusters,^{118,153} which have low dissociation thresholds. Rizzo et al. pioneered an infrared-ultraviolet photodissociation involving an OPO, where UV photons cause dissociation, but prior absorption of an IR photon leads to a dip in the photodissociation yield.¹⁵⁴ The OPO laser used in the work reported here is capable of inducing covalent bond cleavage, particularly in combination with a high-power CO₂ laser. The work discussed here follows up previously reported, where IRMPD spectra of Rb⁺ complexed carbohydrates were measured with the OPO laser.¹⁵⁵ Furthermore, the output ranges of the OPO laser corresponds to vibrational spectra that are not as congested as those accessed by the FELs, given that the C O-H diagnostic stretch and Z NH_3^+ diagnostic stretch are separated by 250 to 300 cm^{-1} in these complexes, allowing for a more straightforward assignment of structure. It is in this way that the OPO region of the infrared can be regarded as a fingerprint region for identifying C or Z gas-phase structure.

Procedure

Materials

Standard compounds of Mg(NO₃)₂, Ca(NO₃)₂, Sr(NO₃)₂, Ba(NO₃)₂, and L-Trp (all from Acros Organics) were dissolved in HPLC-grade water (Fisher Scientific) at a

concentration of 10^{-2} M to prepare the stock solutions for the experiments. Stock solution of the L-Trp was then mixed with each of the metal stock solutions at a 1:1 ratio. The solution was then further diluted to a concentration of 10^{-3} M for both the metal and L-Trp, and the solvent was a 70:30 mixture of methanol/water.

Mass Spectrometry and Ion Spectroscopy

The Ba^{2+}Trp and $\text{M}^{2+}\text{Trp}_2$ complexes were formed by electrospray ionization (ESI) in a commercial 4.7 T Apex II Fourier transform ion cyclotron resonance (FT-ICR) mass spectrometer (Bruker Daltonics, Billerica, MA) as described in chapter 2. The ESI conditions can significantly change the precursor ion spectrum on this instrument, and care must be taken when tuning these parameters. For example, the dimer complex, $\text{Ba}^{2+}\text{Trp}_2$, is much more weakly bound than that of the monomer complex, Ba^{2+}Trp . Therefore, parameters such as the capillary exit voltage can cause unwanted fragmentation, which can deplete the dimer $\text{Ba}^{2+}\text{Trp}_2$ into the monomeric form. Therefore, when making the dimer complexes, an attempt to make the conditions as gentle as possible, without sacrificing total ion current, must be made. Furthermore, hexapole accumulation times and pulse timing from the hexapole to the ICR cell play a major role in the precursor ion spectrum. Typically for these experiments, hexapole accumulation times of 2 seconds were used, and the extract pulse was set to 800 μs to 1200 μs depending on the mass to charge of the ion of interest (shorter extraction pulses favor smaller ions).

Once experimental conditions were optimized, all other ions except for the ion of interested were ejected from the trap using a correlated sweep excitation. This excites all ions, except for the ion of interest, to a radius larger than the cell, causing loss of those ions. For the case when ions other than the precursor ion are still detected after

the correlated sweep, single frequency excitations can be performed, to eject the remaining ions, generating a clean precursor ion spectrum. This is crucial to IRMPD experiments, as “background” ion signal reduces the signal-to-noise ratio in these experiments, especially if they overlap with precursor ion dissociation pathways.

Once the precursor ion was mass isolated, infrared multiple photon dissociation (IRMPD) spectroscopy was performed by irradiating the precursor ion in a step-wise fashion with the tunable output (2500 cm^{-1} – 4000 cm^{-1}) of a continuous-wave (cw) periodically polled LiNbO_3 –optical parametric oscillator (OPO) OS4000 laser (LINOS Photonics, Germany). The IRMPD spectra were generated by plotting the power corrected IRMPD yield, $\text{yield} = -\ln[1 - \{\sum \text{int}_{\text{photofragments}} / (\sum \text{int}_{\text{photofragments}} + \sum \text{int}_{\text{precursor}})\}]$, as a function of the OPO idler wavenumber. The power correction was performed by multiplying the IRMPD yield by the ratio of the power at each wavenumber over the average power measured during the IRMPD experiment.

The main dissociation pathways observed from the IRMPD experiments were neutral loss of NH_3 , neutral loss of 2NH_3 , and loss of TrpH^+ . Irradiation times of 10 seconds with the OPO laser were used, and the laser fluence was estimated to be 2.4-4 J/cm^2 for a spot size of 0.25 cm^2 , even though the exact overlap between the ion cloud and the laser beam is unknown. In order to verify alignment from day to day, the indole N-H stretch for Ba^{2+}Trp served as a calibrant to optimize the beam overlap with the ion cloud. OPO laser irradiation was then followed by irradiation using a CO_2 (SYNRAD J48-5W, Mukilteo, WA) laser operated at 2 W, to boost IRMPD yield, which was particularly important for the weaker vibrational modes, e.g. the NH_3^+ stretching modes. The combination of two infrared lasers to photodissociate was first used by Lee and co-

workers.¹⁵⁶ Eyler and co-workers later implemented a scheme involving two CO₂ lasers in the Penning trap of an FT-ICR.¹⁵⁷

Calculations

Once experimental spectra are recorded, it is convenient to compare these spectra to theoretical spectra to determine gas-phase structure. For these results, theoretical structures and IR spectra were previously calculated with density functional theory (DFT), employing the B3LYP functional with a 6-31+g(d,p) basis set and a Stuttgart-Dresden (SDD) relativistic core potential on the metal for Sr and Ba¹¹⁵ with the Gaussian03 software package.¹⁵⁸ The SDD core potential has been reported to be adequate for calculating vibrational frequencies for metal-ion complexes.^{115,122,123} The computed vibrational frequencies were scaled by 0.975 and stick spectra were broadened with a Gaussian function to 30 cm⁻¹ FWHM (full width at half-maximum). The calculated spectra are plotted with band intensities in km mol⁻¹, which is directly related to the molar absorption coefficient of the structure at that particular wavenumber. The zero-point corrected energy (ZPE) is shown with each corresponding structure in Figures 3.5, 3.7 and 3.8.

The IRMPD results in the 3000–3700 cm⁻¹ region are contrasted to previously published IRMPD spectra in the mid IR-range 600–1800 cm⁻¹ using the free electron laser, FELIX,¹¹⁵ at the FOM Institute for Plasma Physics ‘Rijnhuizen’ coupled to a home-built FT-ICR mass spectrometer.⁵² In that study, complexes were generated by ESI and transferred to the Penning trap and irradiated with the FELIX beam.

Results and Discussion

Experimental Optimization

The primary goal of this research was to design an IRMPD spectroscopy experiment for routine analysis of gas-phase structure and optimization studies were first completed on the Ba²⁺Trp system. Figure 3-3 displays the depletion of the precursor ions into fragment ions as a function of OPO irradiation time. The chart demonstrates overall IRMPD yield increases as a function of laser irradiation time. Therefore, if a vibrational mode is weaker, and difficult to dissociate, it would be possible to increase the irradiation time until this mode is detectable. However, the plot illustrates that as the irradiation time increases beyond 5 seconds, the IRMPD gain is no longer linear, and at 10 seconds, there is no significant gain in IRMPD yield as a function of irradiation time. This deviation from linear behavior is most likely due to a migration of the ions away from the center of the ICR cell (in the form of an increased magnetron motion), thus reducing the overlap between the laser beam and the ion cloud.

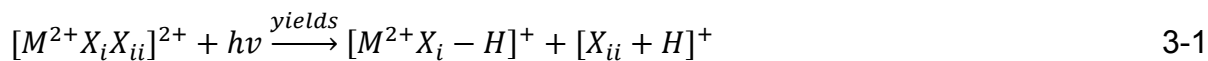
Since increasing irradiation time beyond 10 seconds has little effect on increasing fragmentation yield, other methods are required to improve dissociation yield, particularly for the weaker vibrational modes. Figure 3-4 shows an overlay of two experiments performed in the same wavenumber range of the OPO. The black line is a plot of the experiment with the OPO alone; the red line is a plot of the experiment with the photodissociation assisted by a fixed wavelength (10.6 μm) CO₂ laser. An important feature of this experiment is the fact that although two lasers are incorporated, there is no shift in the frequency of the bands in the spectrum. This shows that the CO₂ laser irradiation only affects the intensity and not the band position in the IRMPD spectrum.

The increase in photofragmentation results from resonant absorption of multiple photons with the OPO laser, which brings a population of ions to higher internal energies than room temperature, but lower energies than the dissociation threshold. Irradiation by the higher-power ($\sim 2\text{W}$) CO_2 laser for 500 ms raises the internal energy of a fraction of those ions above the dissociation threshold, thus inducing photodissociation. The overall gain from the CO_2 irradiation yields an increase from roughly 5% dissociation to close to 25%, giving a factor of 5 increase in signal. Although the noise is also increased in the experiment, the signal-to-noise ratio is still increased from 13 for the OPO alone to 32 by incorporating the CO_2 laser. Furthermore, the irradiation time for the OPO- CO_2 experiment was dropped to 5 seconds versus the previous 10 seconds of irradiation with the OPO alone. The point of 5 seconds was chosen as this was the point where linear gain in yield was lost and gave the best overall gain in signal versus time and significantly reduced the time required to measure an IRMPD spectrum.

Ba^{2+} Tryptophan Monomer Complex

The mass spectrum for the isolated $\text{Ba}^{2+}\text{+Trp}$ complex and the resulting MS/MS spectrum after irradiation with the OPO are shown in Figure 3-5. The precursor ion is selected by performing a correlation sweep (top), which applies a scan of rf frequencies, excluding the frequency at which the precursor is oscillating. In the event that unwanted ions remain in the trap, specific frequencies can be reapplied to the trap to eject the remaining unwanted ions, resulting in single m/z isolation. The fragment ion spectrum (bottom) is shown for an OPO irradiation set to 3475 cm^{-1} . Ammonia loss is the most abundant IRMPD product. Other photodissociation products include the charge

separation products $[\text{Trp}+\text{Ba}-\text{H}-\text{NH}_3]^+$, $[\text{Ba}+\text{C}_2\text{H}_2\text{NO}_2]^+$, and $[\text{Trp}-\text{C}_2\text{H}_2\text{NO}_2]^+$. The general mechanism for a charge separation reaction can be seen in equation 3-1.



Note that for the tryptophan complexes, M is the metal ion and X is tryptophan.

Charge separation reactions are common in multiply charged gas-phase ions;^{115,159-162} however, the exact mechanism of this processes is still under investigation. Work is currently being done on more simple systems, such as H_2O complexed metals, to gain an understanding of the charge separation process in those systems, before it is applied to larger systems, such as amino acids.¹⁶³

The laser frequency of 3475 cm^{-1} resulted in the most intense fragmentation, which suggests that there is an IR active mode at this wavenumber. This particular frequency suggests an indole N-H stretching mode; however, comparison with theoretical spectra can aid in the identity of chemical specific absorption.

In Figure 3-6, the IRMPD spectrum of Ba^{2+}Trp is compared to four of the calculated lowest-energy Z and C isomer structures. Three characteristic stretching modes are predicted in the calculated Ba^{2+}Trp IRMPD spectra—(1) O-H stretch from the carboxylic acid terminus, $3525\text{--}3625\text{ cm}^{-1}$, highlighted in blue, (2) N-H stretch from the indole on the tryptophan side chain (this is expected for all structures), $3450\text{--}3500\text{ cm}^{-1}$, highlighted in red (3) N-H stretches from the amine NH_2 or NH_3^+ groups, $3150\text{--}3375\text{ cm}^{-1}$, highlighted in yellow. Note that, although absorption is expected for both C and Z structures in the N-H stretching (yellow) region, the spectral brightness of the two C NH_2 stretches is predicted to be much lower when compared to the Z NH_3^+ stretches (21 and 19 km mol^{-1} vs. 151 and 101 km mol^{-1}).

Comparison of the experimental IRMPD Ba^{2+}Trp spectrum with calculated spectra suggests that the complex adopts a Z structure, based on the lack of an O-H stretching mode and the presence of a doublet feature at 3290 cm^{-1} and 3320 cm^{-1} , consistent with the antisymmetric NH_3^+ stretching modes. Among the Z conformations, Z3 and Z4 predict an intense symmetric NH_3^+ mode (at 3170 cm^{-1} and 3150 cm^{-1} , respectively), while Z1 does not. Clearly, no mode is observed at this position, which suggests that exclusively Z1 is present. Thermochemically, Z3 is slightly favored relative to Z1 ($+2 \text{ kJ mol}^{-1}$); however, this is within the error of the calculation. Structurally, Z1 and Z3 differ in the orientation of the indole side-chain. This suggests that both structures cannot interconvert readily and supports the hypothesis that exclusively Z1 is present.

An alternative explanation for the lack of fragmentation for the symmetric NH_3^+ stretching mode might be due to experimental constraints, including lower laser power and lower energy per photon at this wavelength. In the IRMPD spectrum, the amine N-H stretching vibrations are reduced in intensity compared to the indole N-H stretch, as expected from the calculated linear absorption spectra. The NH_3^+ modes are likely to be more anharmonic in character than the indole N-H stretch, thus contributing to this reduction in intensity in the IRMPD yield. The additional use of a higher-power CO_2 laser is thus found to be particularly useful to boost the IRMPD yield of weak features in the spectrum. This approach resulted in appreciable IRMPD yields for the weaker antisymmetric NH_3^+ bands at 3290 cm^{-1} and 3320 cm^{-1} , approaching 25% (Figure 3-4). Nonetheless, this dual-laser approach did not yield any detectable photodissociation in the symmetric NH_3^+ stretching region.

In summary, the hydrogen stretching region confirms that Ba²⁺Trp exclusively exists in the Z form, consistent with the presence of a predominant Z1 conformation. In fact, Ba²⁺Trp had been investigated previously in the mid-IR region, using the free electron laser FELIX¹⁴⁰. In that study, the antisymmetric CO₂⁻ stretch (1675 cm⁻¹) and the NH₃⁺ umbrella mode (1450 cm⁻¹) yielded strong evidence for the exclusive presence of Z1, which could in fact be considered as a ‘fingerprint’ for the Z structure. Similarly, the corresponding spectrum in the OPO laser range presented here can be considered as a Z ‘fingerprint’ IRMPD spectrum, based on the lack of O-H stretching and presence of diagnostic NH₃⁺ stretching modes.

Alkaline Earth Tryptophan Dimer Series

The IRMPD spectra recorded over the 3000–3700 cm⁻¹ range for a series of dimeric M²⁺Trp₂ complexes (where M= Mg, Ca, Sr, and Ba) are compared in Figure 3-7. All spectra exhibit intense indole N-H and carboxylic acid O-H stretches. The presence of a carboxylic acid O-H stretching band in all IRMPD spectra confirms that at least one tryptophan is in the C configuration. The most striking difference between the IRMPD spectra is the presence of a weak (yet discernible) band at 3340 cm⁻¹ for the Mg²⁺Trp₂ and Ca²⁺Trp₂ complexes (see insert), as opposed to an absence of this band in the corresponding Sr²⁺ and Ba²⁺ complexes. As all dimer complexes exhibit efficient photodissociation, the presence of this additional band indicates a structural change between smaller and larger alkaline earth complexes. Based on the Ba²⁺Trp monomer results, the most likely assignment of the 3340 cm⁻¹ band is an NH₃⁺ stretch mode, indicative of a Z structure. At first sight, this suggests a mixed C/Z structure for Mg²⁺Trp₂ and Ca²⁺Trp₂, as opposed to a C/C configuration for the larger cation complexes, Sr²⁺Trp₂ and Ba²⁺Trp₂.

The structural changes are accompanied by differences in the photodissociation pathways. The mass spectra for the four systems can be seen in Figure 3-8. The spectrum shown for each complex is the most intense fragmentation spectrum from the entire IR frequency scan. For the $Mg^{2+} + Trp_2$ complex, the irradiation was performed at 3540 cm^{-1} . The $Ca^{2+} + Trp_2$ was recorded at 3495 cm^{-1} . $Sr^{2+} + Trp_2$ and $Ba^{2+} + Trp_2$ were irradiated at 3490 cm^{-1} . Results suggest a trend from exclusive neutral losses of NH_3 for Mg^{2+} to exclusive $TrpH^+$ loss for Ba^{2+} (the loss of 2 NH_3 was exclusively observed for Mg^{2+} and Ca^{2+}). Ca^{2+} and Sr^{2+} dimers exhibit both pathways, going from 90% NH_3 vs. 10% $TrpH^+$ loss for Ca^{2+} , to 60% NH_3 vs. 40% $TrpH^+$ loss for Sr^{2+} .

This gradual shift from NH_3 loss to $TrpH^+$ loss is compatible with the decreasing tryptophan-(divalent metal) cation binding energy as the size of the cation increases, as shown by Dunbar and co-workers.¹¹⁵ For the more tightly bound smaller alkaline earth cations, covalent bond cleavage leading to NH_3 loss is favored over $TrpH^+$ loss. With increasing alkaline earth cation size, the loss of $TrpH^+$ is progressively enhanced, as expected from a reduced cation binding energy.

Direct correlation between dissociation pathways and molecular structure is not as straightforward as IRMPD spectroscopy results. Jockusch et al. had first shown a correlation between NH_3 loss (diagnostic for Z) and H_2O loss (diagnostic for C) channels for the alkali series bound to arginine,¹²¹ suggesting that the transition from C to Z occurred from Na^+ to K^+ . Later spectroscopic studies by Bush et al. confirmed that the transition in fact occurs between Li^+ and Na^+ .¹³⁶ Although both approaches show a qualitative agreement that smaller alkali metal complexes adopt the C structure, as opposed to the Z structure for larger complexes, there are differences in the quantitative

analysis. The discrepancy between neutral loss branching ratios and spectroscopic results was ascribed to structural isomerization between the C and Z structures, which is lower in energy than covalent bond cleavage. In other words, the branching ratios in the dissociation pathways are more indicative of the transition states for the various complexes, than the actual presence of particular complexes at room temperature. Similarly, in the results presented here, the branching ratios between NH_3 and TrpH^+ loss for the $\text{M}^{2+}\text{Trp}_2$ series might suggest a gradual transition from Z-containing dimers for the smaller cations to exclusive C configuration for the $\text{Ba}^{2+}\text{Trp}_2$ complex. The IRMPD results seem to confirm this general trend, but indicate a more sudden transition from Ca to Sr, where no Z conformers are confirmed for Sr.

The exclusive presence of C/C for the $\text{Ba}^{2+}\text{Trp}_2$ and $\text{Sr}^{2+}\text{Trp}_2$ dimers, as opposed to exclusive Z for Ba^{2+}Trp monomer seems surprising. Moreover, the trend that smaller metal cations more readily stabilize the Z configuration, whereas larger cations do not, runs counter to most previous studies for alkali cations. The detailed spectral analysis of $\text{Ba}^{2+}\text{Trp}_2$ and $\text{Ca}^{2+}\text{Trp}_2$ complexes is shown hereafter to confirm the spectral assignments that are made. These results are also contrasted to a previous IRMPD study using the free electron laser FELIX.

Ba^{2+} Tryptophan Dimer Complex

Figure 3-9 compares IRMPD spectra recorded using FELIX (previous study)¹¹⁵ and the OPO- CO_2 laser scheme for $\text{Ba}^{2+}\text{Trp}_2$ with lowest-energy calculated isomers. The red arrow in the FELIX spectrum denotes the position of the fixed wavelength CO_2 laser, and confirms that $\text{Ba}^{2+}\text{Trp}_2$ does not exhibit a strong vibrational band resonant with the CO_2 laser. The same color scheme employed in Figure 3-6 is shown in Figure 3-9 for the carboxylic acid (blue), indole N-H (red) and NH_3^+ stretching modes (yellow).

The major difference between the $\text{Ba}^{2+}\text{Trp}_2$ and Ba^{2+}Trp experimental spectra is the presence of an intense O-H stretching band (3550 cm^{-1}). This suggests that at least one tryptophan is in the C form, and in principle allows for either C-only or mixed C/Z dimers. The calculated spectra for the lowest-energy conformers for each of these, C1/C1 and C1/Z3, are shown. In both cases, a carboxylic acid O-H stretch is predicted at 3550 cm^{-1} . The intensity of this band is intrinsically higher in the case of C1/C1, as there are two underlying oscillators, as opposed to just one in the case for C1/Z3; however, the discrimination between C1/C1 and C1/Z3 is difficult to make based on the intensity of the carboxylic acid O-H stretch band.

A more diagnostic difference between C1/C1 and C1/Z3 is seen in the intensities of their respective N-H stretching modes in the yellow region of the spectrum. Analogously to the Ba^{2+}Trp monomer, the amino NH_2 antisymmetric and symmetric stretching bands for the C structure are much weaker in intensity than the corresponding NH_3^+ bands (10 and 30 km mol^{-1} vs. 95 and 60 km mol^{-1}). The failure to observe N-H stretching modes in the $3100\text{--}3400 \text{ cm}^{-1}$ range suggests that neither of the tryptophans in the dimer is in the Z form. Note that, although weak, the NH_3^+ -associated bands in the more strongly-bound Ba^{2+}Trp monomer in Figure 3-5 (i.e., requiring covalent bond cleavage) were clearly detected. The failure to detect the loss of a protonated tryptophan for the more weakly-bound $\text{Ba}^{2+}\text{Trp}_2$, suggests that no Z structure is present. The lower dissociation threshold of the $\text{Ba}^{2+}\text{Trp}_2$ complex is validated by observing 3 times greater fragmentation yield for the indole N-H stretch vs. the corresponding fragmentation yield for the Ba^{2+}Trp , under identical laser irradiation conditions.

It is somewhat unexpected that $\text{Ba}^{2+}\text{Trp}_2$ exclusively forms C/C, since the monomer spectrum suggested a single Z form. In a previous FELIX IRMPD study of $\text{Ba}^{2+}\text{Trp}_2$ (shown on the Figure 3-9, left-hand-side),¹¹⁵ the experimental spectrum appears to resemble the C1/Z3 calculated spectrum more closely than the C1/C1 spectrum. In that latter study, the carboxylic acid C=O and carboxylate antisymmetric CO_2^- stretch served as diagnostic peaks to distinguish between C and Z. Increased spectral congestion of dimer complexes resulted in spectral overlap of both diagnostic bands, which can complicate spectral interpretation. Nonetheless, since the thermochemistry predicts the complexes to be very close in energy (+7 kJ mol⁻¹), it is conceivable that different mixtures of isomers were made by ESI in the two experiments. With respect to the thermochemistry results, it should be noted that the accuracy of the calculations is certainly limited. In all cases for these alkaline earth-tryptophan dimers, the mixed dimer C/Z is consistently predicted as the most stable configuration.¹¹⁵ For $\text{Ba}^{2+}\text{Trp}_2$ this is clearly not confirmed. Moreover, the IRMPD spectra suggest structural differences between the smaller and larger alkaline earth complexes, which are not predicted by the thermochemical results.

Ca²⁺ Tryptophan Dimer Complex

Figure 3-10 shows a comparison of the $\text{Ca}^{2+}\text{Trp}_2$ experimental spectrum recorded using FELIX¹¹⁵ and the OPO laser with calculated spectra for the three lowest-energy motifs. The chemically diagnostic wavelength regions are highlighted, as previously done in Figure 3-6 and Figure 3-9. Similarly to $\text{Ba}^{2+}\text{Trp}_2$, an intense O-H stretch at 3550 cm⁻¹, associated with the carboxylic acid moiety, is observed. This again confirms that at least one tryptophan is in the C form. However, in contrast to $\text{Ba}^{2+}\text{Trp}_2$, $\text{Ca}^{2+}\text{Trp}_2$ clearly displays an absorption band in the N-H stretching region (3340 cm⁻¹). The position of

this band is consistent with an antisymmetric NH_3^+ stretching mode, diagnostic for a Z tryptophan. The simultaneous presence of carboxylic acid O-H and NH_3^+ modes indicates the presence of a mixed C/Z dimer. The lowest-energy C1/Z2 and C1/Z3 mixed dimer conformations indeed confirm the presence of an antisymmetric NH_3^+ stretching mode at $\sim 3340 \text{ cm}^{-1}$. Note that this band was not observed for $\text{Ba}^{2+}\text{Trp}_2$, in spite of its more efficient photodissociation. Moreover, if this band were due to an NH_2 stretch mode, associated with the C/C structure, then it should also have been observed for all $\text{M}^{2+}\text{Trp}_2$ complexes. These observations make a strong case for the identification of a mixed C/Z dimer for $\text{Ca}^{2+}\text{Trp}_2$.

Intriguingly though, other intense NH_3^+ stretches that are predicted at lower frequency are not observed. The calculations indicate that the exact positions of these lower-frequency NH_3^+ modes are highly dependent on conformation. Specifically, the C1/Z2 predicts NH_3^+ stretches at 3090 and 3195 cm^{-1} and the marginally higher-energy structure C1/Z3 ($+2 \text{ kJ mol}^{-1}$) predicts the corresponding modes at 3110 and 3295 cm^{-1} . On the other hand, the higher-frequency NH_3^+ stretch at 3340 cm^{-1} is consistently reproduced at the same frequency for both geometries. In higher-energy conformations (not shown here), the same trend is observed, in that the position of the antisymmetric NH_3^+ stretch is unaffected by conformation, whereas the lower-frequency bands are affected. Given the floppy nature of these complexes at room temperature, it is thus conceivable that the lower-frequency NH_3^+ bands are not as well defined as the antisymmetric NH_3^+ stretch. If such structures were to interconvert at room temperature or during infrared activation, this would impede resonant absorption of multiple photons for such NH_3^+ stretching modes from OPO laser irradiation. Resonant absorption of

multiple photons may, however, be required to reach the quasi-continuum, where non-resonant absorption from CO₂ laser irradiation brings the ions over the dissociation threshold. Another contributing factor to lower IRMPD yield is likely to be the lower energy per photon, as well as lower laser power than for the corresponding antisymmetric NH₃⁺ stretch.

Despite the inability to detect multiple NH₃⁺ modes, the appearance of a band at 3340 cm⁻¹ suggests the presence of a Z configuration for one of the tryptophans, and is consistent with a mixed C/Z dimer. This does, however, not exclude the possibility of C/C dimers, which may also be present at some level. The previous FELIX study on Ca²⁺Trp₂ was also compatible with a C/Z configuration.¹¹⁵ In this case, C1/Z2 yielded a better match with the experimental spectrum than C1/Z3. No such distinction could be established in the OPO-laser range, due to an inability to detect the lower-frequency NH₃⁺ modes.

Metal Binding Effects on Z Stabilization

The size effect to favor Z-containing tryptophans for smaller cations runs counter to the trend established by Jockusch et al.^{121,125} and Bush et al.¹³⁶ for arginine bound to the alkali metal series (Li⁺–Cs⁺), and later confirmed by Armentrout for serine and methionine.^{134,139} On the other hand, IR spectroscopy results on cationized proline by Schäfer and co-workers¹⁶⁴ showed an opposite trend in the stabilization of Z for smaller alkali metals, as opposed to C for larger cations. They hypothesized that this trend should be mainly observed in aliphatic amino acids, which lack a functionalized side-chain (e.g. heteroatom N, O, S, or aromatic ring). Such functionalized side-chains offer binding partners for the metal cations, whereas the aliphatic amino acids, such as proline (glycine, alanine, valine, leucine and isoleucine), are limited to binding via their

amino N or acid O moieties. In the absence of competing side-chain binding partners, the larger polarizing effect of smaller metal cations leads to charge separation (i.e., Z structure).

In our case of tryptophan dimers, the rationale above cannot explain the effects that are observed, since tryptophan is not an aliphatic amino acid. The question thus arises what other factors are responsible. From chemical intuition, in dimer complexes steric effects are likely to play a much more pronounced role than in monomer complexes. The binding patterns considered for $M^{2+}Trp_2$ are summarized in Figure 3-2. In C1/C1, the lowest-energy C-only geometry, the metal engages in electrostatic bonding to the carboxylic acid O, amino N, and the indole side-chain π -cloud on both tryptophans. This results in a large degree of steric crowding around the cation, and is hence favored for larger cations, such as Sr^{2+} and Ba^{2+} . Conversely, in the lowest-energy mixed dimer conformation for the smaller cations, C1/Z2, steric effects are minimized. Instead, Z2 adopts a more extended form, where the carboxylate is tightly solvated, whereas the indole side-chain is not involved in binding to the metal cation. The more compact mixed dimer conformation, C1/Z3, where the cation binds to both indole side-chains, is probably less favored in smaller alkaline earth complexes, due to steric crowding, as in fact confirmed by the computations. It is not clear yet why C1/Z3 would be disfavored relative to C1/C1 for larger cations. Single-point MP2 calculations for C1/Z3 and C1/C1 (not shown) did not show considerable differences in stability between both geometries, indicating that dispersion interactions do not explain this observation. In summary, the mixed dimer extended structure, C1/Z2, is consistent with

solvating a smaller cation, whereas the more compact C-only conformation, C1/C1, requires a larger cation, to minimize steric repulsion.

Conclusions

It is shown that IRMPD spectroscopy of the N-H and O-H stretching regions serve as a useful ‘fingerprint’ region in identifying Z or C structure in the gas phase. The structural assignment is based on diagnostic bands associated with the carboxylic acid OH stretch (C) and the NH_3^+ asymmetric stretching mode (Z). A clear example of a Z structure is observed for monomeric Ba^{2+}Trp , by virtue of a lack of photodissociation between 3525–3625 cm^{-1} (O-H) and the presence of a doublet at 3290 cm^{-1} and 3320 cm^{-1} (N-H). The simple distinction of these two wavelength regions is then implemented on tryptophan dimer complexes for the alkaline earth series. An unexpected trend is seen, in that the C/Z mixed structure is favored with decreasing metal size, as opposed to C/C for larger cations (Sr^{2+} and Ba^{2+}). This trend is in sharp contrast to other studies on alkali metal-chelated amino acids. These results point to the complex interplay of forces that determine zwitterion stabilization in the gas phase, showing that trends are not always easy to generalize. In this case, it is hypothesized that steric effects account for differences in stability between C/C and C/Z isomers. A more extended C/Z structure, not involving the Z indole side-chain, is capable of effectively solvating smaller alkaline earth cations. Conversely, the more tightly bound C/C structure involves both indole side-chains, and hence presents steric crowding problems for smaller cations. For larger cation complexes, these steric effects are less of a concern.

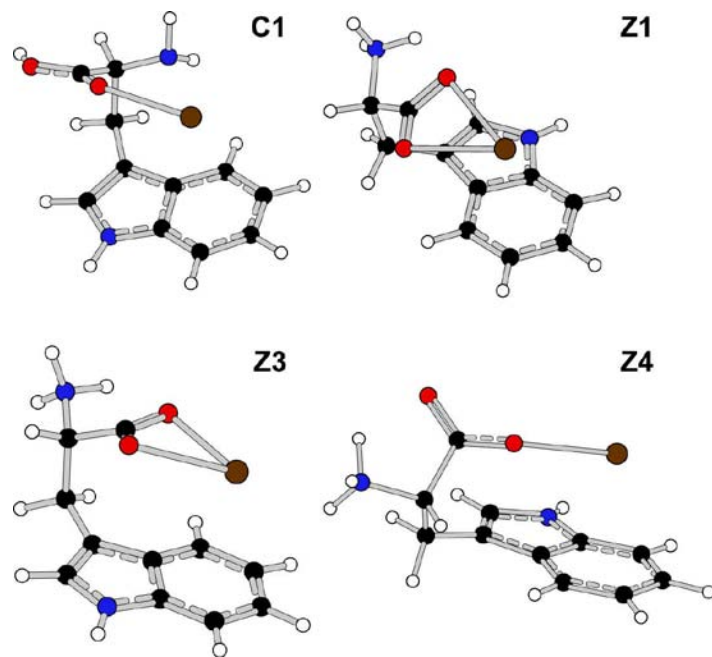


Figure 3-1. Four of the lowest-energy calculated structures for the Ba^{2+}Trp complex. C1 denotes a charge solvated (C) configuration and Z1, Z3, and Z4 denote the zwitterionic (Z) configuration. The numbers represent different conformers in each configuration. [Taken with permission from Elsevier B. V. Mino Jr., W. K.; Szccepanski, J.; Pearson, W. L.; Powell, D. H.; Dunbar, R. C.; Eyler, J. R.; Polfer, N. C. Vibrational Signatures of Zwitterionic and Charge-Solvated Structures for Alkaline Earth-Tryptophan Dimer Complexes in the Gas Phase. *Int. J. Mass Spectrom.* (Volume 297, Pages 131-138)]

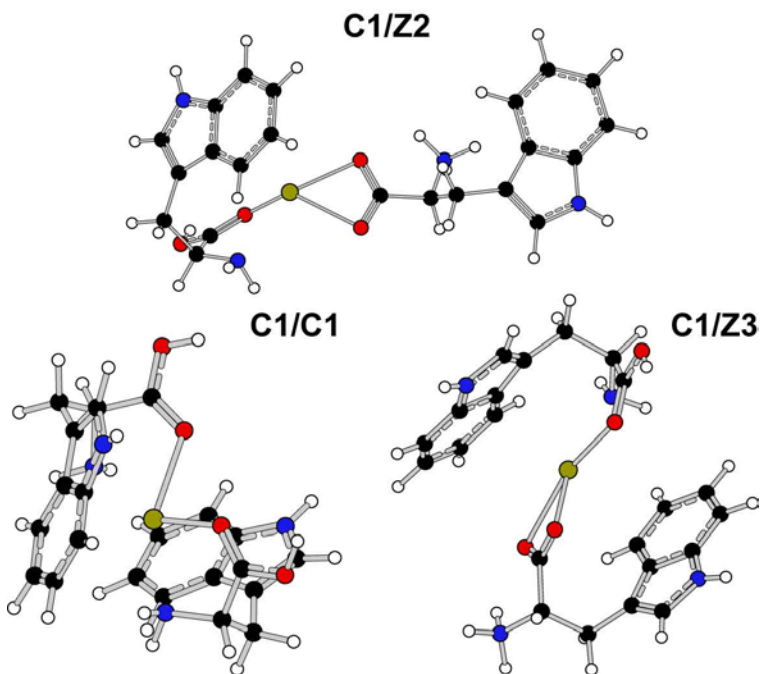


Figure 3-2. Three lowest-energy calculated structures for the $M^{2+}\text{Trp}_2$ complex, where M is Mg, Ca, Sr, and Ba. C1 denotes a charge-solvated configuration and Z2 and Z3 denote the zwitterionic (Z) configuration. The numbers represent different conformers in each configuration. [Taken with permission from Elsevier B. V. Mino Jr., W. K.; Szczechanski, J.; Pearson, W. L.; Powell, D. H.; Dunbar, R. C.; Eyler, J. R.; Polfer, N. C. Vibrational Signatures of Zwitterionic and Charge-Solvated Structures for Alkaline Earth-Tryptophan Dimer Complexes in the Gas Phase. *Int. J. Mass Spectrom.* (Volume 297, Pages 131-138)]

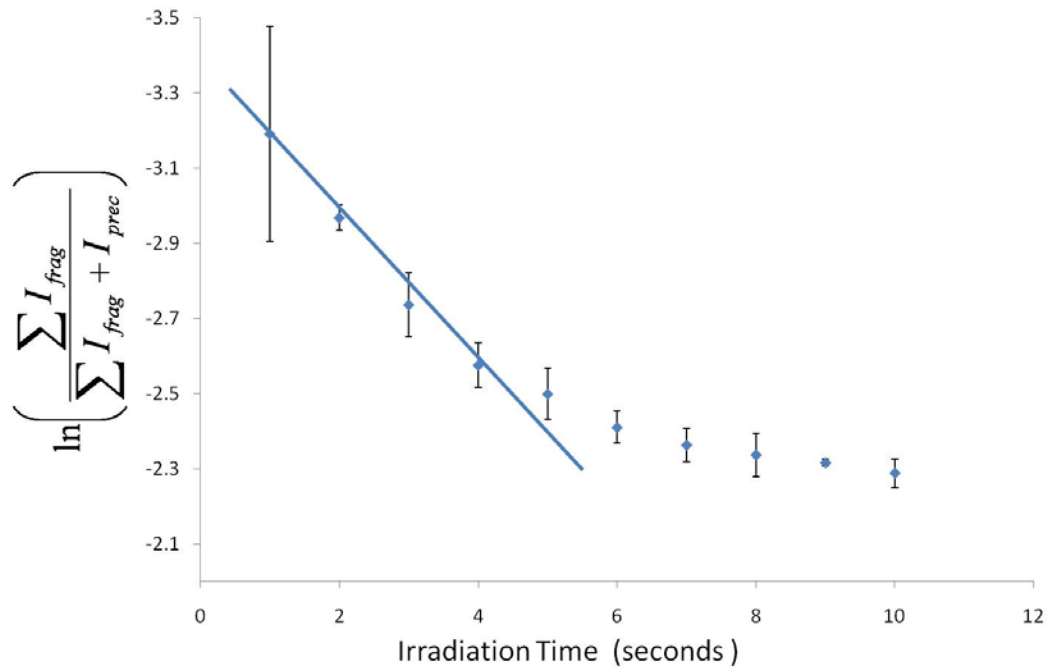


Figure 3-3. Fragmentation yield dependence on OPO irradiation time for the Ba^{2+}Trp monomer irradiated at 3328 cm^{-1} .

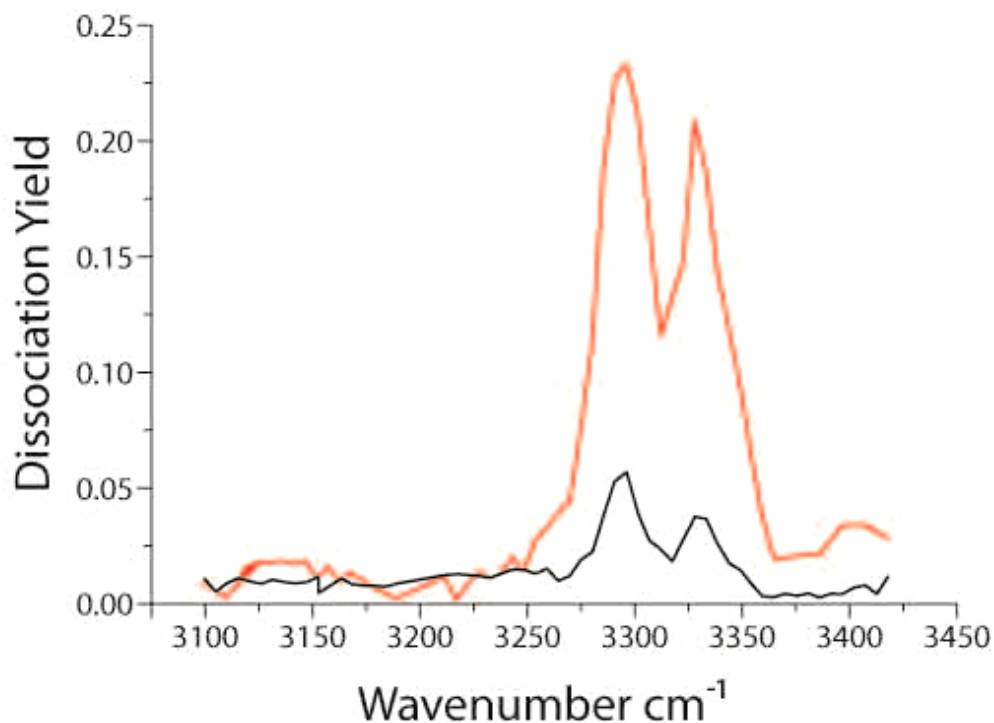


Figure 3-4. Comparison of the dissociation yield of Ba^{2+}Trp when irradiating for 10 s with the OPO laser alone (black) vs. sequential irradiation by the OPO for 5 s and CO_2 lasers for 500 ms (red).

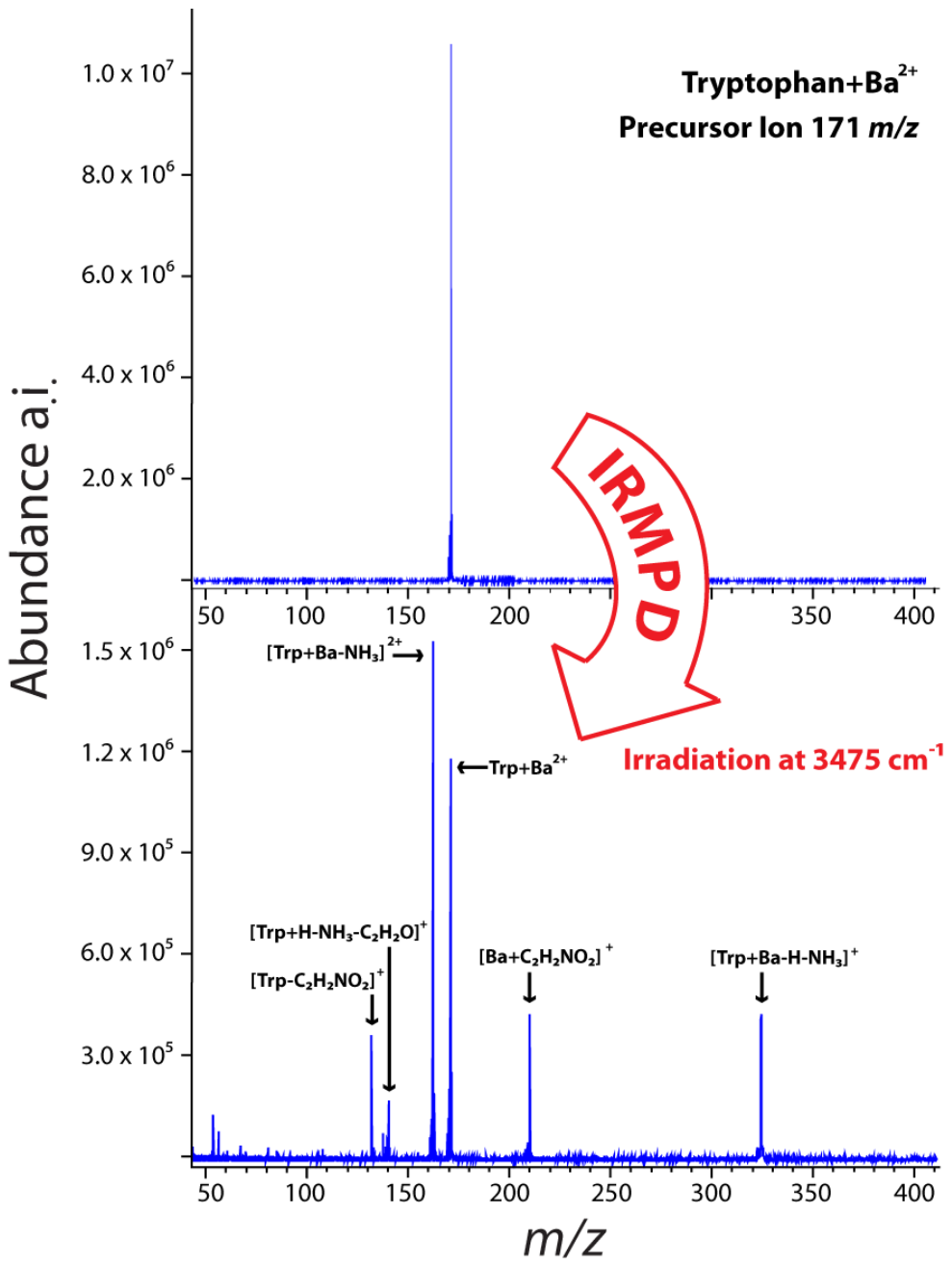


Figure 3-5. Mass spectra of Ba^{2+}Trp after isolation (top) and after MS/MS (bottom). The mass selected ion was irradiated for 10 seconds at 3475 cm^{-1} .

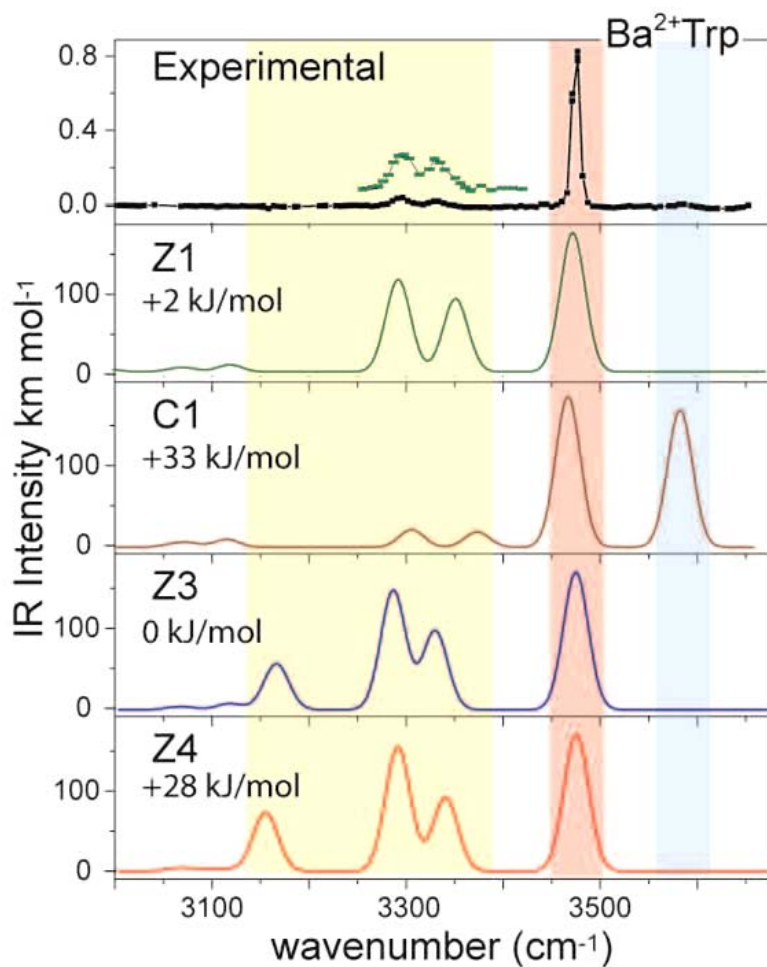


Figure 3-6. IRMPD spectrum of Ba^{2+}Trp ($3000\text{-}3700 \text{ cm}^{-1}$) with calculated vibrational spectra for Z (Z1, Z3, and Z4 conformations) and C (C1 conformation). The calculated geometries are displayed in Figure 3.1. Characteristic wavenumber regions of the spectrum are highlighted in yellow, red and blue to indicate the NH_3^+ , indole N-H, and carboxylic acid O-H stretching modes, respectively. The zero point corrected energies of each structure are shown for comparison. [Taken with permission from Elsevier B. V. Mino Jr., W. K.; Szczechanski, J.; Pearson, W. L.; Powell, D. H.; Dunbar, R. C.; Eyler, J. R.; Polfer, N. C. Vibrational Signatures of Zwitterionic and Charge-Solvated Structures for Alkaline Earth-Tryptophan Dimer Complexes in the Gas Phase. *Int. J. Mass Spectrom.* (Volume 297, Pages 131-138)]

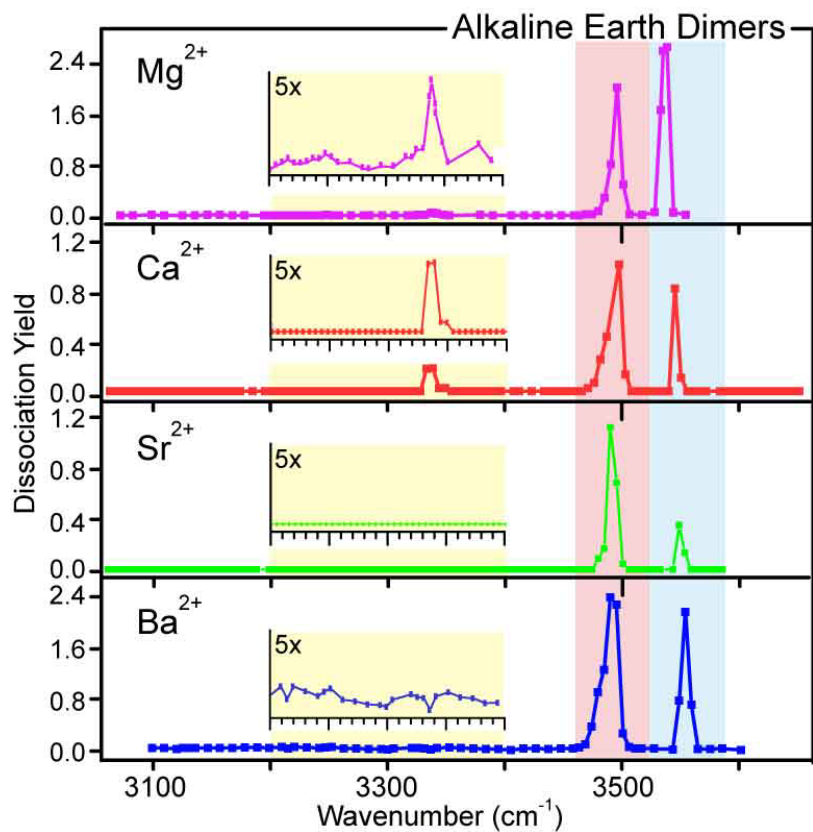


Figure 3-7. IRMPD spectra of the $M^{2+}\text{Trp}_2$ alkaline earth series in N-H and O-H stretching regions. Characteristic wavelength regions associated with NH_3^+ , indole N-H, and O-H stretching modes are highlighted in yellow, red and blue, respectively. The inset shows a 5 times magnification of the NH_3^+ stretching region. [Taken with permission from Elsevier B. V. Mino Jr., W. K.; Szczepanski, J.; Pearson, W. L.; Powell, D. H.; Dunbar, R. C.; Eyler, J. R.; Polfer, N. C. Vibrational Signatures of Zwitterionic and Charge-Solvated Structures for Alkaline Earth-Tryptophan Dimer Complexes in the Gas Phase. *Int. J. Mass Spectrom.* (Volume 297, Pages 131-138)]

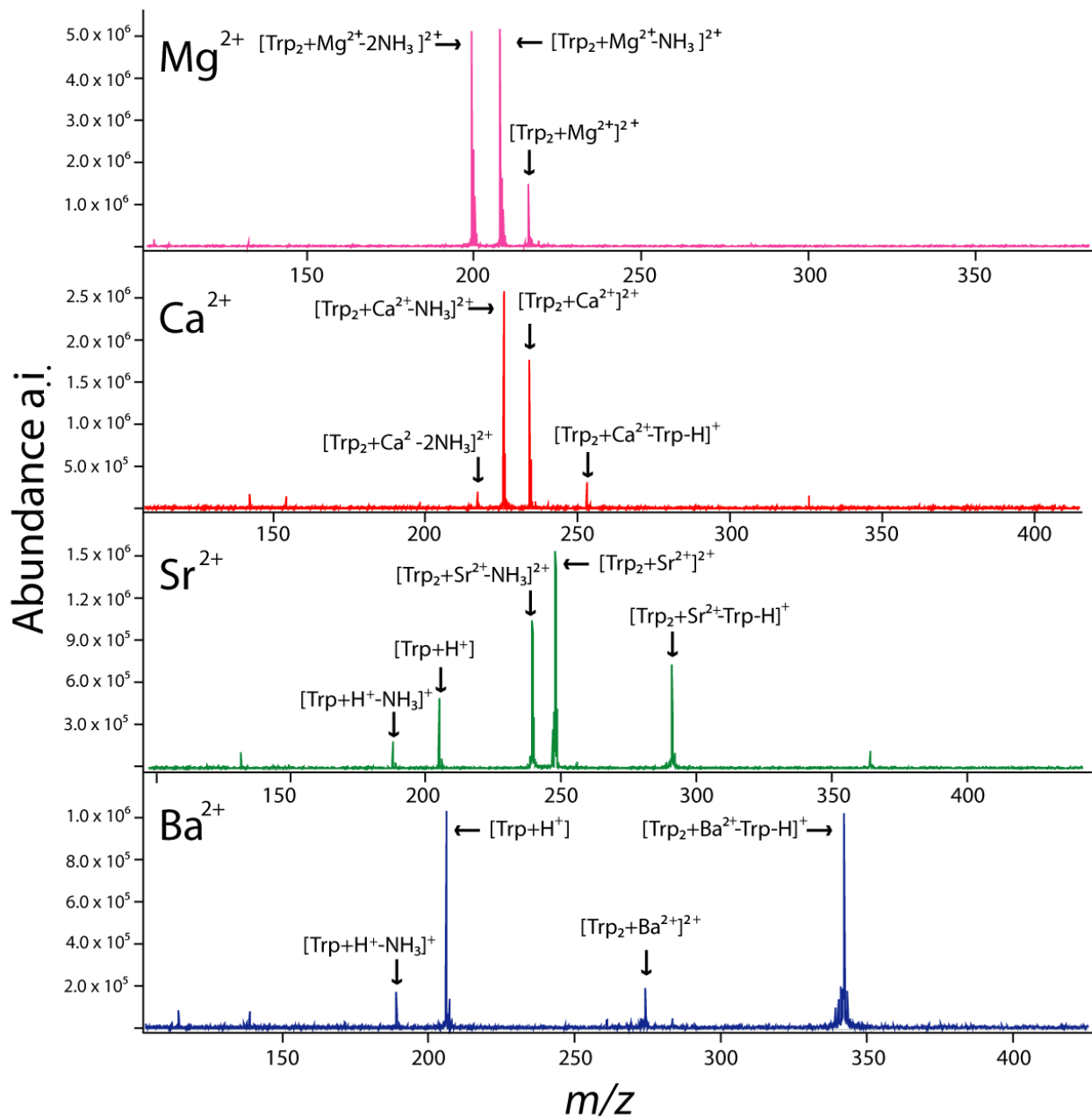


Figure 3-8. Tandem mass spectra of the $M^{2+}Trp_2$ where $M=Mg$, Ca , Sr , and Ba . Each mass spectrum represents the most intense fragmentation recorded for each complexes IRMPD spectrum. The Mg^{2+} spectrum was recorded at 3540 cm^{-1} , $Ca^{2+} + Trp_2$ was recorded at 3495 cm^{-1} . $Sr^{2+} + Trp_2$ and $Ba^{2+} + Trp_2$ were recorded at 3490 cm^{-1} .

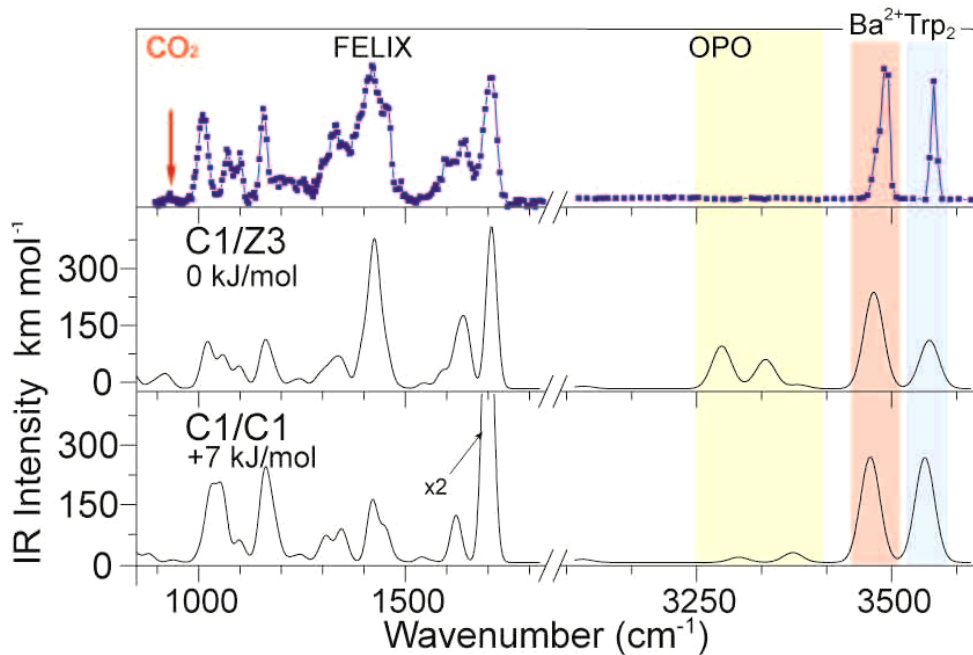


Figure 3-9. IRMPD spectra of $\text{Ba}^{2+}\text{Trp}_2$ with calculated vibrational spectra for the two lowest-energy conformers. The calculated geometries are displayed in Figure 3.2. Characteristic wavelength regions associated with NH_3^+ , indole N-H, and O-H stretching modes are highlighted in yellow, red and blue, respectively. The zero point corrected energies of each structure are shown for comparison. The CO_2 laser wavelength ($10.6 \mu\text{m}$) is indicated by a red arrow. [Taken with permission from Elsevier B. V. Mino Jr., W. K.; Szczepanski, J.; Pearson, W. L.; Powell, D. H.; Dunbar, R. C.; Eyler, J. R.; Polfer, N. C. Vibrational Signatures of Zwitterionic and Charge-Solvated Structures for Alkaline Earth-Tryptophan Dimer Complexes in the Gas Phase. *Int. J. Mass Spectrom.* (Volume 297, Pages 131-138)]

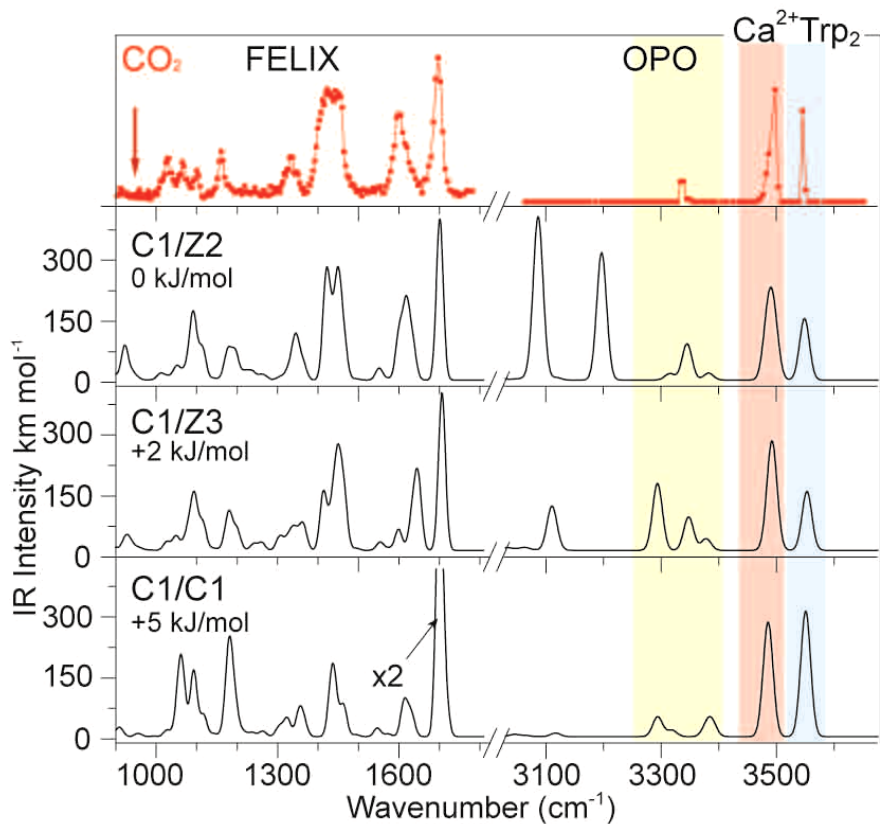


Figure 3-10. IRMPD spectra of $\text{Ca}^{2+}\text{Trp}_2$ with calculated vibrational spectra for the three lowest-energy conformers. The calculated geometries are displayed in Figure 3.2. Characteristic wavelength regions associated with NH_3^+ , indole N-H, and O-H stretching modes are highlighted in yellow, red and blue, respectively. The zero point corrected energies of each structure are shown for comparison. The CO_2 laser wavelength ($10.6 \mu\text{m}$) is indicated by a red arrow. [Taken with permission from Elsevier B. V. Mino Jr., W. K.; Szczechanski, J.; Pearson, W. L.; Powell, D. H.; Dunbar, R. C.; Eyler, J. R.; Polfer, N. C. Vibrational Signatures of Zwitterionic and Charge-Solvated Structures for Alkaline Earth-Tryptophan Dimer Complexes in the Gas Phase. *Int. J. Mass Spectrom.* (Volume 297, Pages 131-138)]

CHAPTER 4

VIBRATIONAL SIGNATURE OF ZWITTERIONIC AND CHARGE-SOLVATED STRUCTURES FOR ALKALINE EARTH METHIONINE DIMER COMPLEXES IN THE GAS PHASE

Introduction

Metal ions are abundant in biological systems and metal complexes play important roles in biological systems.¹⁶⁵⁻¹⁶⁹ For example, the presence of Mg²⁺ has been shown to increase the enzyme activity of methionine aminopeptidase, and Ca²⁺-methionine interactions have been reported to affect the activation of cyclic nucleotide phosphodiesterase.¹⁷⁰ Additionally, methionine synthetase activity was shown to be activated and inhibited in the presence of alkaline earth metals at various concentrations.¹⁷¹ Thus, studying amino acid-metal complexed systems can improve the understanding of fundamental interactions between metals and biological molecules.

Although solution-phase experiments, as those mentioned above, investigate systems under biologically relevant conditions, interactions between solvent and analytes can alter fundamental metal-complex interactions. To overcome this limitation, gas-phase experiments are used to investigate biological systems without the presence of solution effects. Mass spectrometry experiments are well suited to this task, as metal-ligand complexes can be conveniently made by electrospray ionization. Recently, alkali-metal cation interactions with methionine have been studied with guided ion beam mass spectrometry¹⁴² and infrared multiple photon dissociation (IRMPD) spectroscopy.¹³⁹

The implementation of (freely) tunable free electron lasers (FELs) and optical parametric oscillating (OPO) lasers coupled with a mass spectrometer has sparked an interest in IRMPD spectroscopy.^{172,52,173} IRMPD spectroscopy has been employed to

address a number of structural questions in biological molecules pertaining to peptide fragmentation chemistry,^{174,175} differentiation of carbohydrate isomers,¹⁵⁵ and distinguishing charge solvated (C) from zwitterionic (Z) amino acid-metal complexes.^{139,125,136,134,140,115,122-124,126-129,120,176,130-133,135,137,138,141,177,178} In the gas phase, devoid of polar solvent molecules, the amino acid adopts the C form. However, complexation with a metal cation can also induce transition from the C to the Z form, where the carboxylic acid proton is transferred to the amino group (i.e., H₂N-CHR-COOH → H₃N⁺-CHR-CO₂⁻). In the previous chapter, investigation of the trends in stabilizing Z vs. C structures of dimeric tryptophan complexed with the divalent alkaline earth metal series, using an OPO laser coupled with a Fourier transform ion cyclotron resonance mass spectrometer were reported.¹⁷⁹ Results indicated that the structure of the Trp-metal complex changed as metal size increased. Whereas Mg²⁺ and Ca²⁺ Trp-dimers favored a mixed Z/C structure, Sr²⁺ and Ba²⁺ favored a C/C structure. These results were in contrast with studies by Jockusch,¹²¹ where larger metals were proposed to solvate the carboxylate group more effectively, thereby favoring the Z form, as confirmed later by IRMPD spectroscopy.^{139,125,136,134} Since the chemical complexity of dimer systems is increased over corresponding monomer systems, other chemical effects cause an opposite trend in structural conformation. It was hence proposed that for tryptophan dimers, the bulky indole side chain induces a steric effect to counter expected trends.

In the present study, steric effects on Z or C stabilization were investigated with methionine alkaline earth series complexes. Methionine is similar to tryptophan in that they are both non-polar amino acids, but they differ significantly by the side-chain

chemistry. The tryptophan hydrophobicity is due to the aromatic indole side chain compared to the sulfur-containing hydrocarbon side chain of methionine. Methionine has more degrees of freedom compared to tryptophan, the π -bonding system versus the sulfur containing hydrocarbon chain, and thus provides a suitable candidate for comparison with the tryptophan results.

Experimental

Materials

Standard solutions of Mg(NO₃)₂, Ca(NO₃)₂, Sr(NO₃)₂, Ba(NO₃)₂, and L-Methionine (Acros Organics) were prepared in HPLC-grade water (Fisher Scientific) and diluted to a concentration of 10⁻² M. All samples were mixed at a 1:1 ratio to yield a final concentration of 10⁻³ M in 70:30 methanol (Fisher Scientific)/water.

Mass Spectrometry and Photodissociation

Photodissociation experiments were performed with a 4.7 Fourier transform ion cyclotron resonance (FT-ICR) mass spectrometer (Bruker Daltonics, Billerica, MA), a continuous wave (cw) periodically polled lithium niobate–optical parametric oscillating (OPO) laser (LINOS Photonics, Germany) as well as a cw-CO₂ laser (SYNRAD J48-5W Mukilteo, WA), and are described in Chapter 3. Briefly, ions were generated by electrospray ionization, accumulated in a hexapole, and guided into the ICR cell for photodissociation experiments. The tunable radiation was scanned by the OPO laser over the 3000 cm⁻¹ to 3700 cm⁻¹ range, in 5 cm⁻¹ steps. Ions were irradiated with the OPO laser for 5 s followed by a 500 ms pulse of the fixed wavelength CO₂ laser irradiation at 10.6 μ m. The continuous power of the OPO ranged between 30–50 mW and the CO₂ laser was operated at 2 W. The photodissociation yield was calculated with the equation, $yield = -\ln[1 - \{\sum Int_photofragments / (\sum Int_photofragments)$

+Int_precursor)}]. Furthermore, the yield was power corrected and plotted as a function of the OPO idler wavenumber (cm^{-1}) to generate the IRMPD spectra.

Calculations

Starting structures were generated by probing a wide range of metal-solvating geometries, such as binding with lone pairs on nitrogen, sulfur, and the two carboxylic oxygen's for the methionine Mg^{2+} monomer. The monomer calculations served as a basis for identifying the lowest-energy binding motifs for the methionine system. Nine distinct lowest-energy motifs from this search are shown in Figure 4-1. Initial structures were generated in the GABEDIT software¹⁸⁰, by drawing starting structures and optimizing them with molecular dynamic simulations using the quasi-Newtonian gradient optimization algorithm and the AMBER model to calculate energy, under the default parameters (maximum number of iterations=10,000; $\epsilon=10^{-4}$) in the GABEDIT software package. These starting structures were further optimized with the Gaussian software package¹⁵⁸ at the B3LYP level and a basis set of 6-31G*. The detailed computational strategy is summarized below.

This systematic approach to performing a conformational search minimizes computational time. Importantly, Mg^{2+} is parameterized for molecular dynamic simulations. Thus, a fast conformational search can be performed prior to DFT. The geometries that were found for Mg^{2+}Met monomer and $\text{Mg}^{2+}\text{Met}_2$ dimer were then also considered for the larger alkaline earth metal cations at the DFT level.

Given the non-covalent chelation of the metal cation, there are in principle a very large number of binding patterns that have to be considered. The initial geometries were built by hand in the GABEDIT software package using chemical intuition. The structures were then optimized by molecular mechanics, while restraining the ionic bond distance

between the atoms and the metal cation. Although this approach works well for the monomer systems, for the dimer complexes this would result in too many possibilities.

Instead, the monomer binding motifs were combined in the dimer complexes, in order to consider a wide range of geometries. Molecular mechanics optimization was performed on some of the dimer systems prior to DFT optimization. However, many of the dimer molecular mechanics calculations resulted in poor optimization (i.e., complete rearrangement of all the atoms to an unrealistic geometry). Furthermore, the molecular mechanic optimizations prior to DFT calculations did not have a noticeable effect on computational time.

In detail, this was done by copying and pasting two Gaussian Cartesian coordinate files into the same file and reopening that file in the GABEDIT software package. Then, by using the metal as a reference point the two structures were brought together to build the dimer structure. Note that the extra metal center was deleted to make the final input structure. The Mg^{2+} metal center was replaced by the other metals, Ca^{2+} , Sr^{2+} , and Ba^{2+} . For the candidate dimer complexes, geometry optimization was directly performed at the B3LYP/6-31G* level of theory.

In addition to replacing the metal center, bond distances between the metal and heteroatom on methionine needed to be adapted, as the metals all vary in size. The average bond distances to the complexed metal can be seen in Table 4-1. As expected, the larger metals have longer bond distances compared to the smaller metals. The bond distances ranged from 2.05 Å to 2.68 Å and 2.43 Å to 2.91 Å for the oxygen-metal and nitrogen-metal distances, respectively. An example of how the measurement was done is shown in Figure 4-2. Briefly, the GABEDIT software package contains a bond

measurement tool. By selecting the atoms that require measurement, GABEDIT returns the bond distances of each atom relative to another. Within the program, up to 5 atoms can be selected and measured at once.

To perform optimization and frequency calculations on all four alkaline earth metal complexes, the Stuttgart-Dresden (SDD) relativistic core potential was used for the larger metals, Sr^{2+} and Ba^{2+} , since these are not parameterized in the 6-31G* basis set. The calculated vibrational frequencies were scaled¹⁸¹ by 0.9613 and stick spectra were broadened with a Gaussian function to 15 cm^{-1} FWHM (full width at half-maximum). The convoluted spectra were then normalized to integral band intensities in km mol^{-1} for more convenient comparison of vibrational intensities.

Results and Discussion

Ba²⁺ Methionine Monomer Complex

To make direct comparison to the tryptophan results from Chapter 3, the Ba²⁺ methionine complex was measured via IRMPD spectroscopy. Figure 4-3 is the IRMPD spectrum of Ba²⁺Met recorded over the 3200 cm^{-1} to 3650 cm^{-1} range to investigate the presence of a C or Z configuration. The lack of fragmentation in the 3500 cm^{-1} to 3650 cm^{-1} range is indicative of a Z conformation. Furthermore, as expected for NH_3^+ modes, a broad doublet can be seen in the spectrum between 3250 cm^{-1} and 3350 cm^{-1} . In comparison to the Ba²⁺Trp complex, the band at 3500 cm^{-1} is missing; this is expected as the methionine complex does not contain an indole N-H. Furthermore, the doublet feature appears at the same frequencies for both spectra. This is further confirmation that the Ba²⁺Met complex is in the Z conformer and illustrates that calculations are not necessary for identification of gas-phase structures, as long as an experimental

database is built for comparison. The use of the Ba²⁺Trp specifically as a “fingerprint” for a Z structure is thus supported.

Alkaline Earth Methionine Dimer Series

The IRMPD spectra recorded over the 3200–3700 cm⁻¹ range for a series of dimeric M²⁺Met₂ complexes (where M= Mg, Ca, Sr, and Ba) are compared in Figure 4-4. The spectrum is color-coded to reflect where the diagnostic O-H (blue) and NH₃⁺ (yellow) vibrations are expected. The presence of bands in these regions indicate the presence of a C structure, based on a carboxylic acid O-H stretch, and a Z structure, based on the antisymmetric stretch mode of the NH₃⁺ group. For the alkaline earth series in Figure 4-3, there are considerable differences. While the smaller cations Mg²⁺ and Ca²⁺ show abundant photodissociation in the O-H stretch region, the larger cations Sr²⁺ and Ba²⁺ do not. On the other hand, Ca²⁺, Sr²⁺ and Ba²⁺ all display a prominent NH₃⁺ stretching band; however, much weaker features are observed in the Mg²⁺ spectrum. These results strongly suggest that there is a size effect, in that Mg²⁺ favors a purely charge-solvated configuration, C/C, whereas Sr²⁺ and Ba²⁺ both adopt a zwitterion-only configuration, Z/Z. The intermediate case of Ca²⁺ confirms evidence for both C and Z, indicating that this corresponds to a mixed C/Z dimer.

In terms of structural identification between C and Z, the O-H stretching region is unambiguous. The NH₃⁺ region, however, overlaps with other N-H stretching modes. The symmetric and antisymmetric stretches of the unprotonated NH₂ moiety in a C structure are also expected in this region and the results for Mg²⁺ are certainly consistent with this hypothesis. Due to the abundant IRMPD yield for Mg²⁺, these modes are visible. For Ca²⁺ and Sr²⁺, the overall IRMPD yield is much reduced, yet the intensities of those bands compared to the carboxylic acid O-H are much increased.

This intensity enhancement for an N-H stretch band is consistent with a switch from NH_2 to NH_3^+ , as the latter is a much brighter mode.

In addition to the chemically specific information based on vibrational analysis, IRMPD spectroscopy also yields information on fragmentation pathways. Example mass spectra from irradiation with the OPO laser are shown in Figure 4-5 for all four $\text{M}^{2+}+\text{Met}_2$ complexes. Each mass spectrum corresponds to the most intense photo fragmentation spectrum: $\text{Mg}^{2+}\text{Met}_2$ at 3525 cm^{-1} , $\text{Ca}^{2+}+\text{Met}_2$ at 3535 cm^{-1} , $\text{Sr}^{2+}+\text{Met}_2$ and $\text{Ba}^{2+}+\text{Met}_2$ at 3345 cm^{-1} .

The fragmentation pathways for the four complexes differed significantly between two groups. The smaller cations, Mg^{2+} and Ca^{2+} , resulted in a neutral loss of NH_3 , or even two NH_3 for Mg^{2+} . Conversely, for the larger metal cations, Sr^{2+} and Ba^{2+} , the exclusive dissociation pathway is by charge separation to yield protonated methionine, $[\text{Met}+\text{H}]^+$, and de-protonated $[\text{Met}+\text{Me}^{2+}-\text{H}]^+$. The cleavage of a covalent bond to result in NH_3 loss suggests that there is a polarization effect for the smaller cations that destabilizes the C-N bond on the alpha carbon of the amino acid.

Although the experimental trends seem pervasive, a comparison with quantum-chemical calculations is shown to confirm these conclusions. The theoretical structures can be grouped into three different general structures: purely charge-solvated (C/C), mixed charge-solvated and zwitterionic, (C/Z) and purely zwitterionic (Z/Z) structures.

Mg²⁺ Methionine Dimer Complex

The experimental IRMPD spectrum compared with four calculated spectra is shown for the $\text{Mg}^{2+}\text{Met}_2$ complex in Figure 4-6. The dimer structures are labeled as their corresponding starting monomer structures as illustrated in Figure 4-1. The location of the theoretical O-H vibrational band (blue) is slightly red shifted from that of the

experimental peak; however, the band position remains consistent between calculated conformers and is likely due to the anharmonicity of the carboxylic acid O-H stretch, which theory does not predict well. The O-H vibrational mode indicates that at least one of the monomers is in the C state, thus eliminating a complete Z/Z structure. The NH₃ region (yellow) can be used to differentiate between a purely C/C or a mixed C/Z structure. The major indication of a Z structure is intense fragmentation in the yellow, NH₃⁺ region. The purely charged solvated structure predicts weak absorption in this region compared to more intense absorption predicted for the mixed structure (See for example Figure 4-7 (top)). Although fragmentation is expected for the NH₂ bands, it is possible that these modes are too weak, and hence cannot be detected in this experiment. The region between 3300 cm⁻¹ and 3375 cm⁻¹ displays some minor fragmentation; however, no IRMPD band is discernable. These weaker experimental modes are an indication of purely C/C structure. Furthermore, the lowest zero-point corrected energy conformers for the Mg²⁺Met₂ complex were all purely C/C structures.

Ca²⁺ Methionine Dimer Complex

The experimental IRMPD spectrum compared with three theoretical spectra is shown for the Ca²⁺Met₂ complex in Figure 4-7. The three calculated spectra shown are the lowest zero point-corrected energy structures for the mixed C/Z and C/C structures. The position of the theoretical O-H stretch is in good agreement with the experimental spectra (slightly red shifted) and the band position is independent of mixed C/Z or purely C/C structure. Thus, the O-H stretch is indicative of either a mixed C/S structure or a pure C/C structure, but cannot confirm exact structural assignment. The calculated structures, similar the calculations for the Mg²⁺ complex, display weaker absorption for the NH₂ modes compared to the NH₃⁺ modes in the mixed C/Z structure. The peak from

the IRMPD spectrum at 3350 cm^{-1} matches well with the band predicted by theory for the lowest energy structure. However, the band that results from IRMPD appears to have two peaks that are not base line resolved. Although this is not predicted by theory, the general features are in good agreement and confirm a mixed C/Z structure. Furthermore, the mixed C/Z structure was predicted to be the lowest energy conformer for the Ca^{2+} complex.

Ba²⁺ Methionine Dimer Complex

The experimental IRMPD spectrum compared with three calculated spectra is shown for the $\text{Ba}^{2+}\text{Met}_2$ complex in Figure 4-8. The lack of O-H stretching (blue) in the experimental spectrum, even without calculations, is indicative of a purely zwitterionic, Z/Z structure. However, it is useful to compare with calculated spectra to make a structural assignment. The $\text{Ba}^{2+}\text{Met}_2$ experimental spectrum does not correlate well with the two lowest energy calculated pure Z/Z structures. Furthermore, the lowest energy structure, Z1/Z1 has a stronger mode close to the observed experimental peak, but the experimental spectrum does not resolve any other peaks. Referring to Figure 4-4, the Ca^{2+} and Sr^{2+} experimental spectra appear to have two peaks, although they are not baseline resolved, it is possible that the mode experimentally detected is due to an overlap of the two NH_3^+ stretching modes, which are not resolvable by IRMPD spectroscopy. Despite an inability to make exact structural assignments, the lack of O-H stretching is a clear indication of a Z/Z structure.

Comparison of Methionine and Tryptophan

The experimental data for the $\text{M}^{2+}\text{Met}_2$, where $\text{M} = \text{Mg}, \text{Ca}, \text{Sr}$, and Ba , suggests a trend of stabilizing the Z/Z structure as the metal size increases. The trend observed for this system is opposite to the trend reported in Chapter 3, where the $\text{M}^{2+}\text{Trp}_2$ favored

the purely C/C structure as the metal size increased. These two systems naturally differ by their amino acid side chains. The side chain for the tryptophan system is a pi bonded ring system with an indole N-H, where the methionine side chain is a simple carbon chain with a sulfur group before the last methyl group. One main difference is that the methionine systems have much less steric hindrance compared to the tryptophan systems. For the smaller metal systems, this constrains the tryptophan, whereas the methionine systems have more degrees of freedom, allowing the complex to explore conformations to stabilize the charge on the metal.

Another interesting observation is the dissociation pathways for both of these systems. The dissociation pathways are tabulated in Table 4-2 and illustrated in Figure 4-9. The general trends of dissociation are identical for the methionine and tryptophan systems. This is interesting because the dissociation trends are identical, yet their structures predicted by IRMPD spectroscopy show opposite trends. This demonstrates that the structure of an ion cannot be predicted based on dissociation pathways alone. For example, a neutral loss of NH₃ could indicate a purely zwitterionic structure, because a charge solvated structure would require a mobile proton to lose an NH₃. However, the purely charge-solvated Ba²⁺Trp₂ results in only charge separation loss of a monomer (-TrpH⁺), whereas the purely charge-solvated Mg²⁺Met₂ results in purely NH₃ loss. This shows that dissociation pathways are not necessarily related to the ground state structure.

A cartoon illustrating the energy barriers in the dissociation chemistry of these complexes is shown in Figure 4-10. The figure shows that there are three possible potential wells for the three types of structures, C/C, C/Z, or Z/Z, connected by lower-

energy barriers. The two possible dissociation pathways via the loss of a protonated methionine or a neutral loss of NH₃ are much higher in energy. The depth of the well indicates the stability of that conformer for each complex. For example, the C/C potential well is the deepest for the Mg²⁺Met complex, whereas the Z/Z potential well is the deepest for the Ba²⁺Met complex. Furthermore, the dissociation barriers also change between complexes. As the metal ion size increases, the relative height of the energy barrier for the protonated methionine loss is lowered. The Ba²⁺Met dimer is the only complex where the protonated methionine loss is completely favored over the neutral loss of NH₃.

Conclusions

It is shown that IRMPD spectroscopy of the N-H and O-H stretching regions can identify trends of zwitterionic stabilization in the gas phase. The structural assignment is based on diagnostic bands associated with the carboxylic acid O-H stretch and the NH₃⁺ asymmetric stretching mode. The simple distinction of these two wavelength regions is then implemented on methionine dimer complexes for the alkaline earth series. A trend of favoring the charge-solvated structure with decreasing metal size, as opposed to purely zwitterionic structure for larger cations (Sr²⁺ and Ba²⁺) was seen for the M²⁺Met₂ complexes. This trend is in sharp contrast to the studies conducted in Chapter 3. These results point to the complex interplay of forces that determine zwitterion stabilization in the gas phase, showing that trends are not always easy to generalize. In this case, it is hypothesized that the degrees of freedom in the methionine system compared to the steric effects in the tryptophan system account for the differences in the trends observed. Furthermore, it is shown that simple assignments based on fragmentation pathways are a poor indication in terms of identifying

zwitterionic or charge-solvated structures. This illustrates that IRMPD spectroscopy is a much more direct probe of gas-phase structure, as the structure prior to activation is elucidated.

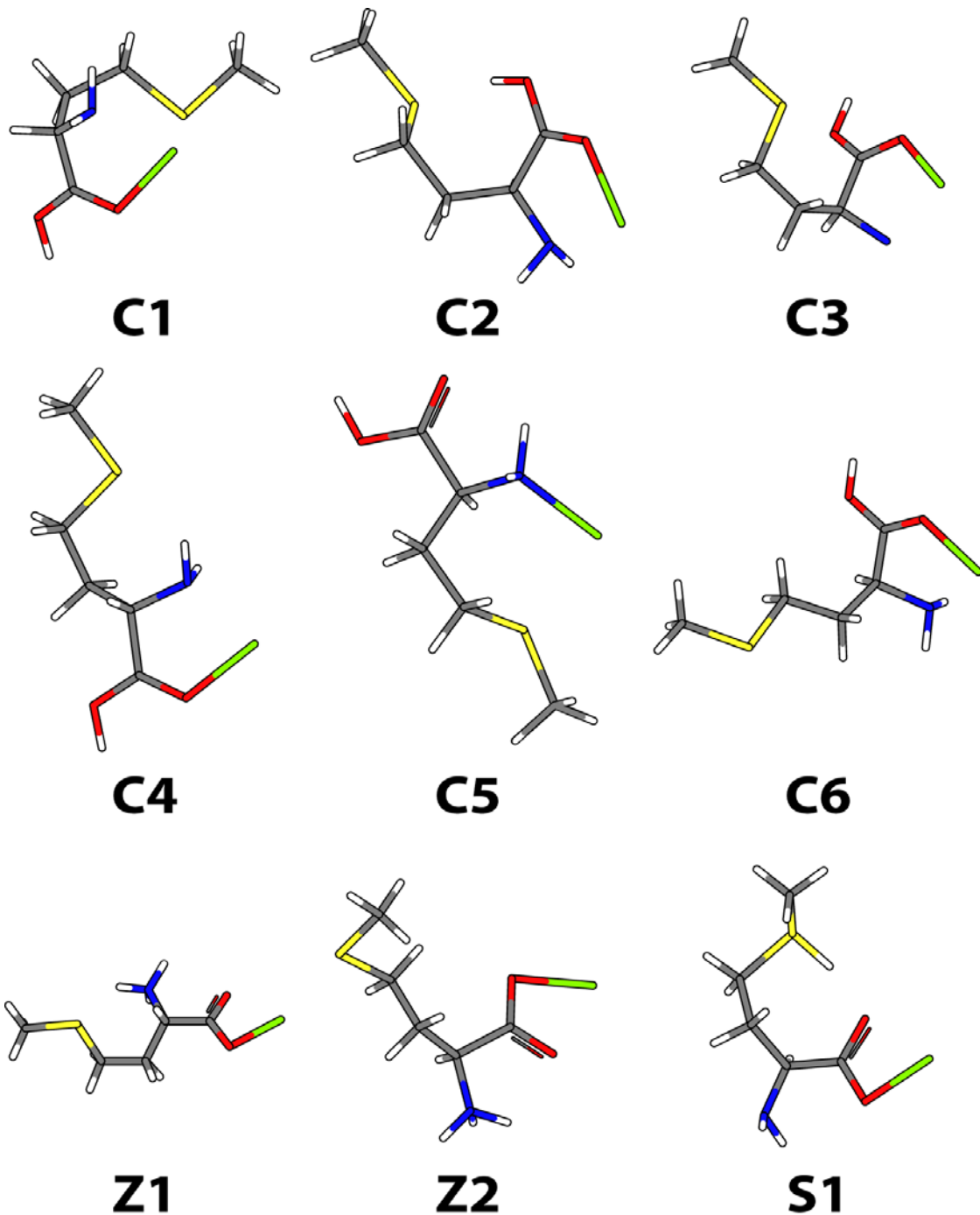


Figure 4-1. Nine of the lowest-energy calculated structures for the M^{2+} -Met monomeric complex. C1-C6 denotes a charge solvated (C) conformers and Z1 and Z2 denote zwitterionic (Z) geometries. Some monomer structures converged by moving the hydrogen to the sulfur group, and these structures are denoted as S.

Table 4-1. Average bond distances to the complexed metal.

Complex	Bond Distance in Angstroms		
	Me - O	Me - N	Me - S
Mg ²⁺ Met	2.05	2.43	2.56
Ca ²⁺ Met	2.35	2.51	2.91
Sr ²⁺ Met	2.49	2.70	N/A
Ba ²⁺ Met	2.68	2.91	N/A

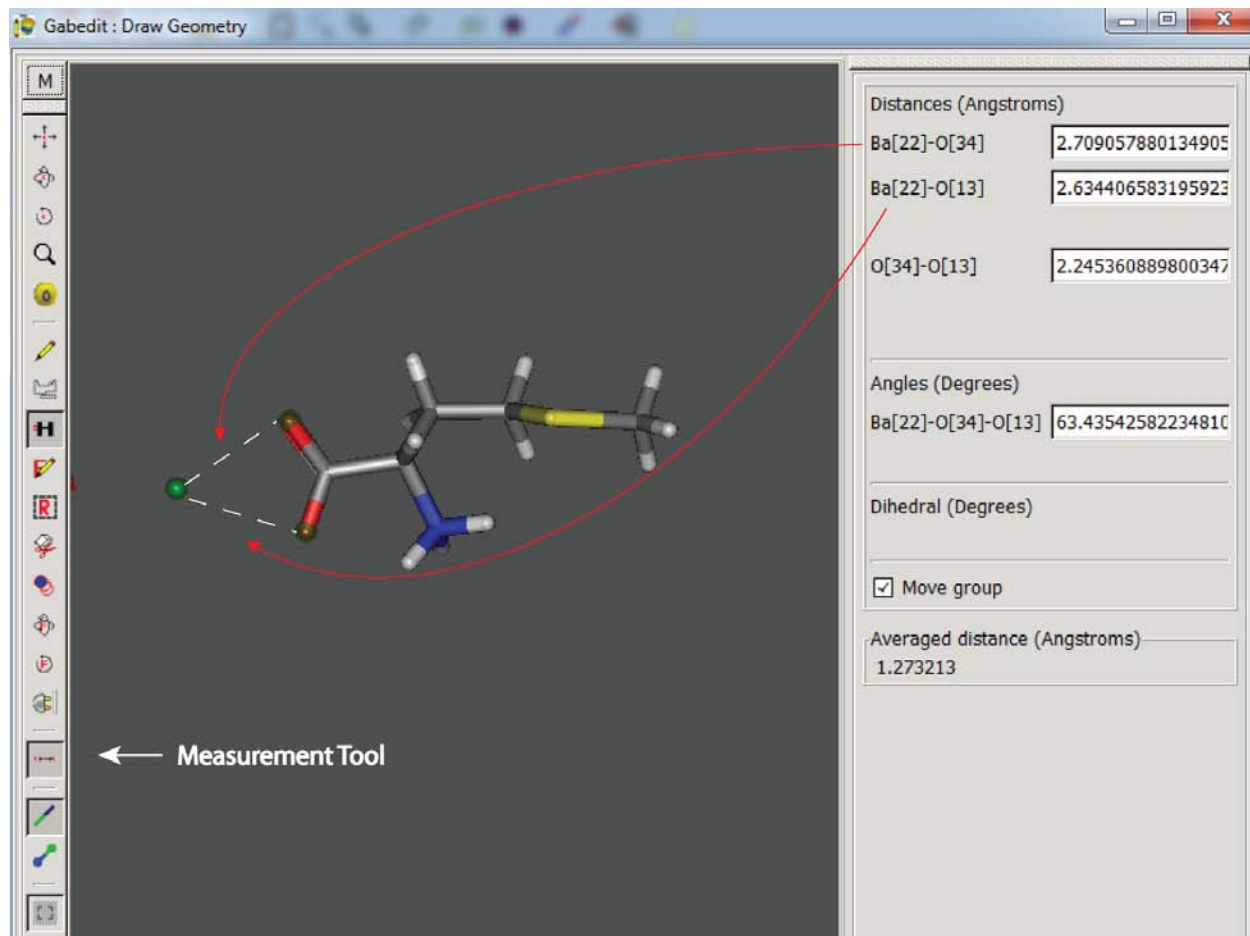


Figure 4-2. Screenshot of Gabedit program, showing Ba²⁺Met Z conformer. This software allows visualization of the structures and determination of interatomic distances, as demonstrated for oxygen-barium distances. Note that barium is highlighted in green, oxygen in red, nitrogen in blue, carbon in grey, and hydrogen in white.

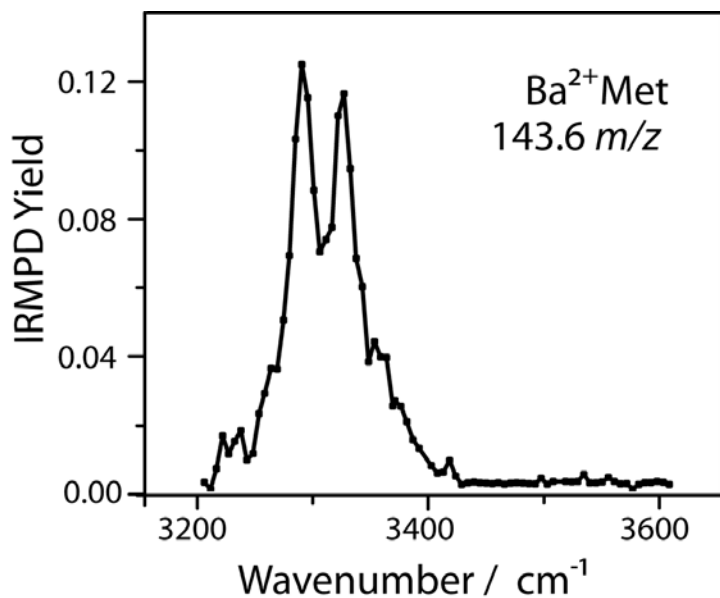


Figure 4-3. IRMPD spectra of the Ba^{2+} methionine complex over the 3200 cm^{-1} to 3650 cm^{-1} range.

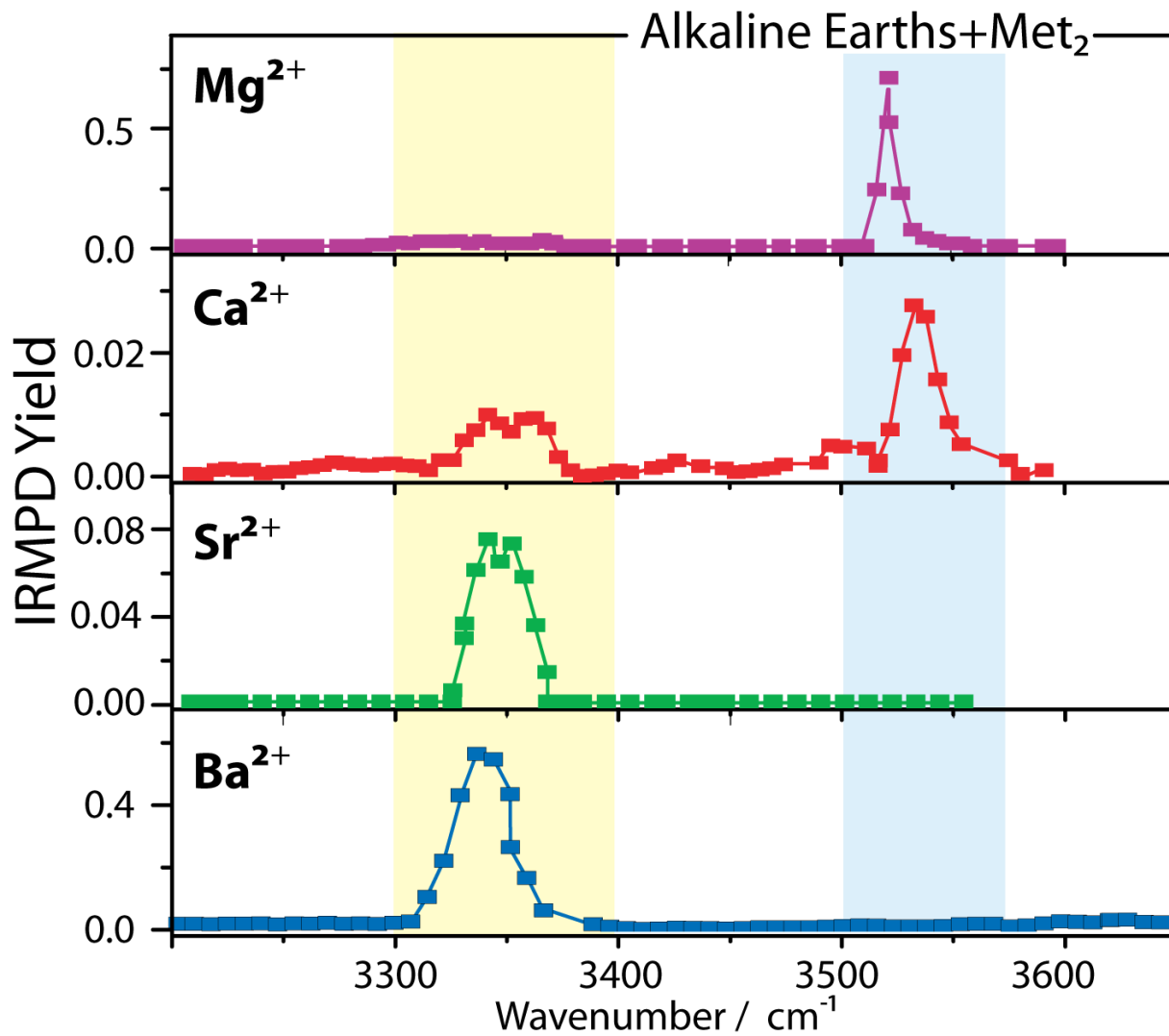


Figure 4-4. IRMPD spectra of the alkaline earths complexed with the methionine dimer in the N-H and O-H stretching regions. Characteristic wavelength regions associated with NH₃⁺ and O-H stretching modes are highlighted in yellow and blue, respectively.

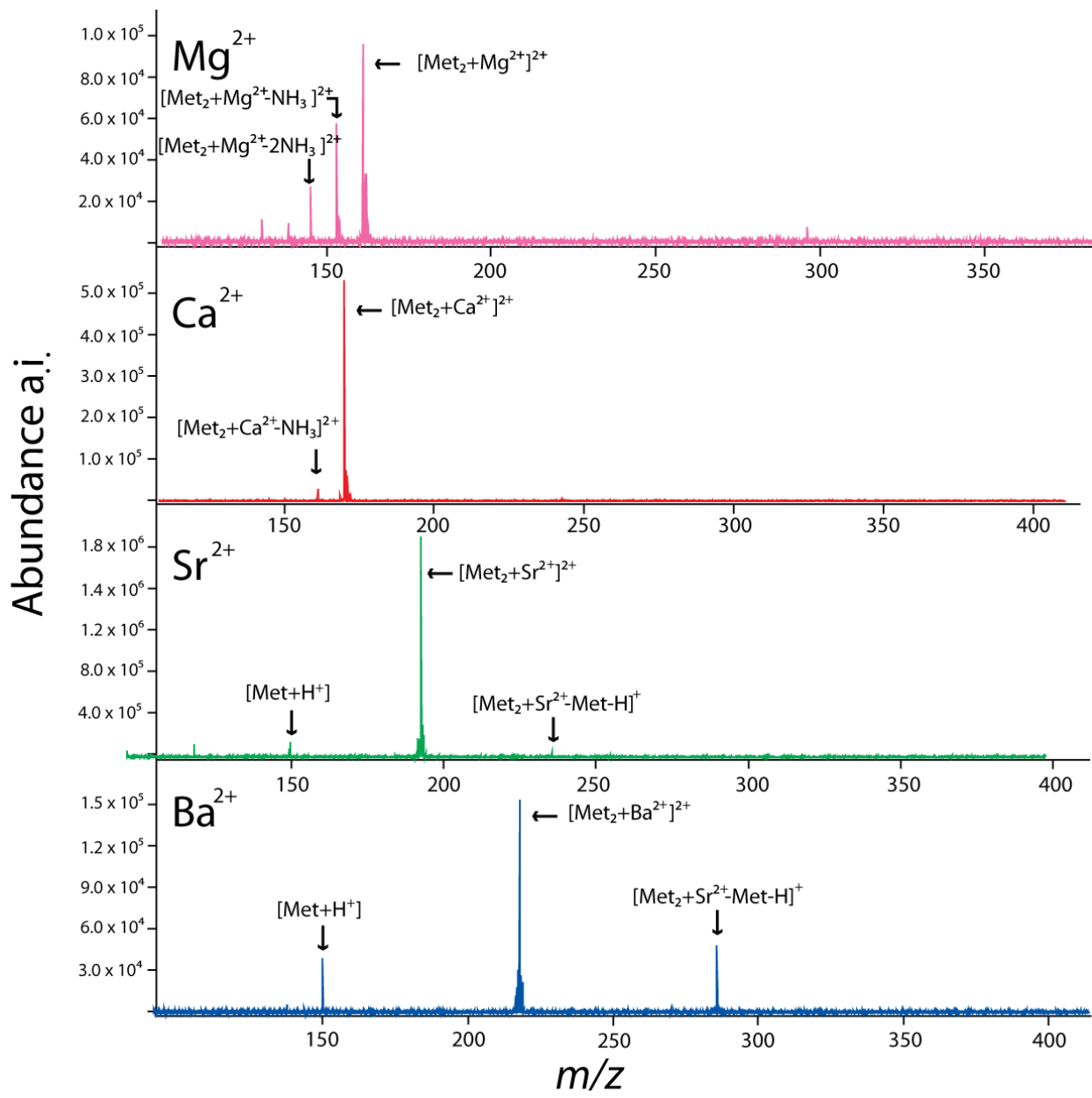


Figure 4-5. IRMPD mass spectra of $M^{2+}Met_2$ under conditions of maximum IRMPD yield. The precursor ions and IRMPD products are labeled.

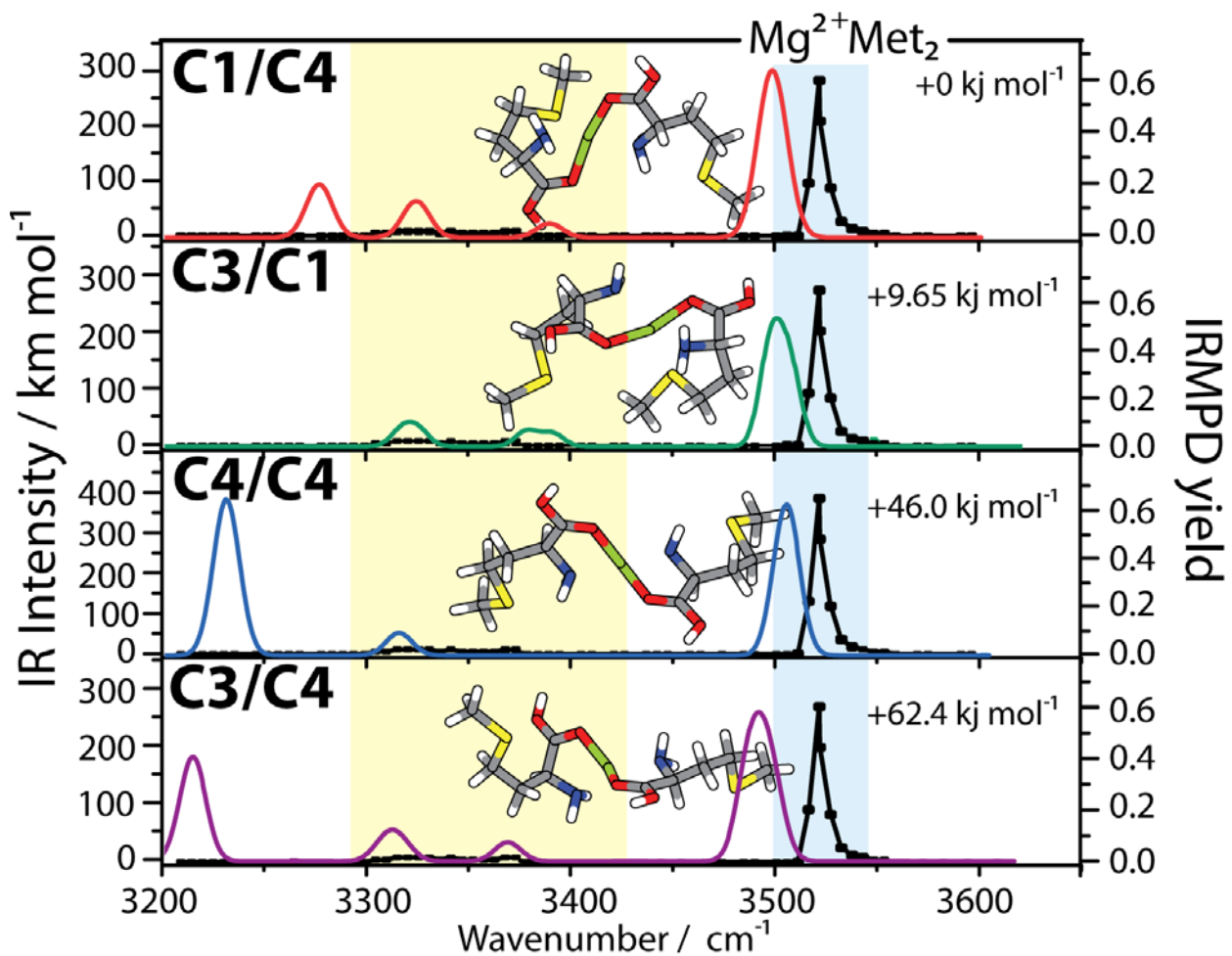


Figure 4-6. IRMPD spectrum of $\text{Mg}^{2+}\text{Met}_2$ in the hydrogen stretching region along with calculated vibrational spectra for the four lowest-energy conformers. Characteristic wavelength regions associated with NH_3^+ and O-H stretching modes are highlighted in yellow and blue, respectively. The zero point-corrected energies of each structure are shown for comparison.

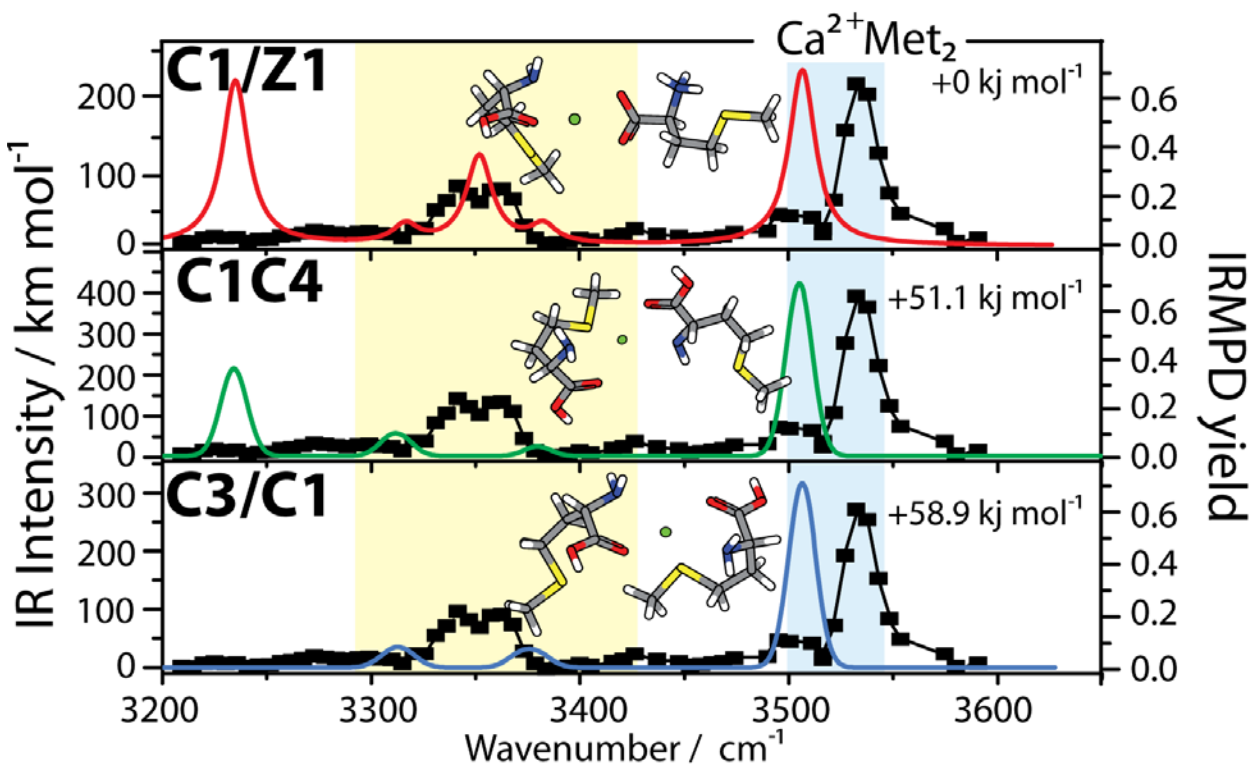


Figure 4-7. IRMPD spectra of $\text{Ca}^{2+}\text{Met}_2$ in the hydrogen stretching region along with calculated vibrational spectra for the three lowest-energy conformers. Characteristic wavelength regions associated with NH_3^+ and O-H stretching modes are highlighted in yellow and blue, respectively. The zero point-corrected energies of each structure are shown for comparison.

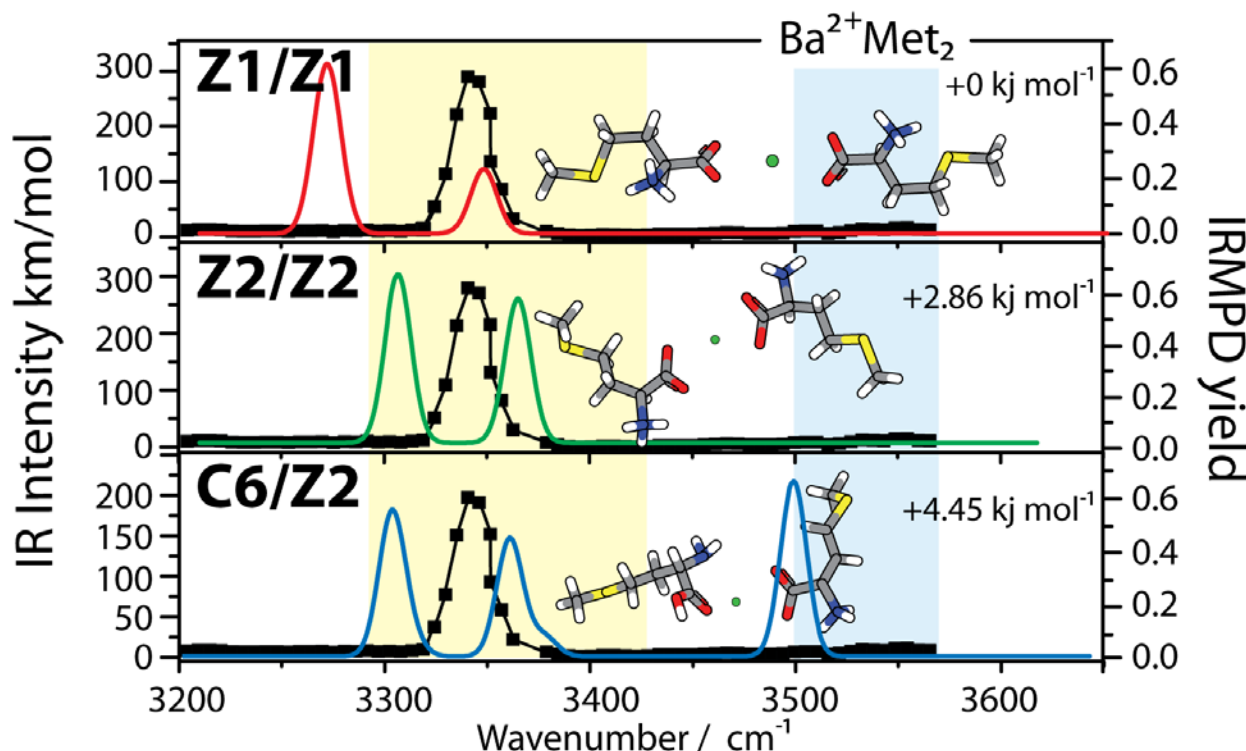


Figure 4-8. IRMPD spectra of $\text{Ba}^{2+}\text{Met}_2$ in the hydrogen stretching region along with calculated vibrational spectra for the three lowest-energy conformers. Characteristic wavelength regions associated with NH_3^+ and O-H stretching modes are highlighted in yellow and blue, respectively. The zero point-corrected energies of each structure are shown for comparison.

Table 4-2. Relative product ion intensities for the alkaline earth complexed series of tryptophan and methionine.

Metal	Tryptophan Fragments	Methionine Fragments	Tryptophan IRMPD structure	Methionine IRMPD structure
Mg^{2+}	100% NH_3 loss 0% TrpH^+ loss	100% NH_3 loss 0% MetH^+ loss	C/Z	C/C
Ca^{2+}	90% NH_3 loss 10% TrpH^+ loss	100% NH_3 loss 0% MetH^+ loss	C/Z	C/Z
Sr^{2+}	60% NH_3 loss 40% TrpH^+ loss	0% NH_3 loss 100% MetH^+ loss	C/C	Z/Z
Ba^{2+}	0% NH_3 loss 100% TrpH^+ loss	0% NH_3 loss 100% MetH^+ loss	C/C	Z/Z

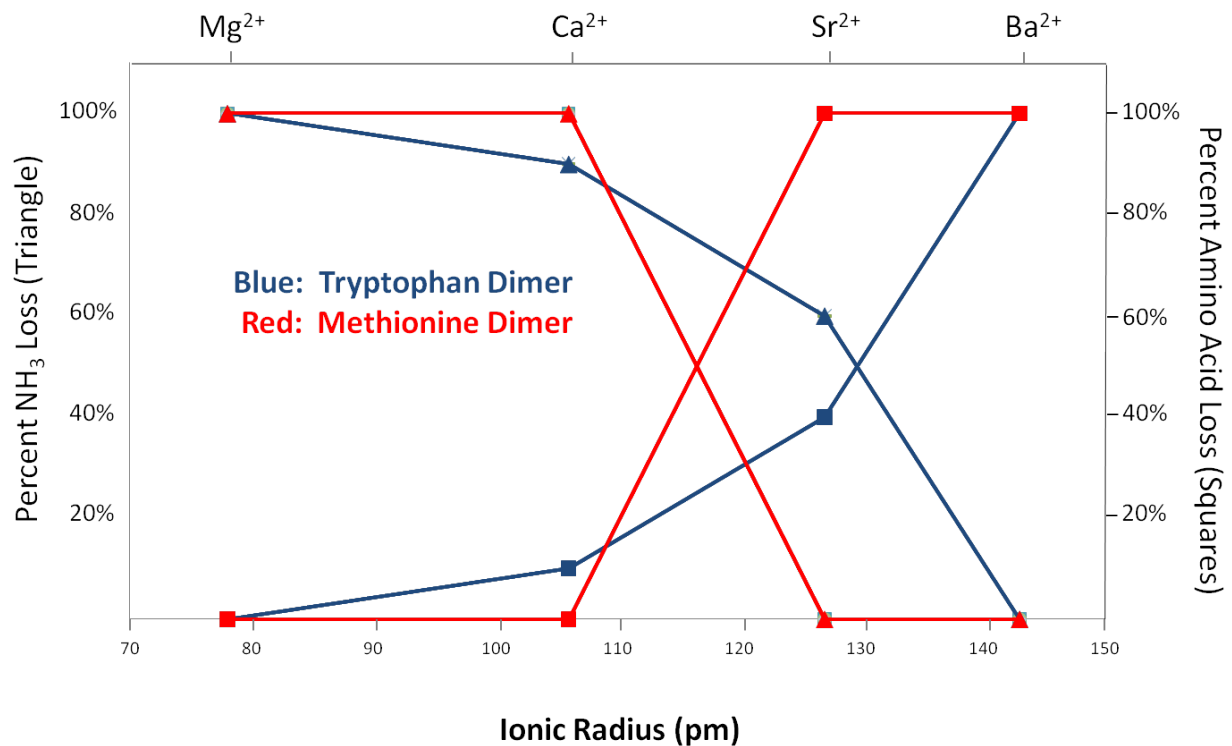


Figure 4-9. Plot of the photofragmentation pathways relative to the complexed metal ion ionic radius.

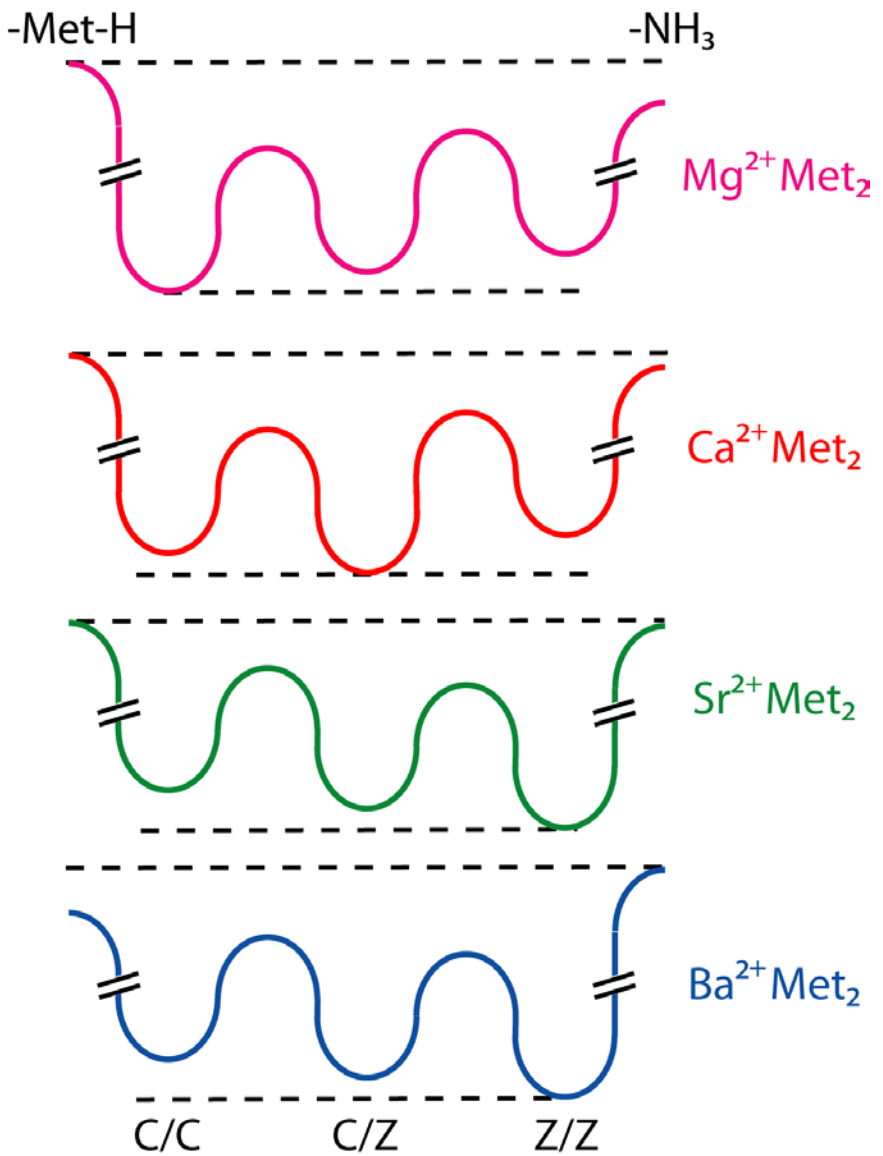


Figure 4-10. Cartoon of the energy wells and barriers for dissociation chemistry of each metal amino acid complex.

CHAPTER 5

INFRARED MULTIPLE PHOTON DISSOCIATION SPECTROSCOPY OF IONS IN PENNING AND QUADRUPOLE ION TRAPS

Introduction

Infrared multiple photon dissociation (IRMPD) spectroscopy is an emerging technique that can unlock chemically selective information on gas-phase ions, unattainable from conventional dissociation techniques,^{53,117,182} such as collision induced dissociation.^{175,183-186} The general purpose of a dissociation technique in mass spectrometry is to obtain information on the structure of the precursor ion based on fragmentation products. For example, in proteomics research, a protein's sequence can be identified by identifying the peptides that make up the protein. A peptide's sequence can be identified based on the *m/z* of the detected fragments. Once multiple peptides are identified, the peptide information can be used to reconstruct the primary structure of the target protein.²⁵ The advantage of IRMPD spectroscopy over standard dissociation techniques is that in addition to generating a fragment ion mass spectrum, wavelength-specific information is obtained that can identify chemical moieties in the precursor ion. In other words, IRMPD spectroscopy yields more direct information on the structure of the precursor ion prior to ion activation.

This chapter discusses work that improved IRMPD spectroscopy in two different types of ion traps, specifically, the Penning trap of an FT-ICR mass spectrometer and a reduced-pressure quadrupole ion trap (QIT) ($\sim 10^{-5}$ Torr) of a custom-built mass spectrometer. Ion trapping conditions in the Penning trap were manipulated to increase the overlap of the ion cloud with the optical parametric oscillator (OPO) laser beam, and hence improve the photodissociation yield. Furthermore, experiments were performed by coupling the OPO laser to a QIT on a custom-built mass spectrometer to evaluate

the performance of IRMPD spectroscopy in a different ion trap. Protonated tryptophan, TrpH⁺, was used as a standard to compare the IRMPD efficiency in both instruments.

In the custom-built instrument, the IRMPD spectra for two collision induced dissociation (CID) fragments from TrpH⁺, [Trp+H-NH₃]⁺ (17 amu loss), and [Trp+H-NH₃-CH₂CO]⁺ (42 amu loss), were also recorded to identify the fragmentation mechanisms. By conducting experiments on simple systems, such as single amino acids, it may be possible to identify fragmentation chemistry in more complex systems, such as peptides, which underpins identification in proteomic studies.

Experimental

Materials

Standard compounds of Ba(NO₃)₂, L-Trp and L-Met (Acros Organics) were dissolved in HPLC-grade water (Fisher Scientific) at a concentration of 10⁻² M to prepare the stock solutions for the experiments. For the Ba²⁺Met complex, the L-Met and Ba(NO₃)₂ stock solutions were combined and further diluted to a concentration of 10⁻³ M. For the TrpH⁺ complex, the stock solution was diluted to 10⁻³ M and 0.1% by volume of acetic acid was added to aid in protonation of the species. The solvent for both complexes was a 70:30 mixture of methanol/water.

Mass Spectrometry and Ion Spectroscopy

The Ba²⁺Met and TrpH⁺ complexes were formed by electrospray ionization (ESI) using a commercial 4.7 T Apex II Fourier transform ion cyclotron resonance (FT-ICR) mass spectrometer (Bruker Daltonics, Billerica, MA) and a custom-built mass spectrometer equipped with a quadrupole mass filter, quadrupole ion trap, and a time-of-flight mass analyzer (QMF-QIT-ToF).

Penning trap

The specifics of the experiments performed in the Penning trap are discussed in detail in Chapters 3 and 4. Briefly, the precursor ion was mass isolated and infrared multiple photon dissociation (IRMPD) spectroscopy was performed by irradiating the precursor ion in a step-wise fashion with the tunable output (2500 cm^{-1} – 4000 cm^{-1}) of a continuous-wave (cw) periodically poled LiNbO₃–optical parametric oscillator (OPO) OS4000 laser (LINOS Photonics, Germany) in the Penning trap. The IRMPD spectra were generated by plotting the IRMPD yield, $\text{yield} = -\ln[1 - \{\sum \text{int}_{\text{photofragments}} / (\sum \text{int}_{\text{photofragments}} + \sum \text{int}_{\text{precursor}})\}]$, as a function of the OPO idler wavenumber. OPO laser irradiation was then followed by CO₂ laser (SYNRAD J48-5W, Mukilteo, WA) irradiation at 2 W, to boost IRMPD yield.

Custom-built instrument equipped with a quadrupole ion trap

A schematic of the custom-built instrument optimized for IRMPD spectroscopy is shown in Figure 5-1. A solution containing the analyte of interest is pumped via a syringe pump (Harvard Apparatus, Inc., Holliston, MA) at a rate of $3\text{ }\mu\text{L min}^{-1}$ through a commercially available electrospray ionization source (Analytica of Branford, Branford, CT). The needle of the electrospray source is directed at a 45° angle relative to the capillary entrance of the mass spectrometer. A 4.5 to 5kV bias is applied across the electrospray needle and the capillary entrance to induce the formation of charged droplets. The charged droplets desolvate during the transfer through the heated capillary and exit the capillary as gas-phase ions. The voltage drop between the capillary exit potential (e.g. +80–400 V) and the skimmer can be adjusted to perform collision induced dissociation (CID) via ‘nozzle-skimmer’ dissociation. The fragment ions, [Trp+H-NH₃]⁺ (*m/z* 188), and [Trp+H-NH₃-CH₂CO]⁺ (*m/z* 146), were generated in

this way by in-source CID. The skimmer orifice is 2 mm, and hence presents a conductance limit to a 20 cm long hexapole ion guide, in the next pumping stage. An rf voltage is applied to the hexapole and the amplitude of the rf can be adjusted to optimize ion signal. Note that the polarity of the rf applied is the same for every other pole, and the poles in between are exactly 180° out of phase. Furthermore, a DC voltage is applied to the hexapole, +11 V, which serves as the cation bias for transmission through the mass spectrometer.

The ions exit the hexapole and are directed through an Einzel lens to focus the ion packet into a DC quadrupole deflector. On axis with the hexapole is a multiplier detector (not shown), which can be used to optimize the ionization conditions of the source without having to optimize other ion optics in the mass spectrometer. The custom built instrument also includes an electron ionization (EI) source orthogonal to the hexapole and multiplier detector (not shown). The EI source generates ions from a diffuse gas by impacting the neutral gas with high kinetic energy electrons. The impact of the electron results in odd electron, or open shell, cations that can be analyzed by the mass spectrometer. The EI source is generally used for testing the set-up.

Typical instrument operation results in ions generated by the ESI source steered 90° by the DC quadrupole deflector into a quadrupole mass filter (QMF) for mass filtering. A second deflector follows the QMF, to direct the ions 90° toward a second multiplier detector (not shown) or a rectilinear ion guide/trap (RIT). The second multiplier detector can be used to optimize the ion signal from the ion source (ESI or EI), via both deflectors and the QMF. The QMF contains four 9 mm rods 8 inches in length operated by an rf power supply (Aradara Technologies, Monroeville, PA). Further discussion of

operating a QMF and filtering ions by *m/z* can be found in Chapter 2. Briefly, the power supply feeding the QMF is capable of a maximum rf amplitude of 5,000 Vpp and an rf frequency of 1MHz.

For the IRMPD spectroscopy experiments, deflector 2 is operated to guide the ions into the RIT. The RIT has three segments to efficiently store ions, which later are pulsed into the quadrupole ion trap (QIT) for dissociation experiments. The three segments of the RIT are biased at consecutively lower DC potentials (e.g. +7, +5 and +2 V). The last segment of the RIT is followed by a 6 mm disk electrode that is biased at +50 V DC during ion accumulation mode. Thus the ions, biased from the hexapole at +11 V should not be able to pass this potential and remain trapped in the RIT. However, since the ions are biased at +11V it is possible for the ions to exit the entrance of the RIT (biased at +7 V). This is counteracted by a He buffer gas applied to the RIT. The ions undergo collisions in the RIT, which over time results in an accumulation of ion in the last segment and their collisional re-biasing at the potential of the last segment (i.e., +2 V). The stored ions are then guided into the QIT by pulsing the disk electrode to -50 V.

Prior to pulsing the ions into the QIT, He buffer gas is introduced in the QIT ion trap via a pulsed solenoid valve through the first space in the QIT. Figure 5-2 illustrates the timing of events required to successfully trap and perform tandem MS experiments. The current sequence has a total cycle time of 2 seconds, including an IR irradiation time of 1.5 seconds. Note that the timing events illustrated are controlled by a delay generator (Stanford Research Systems). The solenoid valve is opened for 2 ms with a backing pressure of He buffer gas at 50-60 Torr. The build-up of a buffer gas when the

ions arrive in the QIT serves to collisionally cool the ions to the center of the QIT for sufficient storage. Once the ions are cooled to the center of the trap, the buffer gas is no longer required for storage and is pumped away by a high-speed turbo pump (Pfeiffer 700 l/s turbomolecular pump). Note that at a base pressure of 10^{-5} Torr in the QIT, no ions would be trapped. The second spacer was removed to ensure that the He gas could be quickly pumped away (~50 ms) prior to OPO laser irradiation. In the experiment, this pump down delay was often elongated to 300 ms to ensure a lower background pressure.

The QIT is a “Paul type” ion trap with two hyperbolic endcaps separated by 14.3 mm with a hyperbolic ring electrode within the endcaps with an inner diameter of 20.3 mm (Jordan ToF Products, Grass Valley, CA). Ions enter and exit the trap via 3.2 mm diameter endcap apertures. The ring electrode has an rf frequency applied via a power supply controlled by an arbitrary waveform generator (Stanford Research Systems DS345). During trapping the rf amplitude is sufficiently low ($300\text{ V}_{\text{p-p}}$) such that all ions are trapped efficiently, the rf amplitude is then ramped to destabilize the trajectories of low m/z ions while retaining the precursor ion in the trap. The varying rf amplitude allows for mass isolation of a precursor ion to obtain background free spectra while performing IRMPD experiments.

The OPO laser discussed in the previous chapters was interfaced to the QIT for IRMPD spectroscopy experiments. The two OPO laser beams are directed into the vacuum chamber via an IR transparent BaF₂ window where they are focused with a 70.4 mm focal length plano-convex lens into the QIT. The beam waist of each focused OPO beam was on the order of <100 μm , which corresponds to a laser flux of 280

W/cm^2 for the maximum laser power (i.e., 25 mW per beam). Optical access is provided by an aperture (2.4 mm) in the ring electrode. A shutter driven by a digital delay generator (Stanford Research Systems DS645) alters the timing and duration of the laser irradiation. Typically, the ion cloud is held in the QIT for 300 ms prior to irradiation (See Figure 5-2).

The resulting photofragment ions were then pulsed out of the QIT into the time-of-flight (ToF) drift tube for mass analysis. The rf power supply allows a fast switch-off of the rf amplitude (i.e., <2 rf cycles). The ions are then directed into the ToF drift tube by pulsing the voltages on the front and rear endcaps of the QIT from ground (0 V) to +700V and -700V, respectively. The ToF mass spectrometer is a commercial (Jordan ToF Products, Grass Valley, CA) reflectron type drift tube with a distance of ~1.1 m between the QIT and reflecting electrodes. The fundamentals of ToF mass analysis are covered in detail in Chapter 2. Briefly, ions of different m/z biased at the same potential will transverse the drift tube at different velocities, resulting in separation based on m/z , thus providing mass analysis. The ions are collected by a multi-channel plate (MCP) detector at the end of the ToF drift tube. The analog signal is amplified (3x) by a pre-amplifier and is digitized with a 1GHz digitizer (National Instruments NI5154). Typically, ten mass spectra are averaged on the digitizer card and recorded as one mass spectrum.

The tandem MS experiments (here: IRMPD experiments) performed can be discussed as “in space” or “in time” for the QIT or Penning trap set-ups, respectively. An illustration of the mass spectrometric workflow for both instruments used is shown in Figure 5-3. In short, tandem “in space” suggests that more than one mass analyzer is

used for analysis. The custom-built instrument is operated “in space” as there are multiple mass analyzers. The QMF is used to mass select the ions, the QIT is used to store the ions for dissociation techniques, and the ToF is used for mass analysis. Tandem “In time” suggests a single mass analyzer that can store ions for a certain period of time. The Penning trap in the FT-ICR mass spectrometer operates in time, since the ions are held in the Penning trap for the duration of the experiment. Therefore, compared to the custom-built instrument, the Penning trap can mass isolate, similar to the QMF, store ions for fragmentation, similar to the QIT, and mass analyze the sample, similar to the ToF.

Previously, IRMPD spectra recorded on the Penning trap were processed in Excel; however, the peak heights of the precursor ion and fragment ions were manually entered. To aid in data processing for experiments performed on the custom built set-up, a program written in LabVIEW was incorporated to automatically process the ToF mass spectra and generate IRMPD spectra. The program interface can be seen in Figure 5-4. ToF mass spectra are uploaded into the program. As each mass spectrum is uploaded, the program looks for changes in the baseline and assigns gates, indicated as red, green, and blue. These gates mark the mass ranges over which integration of the mass peaks is carried out. Before the integration is performed, the program asks the user to make sure the gates are correctly aligned. The gates can be manually adjusted, removed or added for the integration process. The integration function re-processes all the mass spectra, this time calculating the area of each peak within the assigned gates and the IRMPD yield, $\text{yield} = -\ln[1 - \{\sum \text{Area}_{\text{photofragments}} / (\sum \text{Area}_{\text{photofragments}} + \sum \text{Area}_{\text{precursor}})\}]$. The program plots the power corrected IRMPD yield for each mass

spectrum vs. the associated irradiation wavenumber. Processing the data via LabVIEW has two major advantages. 1) The automation significantly decreases the time of post-experiment data processing. 2) The automation eliminates the possibility of user error while manually recording peak values and wavenumbers.

Calculations

Chemical structures generated for the TrpH^+ , $[\text{Trp}+\text{H}-\text{NH}_3]^+$, and $[\text{Trp}+\text{H}-\text{NH}_3-\text{CH}_2\text{CO}]^+$ ions were completed in the Gabedit¹⁸⁰ software package, followed by further optimization with density functional theory (DFT) with the Gaussian03¹⁵⁸ software package, employing the B3LYP functional with a 6-31+G* basis set. In addition to optimization calculations, vibrational stick spectra were computed and broadened with a Gaussian function to 15 cm^{-1} FWHM (full width at half-maximum). Furthermore, scaling factors for the O-H (0.976), N-H (0.959) and C-H (0.961) vibrations were applied due to anharmonicity differences arising from the different chemical moieties.¹⁸⁷ In short, the theoretical calculations predict harmonic vibrations; however, because of anharmonicity, experimental values are typically red shifted from the harmonic theoretical calculations. In the hydrogen stretching region, the differences in anharmonicities between different vibrations can be particularly pronounced.¹⁸⁷ The calculated spectra were plotted with band intensities in km mol^{-1} for more convenient comparison to experimental results. The zero-point energy (ZPE) corrected energies shown are calculated at the B3LYP/6-31+G* level of theory; however, further calculations were performed with the M05-2X and MP2 functionals to account for dispersion forces.

Results and Discussion

Laser Set-up in the Penning trap

As described in Chapter 2, the motion of the ions in the Penning trap is governed by the magnetic field in a plane orthogonal to the magnetic field direction, while being constrained by DC voltages applied to the trapping plates in the direction of the magnetic field (Figure 2-6). Thus, the ion cloud is distributed symmetrically if the two trapping voltages are equal. In our case, the front trapping plate was held at 1.40 V and the back trapping plate was held at 1.40V.

In a typical IRMPD experiment, the laser beam can be introduced via an aperture (6 mm) in the trapping plate. The CO₂ laser that we have coupled to the FT-ICR is aligned down the z-axis; thus partially blocking this optical access for the OPO laser. An illustration of the laser set-up is given in Figure 5-5. The figure shows the CO₂ laser beam directly in line with the z-axis, but the two OPO laser beams are directed down the z-plane at an angle of 1.9 degrees. In an ideal set-up, the two OPO laser beams would cross in the center of the trap with a minimal angle, resulting in maximum overlap of the ion cloud with the laser beam. However, due to the physical constraints and orientation of the Penning trap, the exact position of the laser beam relative to the ion cloud is unknown and the laser alignment is difficult to verify. Therefore, alignment is performed by adjusting the two laser beams and monitoring the IRMPD yield; however, exact laser beam ion cloud overlap cannot be verified in this way.

Furthermore, the laser set-up illustrated in Figure 5-5 is contained in a purge box saturated with N₂ gas. The operating wavelength region of the OPO is in the O-H stretching region of the IR spectrum. Thus, as the laser beam is directed into the Penning trap via steering mirrors, water molecules in the air can absorb IR photons

before they reach the cell. This effect can be seen on the power meter without the N₂ gas flowing in the purge box. A listing of the H₂O bands in the IR spectrum is given in Table 5-1. Power corrections are performed on the IRMPD yield to account for fluctuations in power; however, these bands can significantly reduce the number of photons for the IRMPD experiments, thus adversely affecting the experiments.

Effect of Trapping Condition on IRMPD

The position of the ion cloud relative to the z-axis can be adjusted by changing the trapping potentials of the Penning trap. The trapping potentials can be varied from 0–10 V; however, reducing the potentials below 1.4 V results in significant ion loss. To adjust the ion cloud without adversely affecting the trapping efficiency, the ions are trapped at standard conditions in the instrument, i.e., the front trapping plate at 1.40 V and the back trapping plate at 1.40 V. With these conditions, the ion cloud moves freely along the z-axis in the Penning trap, resulting in a ‘cigar-like’ shaped ion cloud, spread over a few cm. The trapping plates were then ramped stepwise to other trapping potentials for irradiation and then stepwise brought back down to the standard trapping potential (1.40V) for excitation and detection. The effect of altering the trapping voltages on the potential field along the z-axis was calculated using SIMION¹⁸⁸ and is illustrated in Figure 5-6. The plot shows that as the potential on the front trapping plate is raised, the potential well in the Penning trap is distorted and the minimum potential position is shifted toward the back trapping plate. Thus, by adjusting the trapping voltages, the potential well, and thus the ion cloud, can be manipulated in the Penning trap to maximize overlap with the OPO laser beam.

To obtain a better understanding of the ion cloud in the Penning trap, the kinetic energy distribution of the ions was measured, which is shown in Figure 5-7. The front

and back trapping plates were reduced in voltage (i.e., 500 ms) prior to increasing the voltage back to 1.4 V on both plates, followed by exciting and detecting the remaining ions. This control experiment relies on the assumption that ions of higher kinetic energy (than the voltage of the trapping plates) are lost from the Penning trap. The ion abundance plot as a function of trapping potential shows a sigmoidal-like distribution. There is a sharp drop-off in the ion abundance centered at ~1.25 V. This is more easily visualized by the derivative plot, $\partial \text{Int}/\partial V$, which represents the incremental change in ion abundance as a function of reduced trapping potential. This means that the average kinetic energy of the ions is centered around 1.25 V (+/- 0.05 V), which is close to the DC bias of the hexapole (in the ESI source of the FT-ICR instrument). There is nonetheless a tailing of the ion abundance at lower kinetic energy, which suggests that some ions have reduced kinetic energies.

The average kinetic energy distribution can be compared to the potential energy simulations in Figure 5-6 to estimate the effect on the ion cloud from employing asymmetric trapping potentials during laser irradiation. By, for instance, changing the front trapping voltage from 1.4 V to 8.9 V the ion cloud is “squeezed” by a factor of 2 in the axial direction.

Figure 5-8 shows a plot of the IRMPD yield of the Ba^{2+}Met monomer complex versus the potential applied to the front trapping plate. The OPO irradiation (10 s) was fixed at an idler wavenumber of 3345 cm^{-1} , which corresponds to the maximum absorption band of the NH_3^+ stretch.. As the front trapping plate potential is raised, an increase in photofragmentation yield is observed. This suggests that the two OPO beams intersect closer to the rear of the Penning trap, rather than the center. The

manipulation of the trapping conditions resulted in a 2.5-fold linear increase in signal gain by increasing the front trapping plate between 1.4 V to ~8.9 V and holding the back trapping plate constant at 1.40 V. This roughly mirrors the “squeezing” of the ion cloud in the axial direction. Beyond 8.9 V, the IRMPD yield decreases, which may, in principle, be due to two effects: 1) either the ion cloud was moved beyond the overlap region of both laser beams, or 2) the ion cloud was squeezed too much, thus resulting in space-charge effects, which result in larger magnetron radii for the ions. In the latter case, the ions are dispersed radially away from the central axis of the trap, thus resulting in lower IRMPD yield. In summary, the tuning of the laser beams and the ion cloud results in optimized ion cloud-laser beam overlap, which is essential in detecting weaker vibrational features, such as the NH_3^+ asymmetric stretch.

Dual-laser IRMPD yield

The comparison of the Ba^{2+}Met monomer IRMPD yield irradiated with the OPO alone and the combination of the OPO and CO_2 lasers is shown in Figure 5-9. The OPO irradiation was fixed at an idler wavenumber of 3345 cm^{-1} , or the peak of the weakest NH_3^+ stretching mode. Furthermore, the trapping conditions of the Penning trap were set to 8.9 V for the front trapping plate and 1.40 V for the back trapping plate. The OPO irradiation time was increased from 0 to 15 s in one-second intervals. For the OPO-only results, the IRMPD yield increases linearly with irradiation time, which would be expected for a first-order rate process (since the IRMPD yield is on a natural logarithm scale). This suggests that the overlap between the laser and the ion cloud remains fairly constant during the time of irradiation. The CO_2 irradiation was subsequent to the OPO laser irradiation and was fixed at 500 ms. The combined OPO- CO_2 results show a consistently higher IRMPD yield; however, this effect is much more pronounced for

shorter OPO irradiation times, whereas both sets of results converge at longer OPO irradiation times. It is clear that the CO₂ laser mainly enhances the IRMPD yield for those ions that are vibrationally excited, but whose internal energy is below the dissociation threshold. As a larger proportion of the ion population is dissociated with the OPO laser for longer irradiation times, the enhancement factor of the CO₂ laser becomes much reduced. Furthermore, space-charge effects can radially distribute the ions in the Penning trap, resulting in a loss of overlap with the laser beam. Longer irradiation times will allow ions to drift out of the irradiation region, thus losing the IRMPD enhancement. Nonetheless, the combined OPO-CO₂ laser approach can reduce the duty cycle. For instance, a 4 sec irradiation time for the OPO-CO₂ method results in a similar IRMPD yield as a ~7 sec irradiation time with the OPO laser alone.

Protonated Tryptophan IRMPD Spectrum in the Penning Trap

In order to make a comparison of IRMPD performance in the Penning trap and the QIT, a standard for IRMPD yield needed to be developed and tested in both systems. Although all experiments throughout this dissertation have been done in the Penning trap and could be viable standard candidates, the metal complexed ions were difficult to generate in the custom-built mass spectrometer. On the other hand, protonated amino acids are easy to generate on both mass spectrometers and were hence chosen as the standard for comparison.

The full IRMPD spectrum of protonated tryptophan acquired in the Penning trap, from 2950 cm⁻¹ –3650 cm⁻¹, is shown in Figure 5-10. The OPO irradiation time was fixed at 10 s followed by irradiation with the CO₂ laser for 500 ms. The trapping conditions were set to 8.9 V and 1.40 V for the front and back trapping plates, respectively. The two major fragmentation bands at 3550 cm⁻¹ and 3500 cm⁻¹ are assigned to the

carboxylic acid O-H stretch and the indole ring N-H stretch. A third, smaller band is observed at 3335 cm^{-1} and is assigned to the NH_3^+ antisymmetric stretching mode. In addition to these three bands, there are potentially weaker features between 3050 cm^{-1} and 3200 cm^{-1} ; however, these are at the detection threshold of the IRMPD experiment.

Protonated Tryptophan IRMPD Spectrum in the Quadrupole Ion Trap

The OPO laser used for the Penning trap experiments was removed from the FT-ICR mass spectrometer and coupled to the custom-built mass spectrometer, where the OPO laser beams are introduced via apertures in the ring electrode (see Figure 5-1). The set-up is similar to the previous laser configuration used on the Penning trap, except for a few changes to increase ion cloud and beam path overlap. Inherently, the ion cloud in the QIT is smaller compared to that in the Penning trap. The ion cloud diameter in the QIT is on the order of 1 mm and has a somewhat uniform circular shape, whereas in the Penning trap it is stretched over a few cm. Since the ion cloud is smaller than the standard beam profile of the OPO (i.e., 3 mm), a focusing lens was employed to increase the laser flux on the ion cloud, and increase the efficiency of the IRMPD process.

Penning traps are typically maintained at an ultra-high vacuum of $\sim 10^{-10}\text{ Torr}$ to minimize collisions during trapping and detection, as collisions adversely affect the detection efficiency and resolution. The lower pressure is an advantage to IRMPD experiments, as collisions ‘cool’ the ions, hindering the photodissociation process; this is especially important in the case of the OPO laser, where photodissociation results from a slow heating of the ion.

Typical QITs require an operating pressure of 10^{-3} Torr , because the QIT relies on collisional cooling of the ions to the center of the trap, allowing for stable trajectories and

efficient storage of ions. As discussed in the experimental section, a pulsed valve was incorporated to pulse He gas into the trap, giving the user more pressure control. Specifically, the valve allows the pressure in the QIT to increase during ion injection and decrease during the IRMPD experiments. The base operating pressure is maintained at 10^{-5} Torr, which is 2 orders of magnitude lower than that of conventional QITs.

Figure 5-11 shows the IRMPD spectrum of protonated tryptophan in the QIT from 2950 cm^{-1} to 3700 cm^{-1} for a laser irradiation time of 1.5 s and 150 ms. Compared to the IRMPD spectrum recorded on the FT-ICR mass spectrometer, at 1.5 s of irradiation there are significant improvements in dissociation yield in all modes of the spectrum. The most striking result is the appearance of a number of modes at lower frequency in the 3000 to 3200 cm^{-1} range, which were not visible in the Penning trap experiments (similar to the spectrum recorded at 150 ms). Moreover, the IRMPD yield at 3550 cm^{-1} reaches infinity, as a result of complete dissociation of the precursor ion. For a lower irradiation time of 150 ms, the IRMPD yield of the 3550 cm^{-1} band drops to an IRMPD yield of 4. All of the band positions and assignments are summarized in Table 5-2. Note that the band positions do not change as a function of the irradiation time.

In addition to the photofragmentation improvements seen in the QIT over the Penning trap experiments, the overall cycle time (irradiation from 10 s to 1.5 s) was significantly reduced. Considering that each point on the IRMPD spectrum is typically the average of 10 mass spectra, the reduction in time compiles quickly. Furthermore, the experiments did not require a second laser approach, as the fragmentation yields were significant with the OPO alone. This reduces the complexity of the experiment,

and eliminates the possibility of background dissociation, which could occur during irradiation with a second laser.

To confirm peak assignments, the TrpH⁺ experimental spectrum recorded on the QIT was compared to theoretical spectra. The overlay of the four lowest energy structures with the experimental spectrum can be seen in Figure 5-12. The predicted frequencies of the carboxylic acid O-H at 3550 cm⁻¹ and indole N-H at 3500 cm⁻¹ differ slightly between conformers, yet the lower frequency modes associated with the terminal amine, NH₃⁺ show considerable differences across different geometries. The calculations suggest that the broad feature found in the experiment spectrum between 2950 cm⁻¹ and 3200 cm⁻¹ could be explained by the combination of the conformers. The energies given for the theoretical structures are from the B3LYP/6-31G+* level of theory. The frequency calculations were scaled using 0.976 for the O-H, 0.959 for N-H, and 0.961 for C-H, as recommended by Lisy.¹⁸⁷

Other theoretical calculations were performed to incorporate dispersion forces, M05-2X and MP2, which resulted in the Figure 5-12C conformer being the lowest in energy; however, for all three levels of theory, the maximum spread of energies was within 9 kJ mol⁻¹. The energies calculated are tabulated in Table 5-2. Such a small difference in energy suggests that all conformers are energetically accessible, supporting the conclusion that the broad feature in the experimental spectrum could be a function of the different geometries.

In all of the theoretical geometries in Figure 5-12, one hydrogen from the terminal amine, NH₃, interacts with the aromatic side chain and another hydrogen is in a hydrogen bonding network with the carboxylic acid, COOH. Other higher energy

structures exist employing other bonding networks. Shown in Figure 5-13 is the lowest energy structure with three other higher energy structures compared with the experimental TrpH⁺ spectrum. Optimized geometries where the NH₃⁺ group interacts with the hydroxyl O, or has no interaction with the aromatic side chain, results in intense NH₃⁺ vibration in the 3280 to 3300 cm⁻¹ range, which is not confirmed experimentally. This suggests that the hydrogen-bonding network with the aromatic side chain and carboxylic acid remains intact even at room temperature.

Collision-induced dissociation of TrpH⁺

The dissociation chemistry of TrpH⁺ was explored by generating NH₃ loss, [Trp+H-NH₃]⁺ (m/z 188), and subsequent CH₂CO loss, [Trp+H-NH₃-CH₂CO]⁺ (m/z 146), CID products. The mass spectrum in Figure 5-14 shows the appearance of these CID products via IRMPD. Each of these fragments was generated in-source and mass selected by the QMF, as described above in the experimental section. An advantage of the custom-built mass spectrometer is that fragment ions generated by nozzle-skimmer dissociation can thus be mass selectively enriched via storage in the RIT prior to pulsing into the QIT for IRMPD studies.

The IRMPD spectrum of TrpH⁺ (top) is contrasted to the 188 m/z fragment, [Trp+H-NH₃]⁺ (middle), and the 146 m/z fragment, [Trp+H-NH₃-CH₂CO]⁺ (bottom) in Figure 5-15. The comparison shows that upon fragmentation from TrpH⁺ to [Trp+H-NH₃]⁺, the NH₃⁺ modes are lost, which is expected from the neutral loss of NH₃. The interesting difference between the spectra is the 75 cm⁻¹ red shift in the indole N-H stretch. This suggests that the delocalization of the electrons on the side chain has changed, most likely due to the charge of the ion moving from the terminal amine to

being delocalized around the indole ring. The other interesting feature is the slight blue shift of the indole N-H and a blue shift of the O-H stretch when the complex dissociates from the $[\text{Trp}+\text{H}-\text{NH}_3]^+$ to the $[\text{Trp}+\text{H}-\text{NH}_3-\text{CH}_2\text{CO}]^+$ structure. The charge is delocalized over the indole ring and the O-H group of the 146 *m/z* structure. Furthermore, as the carboxylic acid O-H is changed to an alcoholic O-H, the frequency change is reflected in the experimental spectrum; however, a free O-H would be further blue-shifted, and thus supports a delocalized terminal O-H, which was predicted with theory.

IRMPD of the $[\text{Trp}+\text{H}-\text{NH}_3]^+$ Fragment Ion

The experimental spectrum of the $[\text{Trp}+\text{H}-\text{NH}_3]^+$ fragment ion compared to four of the lowest energy conformers is shown in Figure 5-16. The conformers suggested are derived from three possible nucleophilic attacks from carbon atoms denoted C2 (A and B), C3 (C), and C4 (D). The pathways of fragmentation for each nucleophilic attack are illustrated in Figure 5-17.

The conformer that results in the best spectroscopic match is the spirocyclopropane structure (C3), illustrated in Figure 5-16C. The three absorption bands predicted by theory align closely with the bands observed in the IRMPD spectrum. Furthermore, the predicted spectra for the two conformers formed from the C2 attack and the conformer predicted from the C4 attack do not match well with the experimental spectrum. Specifically, the prediction of the N-H indole vibration, which is a useful indication of the delocalization of charge over the aromatic side chain, does not match well with the experimentally detected modes. This result is in agreement with previous work done by Lioe et al.,¹⁸⁹ where they showed the C2 and C4 structures were hindered by high kinetic barriers.

In addition to the theoretical structures shown in Figure 5-16, other candidate structures were also calculated for the $[\text{Trp}+\text{H}-\text{NH}_3]^+$ (*m/z* 188) fragment ion. The benzyl cation structure can be seen in Figure 5-18, compared to the $[\text{Trp}+\text{H}-\text{NH}_3]^+$ experimental spectrum. The conformer was predicted to be significantly lower in energy, $\sim 40 \text{ kJ mol}^{-1}$, than the other conformers resulting from the C2, C3, and C4 nucleophilic attacks. Although the structure is thermodynamically favored, the theoretical spectrum does not match as well as the spectrum calculated for the C3 conformer. Furthermore, the energy of the optimized structure does not reflect the transition-state energy barrier required to generate the fragment ion. The benzyl cation would require a 1,2-hydride shift to form the fragment, which has a large transition state barrier, thus making the formation of this conformer unlikely.¹⁹⁰

IRMPD of the $[\text{Trp}+\text{H}-\text{NH}_3-\text{CH}_2\text{CO}]^+$ Fragment Ion

The ion at *m/z* 188 gave rise to a subsequent neutral loss of 42 amu to produce a fragment ion at *m/z* 146. This loss was assigned as a neutral loss of $-\text{CH}_2\text{CO}$ and resulted in the fragment $[\text{Trp}+\text{H}-\text{NH}_3-\text{CH}_2\text{CO}]^+$. Just as the 188 *m/z* ion was generated through nozzle-skimmer dissociation, the 146 *m/z* ion was generated and stored in the QIT for photodissociation experiments. The IRMPD spectrum recorded for the $[\text{Trp}+\text{H}-\text{NH}_3-\text{CH}_2\text{CO}]^+$ compared with the lowest energy conformers is shown in Figure 5-19. The conformers shown (A-D) are the rotamers of the same structure relative to the C-C and C-O bonds. The higher energy structures result in an improved match between the theoretical and experimental spectra, specifically, the conformer in Figure 5-19D, where the hydroxyl H is directed toward the H on C2. Considering that the conformers are based on rotation, the chance that the structure is kinetically trapped in a higher energy conformer seems unlikely. In general, the trends for the position of the indole N-H and

alcoholic O-H shown for the four conformers are consistent with experimental findings and match the proposed chemical structure $[\text{Trp}+\text{H}-\text{NH}_3-\text{CH}_2\text{CO}]^+$.

Conclusions

Optimization experiments were performed with the OPO laser coupled to the Penning trap of a FT-ICR mass spectrometer to maximize the IRMPD yield. The trapping parameters in the Penning trap were adjusted to squeeze the ion cloud along the z-axis of the trap to increase overlap of the ion cloud with the beam path of the OPO laser and resulted in a 2.5-fold linear gain in IRMPD yield. Furthermore, at optimal trapping conditions, the abundance of fragmentation was measured relative to the irradiation time for the OPO alone and a dual laser approach of the OPO and CO₂ lasers. The boost in IRMPD yield from the second laser was less useful at longer irradiation times, suggesting that the dual laser approach is mainly beneficial in boosting relatively low IRMPD yields at shorter irradiation times.

The IRMPD spectrum of protonated tryptophan, TrpH⁺, was taken on two different mass spectrometers, in a Penning trap and in a QIT of a custom-built mass spectrometer. Results indicated that fragmentation yield was significantly increased in the QIT because of the increase in laser flux on the ion cloud, despite much shorter irradiation times and higher pressures.

Furthermore, the fragment ions of the TrpH⁺ complex, $[\text{Trp}+\text{H}-\text{NH}_3]^+$ and $[\text{Trp}+\text{H}-\text{NH}_3-\text{CH}_2\text{CO}]^+$ were studied with IRMPD spectroscopy to elucidate gas-phase structure and dissociation chemistry. A single conformer, via a C3 carbon attack was confirmed as the 188 *m/z* fragment. In addition, the $[\text{Trp}+\text{H}-\text{NH}_3-\text{CH}_2\text{CO}]^+$ structure was also elucidated based on matching with theory. These experiments demonstrate that IRMPD spectra of covalently bound complexes can now be routinely recorded using low-power

tunable bench top laser, thus allowing the characterization of fragmentation pathways of protonated amino acids and peptides.

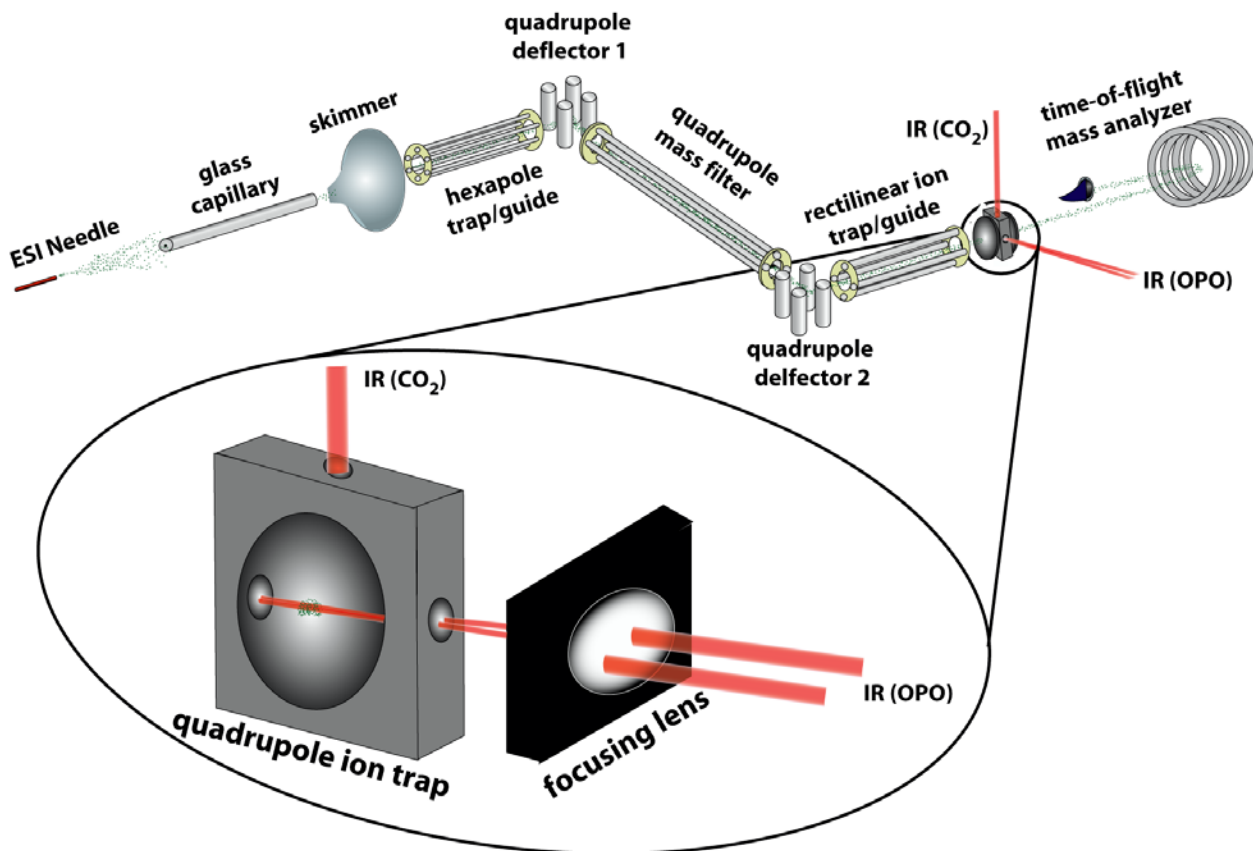


Figure 5-1. Illustration of the OPO and CO₂ lasers tethered to the QIT of a custom built instrument. The two idler beams of the OPO are positioned through a focusing lens to increase the photon flux with the ion cloud. [Adapted with permission from ACS publishing. Mino Jr., W. K.; Gulyuz, K.; Wang, D.; Stedwell, C. N.; Polfer, N. C. Gas-Phase Structure and Dissociation Chemistry of Protonated Tryptophan Elucidated by Infrared Multiple-Photon Dissociation Spectroscopy. *J. Phys. Chem. Lett.* (Volume 2, Pages 299–304)]

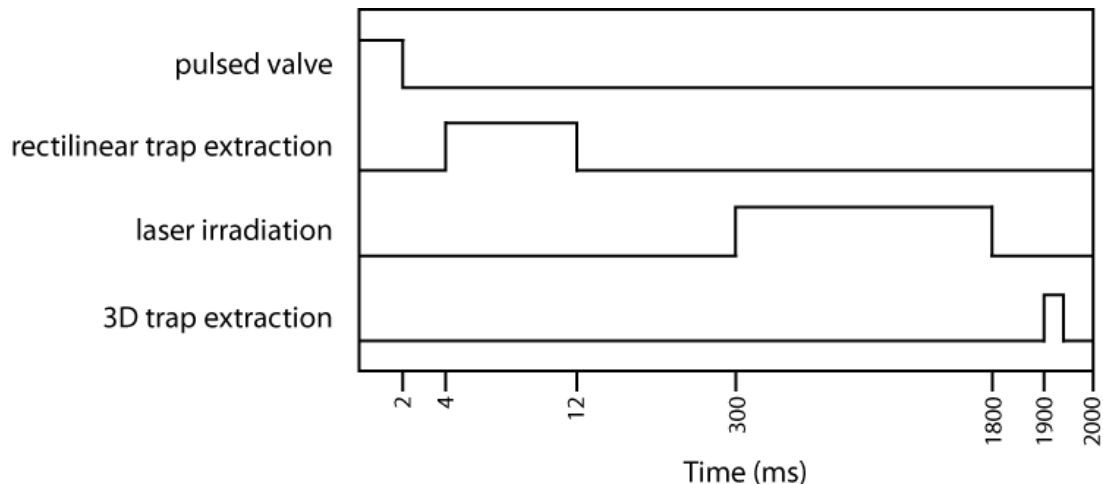


Figure 5-2. Schematic of the timing events used for the IRMPD experiments in the QIT.

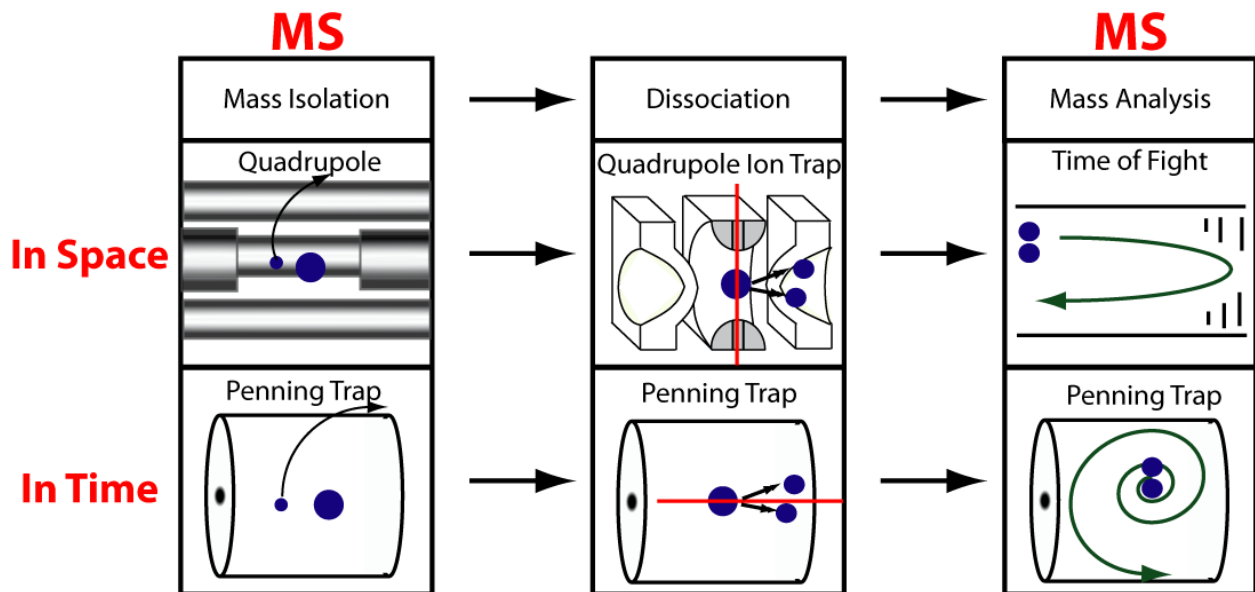


Figure 5-3. Illustration of the mass spectrometric methods for both the custom built and commercial FT-ICR instruments.

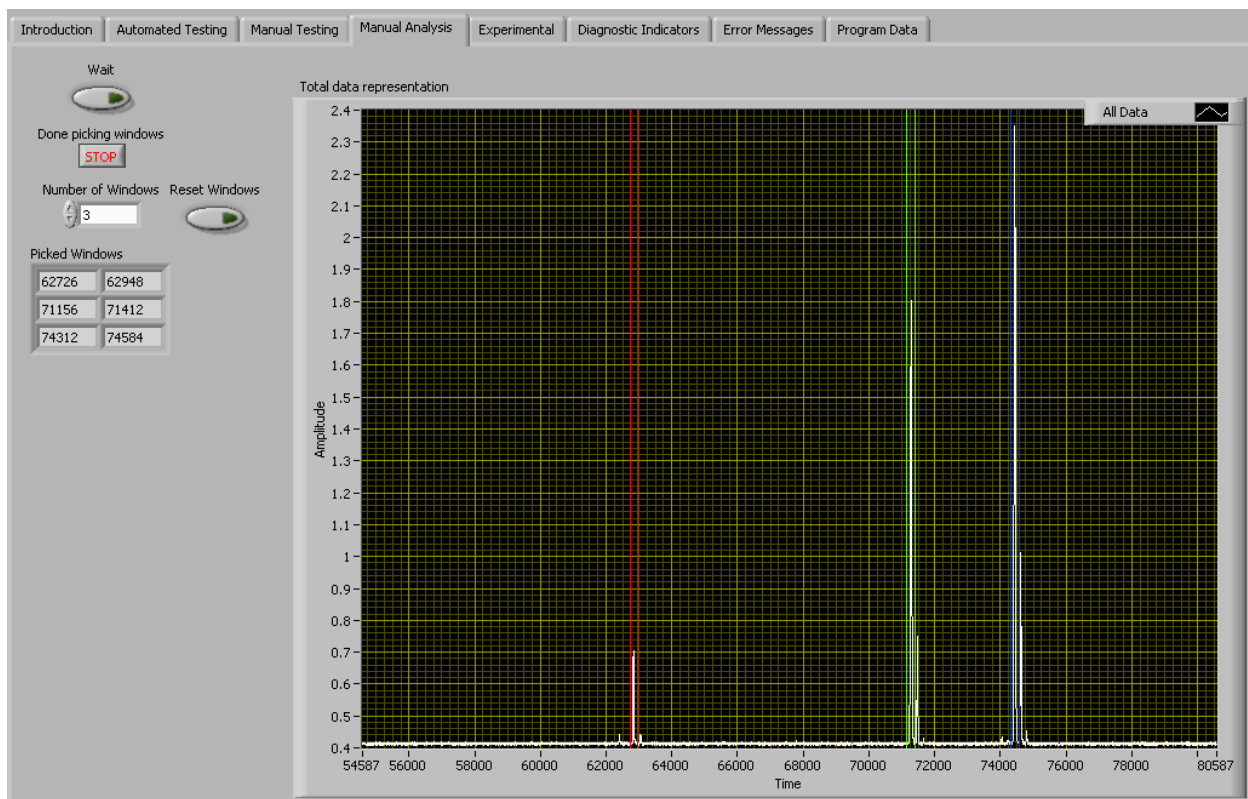


Figure 5-4. Screenshot of the data analysis software built in LabVIEW. .

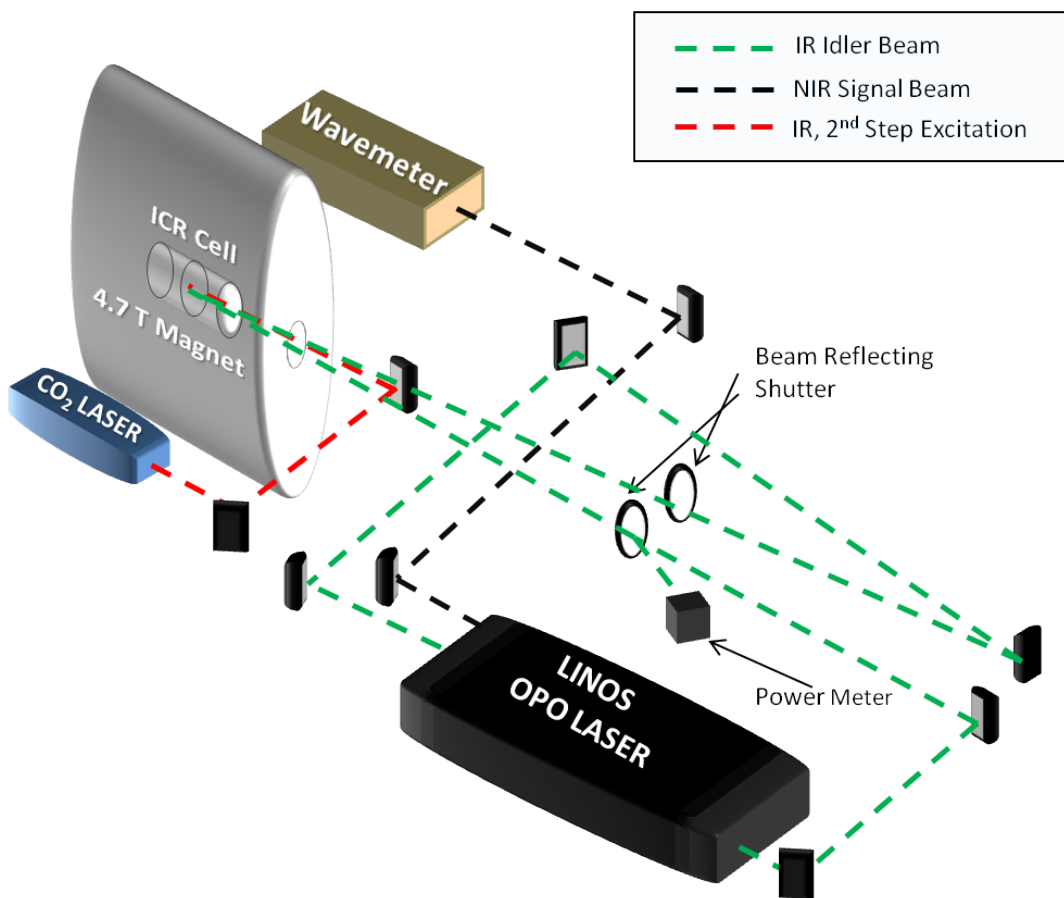


Figure 5-5. Set-up of the OPO and CO₂ lasers tethered to the Penning trap of a FT-ICR mass spectrometer. The two idler beams (green) and the beam from the CO₂ (red) are directed into the trap via steering mirrors. The signal beam (black) of the OPO is directed into the wavemeter. Two beam shutters are used to set the irradiation times in the Penning trap.

Table 5-1. Water cluster absorption bands for the signal and idler beams of the optical parametric oscillator laser.

Signal Wavelength / Nm	Signal Wavenumber / cm ⁻¹	Idler Wavelength / nm	Idler Wavenumber / cm ⁻¹
1715.091	5830.594	2802.768	3567.902
1720.431	5812.497	2788.623	3585.999
1721.231	5809.795	2786.524	3588.701
1723.188	5803.197	2781.410	3595.299
1727.355	5789.198	2770.622	3609.298
1728.341	5785.895	2768.089	3612.601
1729.865	5780.798	2764.188	3617.698
1730.434	5778.897	2762.737	3619.599
1733.043	5770.197	2756.112	3628.299
1733.439	5768.879	2755.112	3629.617
1734.697	5764.696	2751.940	3633.801
1738.859	5750.898	2741.530	3647.599
1739.373	5749.198	2740.253	3649.298
1739.767	5747.896	2739.276	3650.600
1740.009	5747.097	2738.676	3651.400
1741.494	5742.196	2735.005	3656.300
1745.293	5729.697	2725.687	3668.799
1745.872	5727.797	2724.276	3670.699
1747.183	5723.499	2721.090	3674.997
1747.489	5722.497	2720.349	3676.000
1748.528	5719.096	2717.834	3679.400
1751.315	5709.995	2711.128	3688.501
1752.082	5707.495	2709.292	3691.001

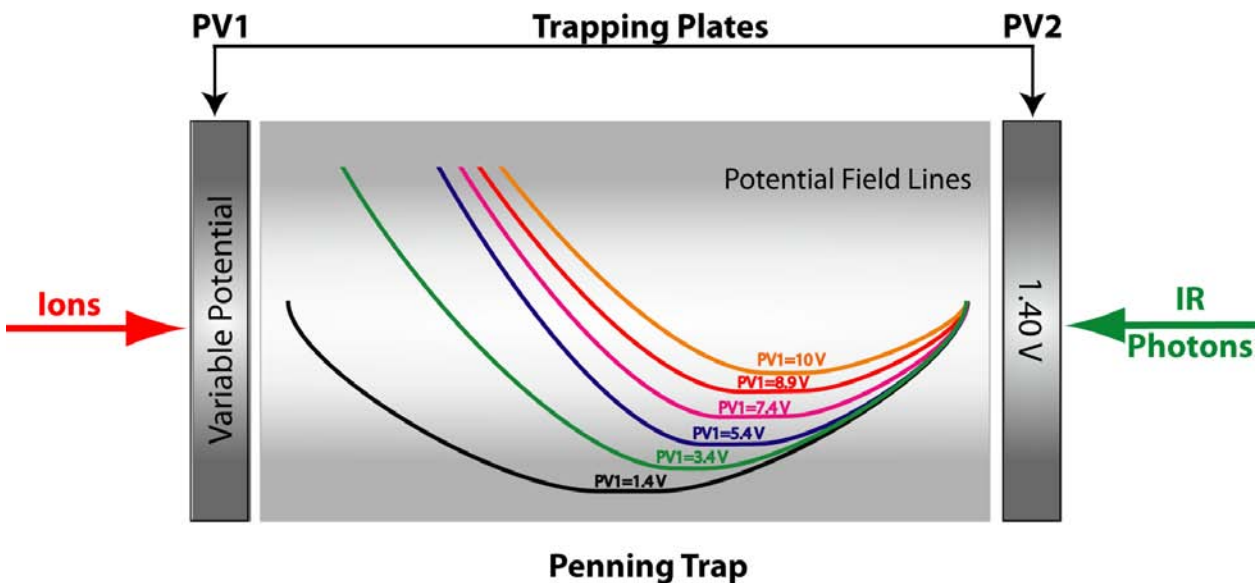


Figure 5-6. Illustration of the effect of changing the trapping voltages on the potential field in the Penning trap. The potential field was simulated with the SIMION software package.

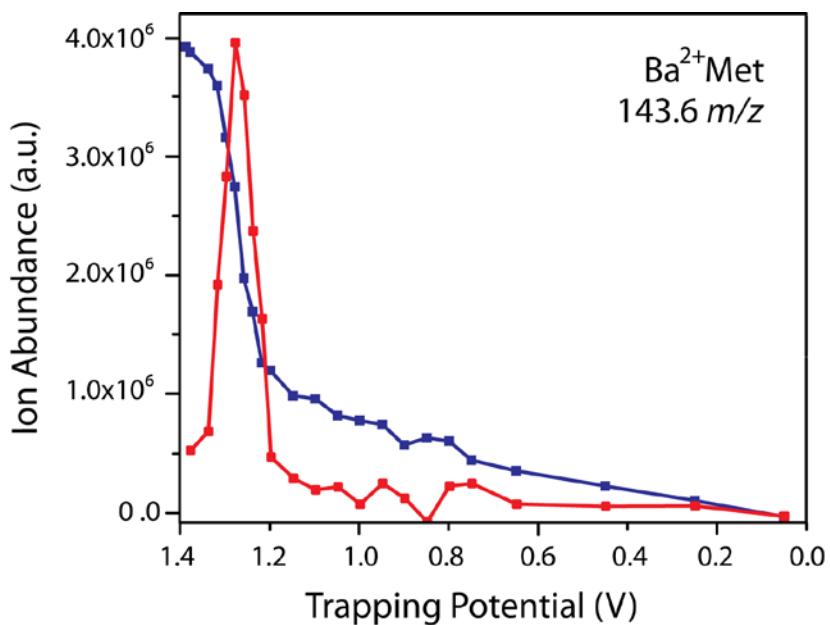


Figure 5-7. Plot of the change in reduced trapping potential versus the measured ion abundance in the Penning trap (blue line). The red shows the derivative $\partial \text{Int} / \partial V$ plot.

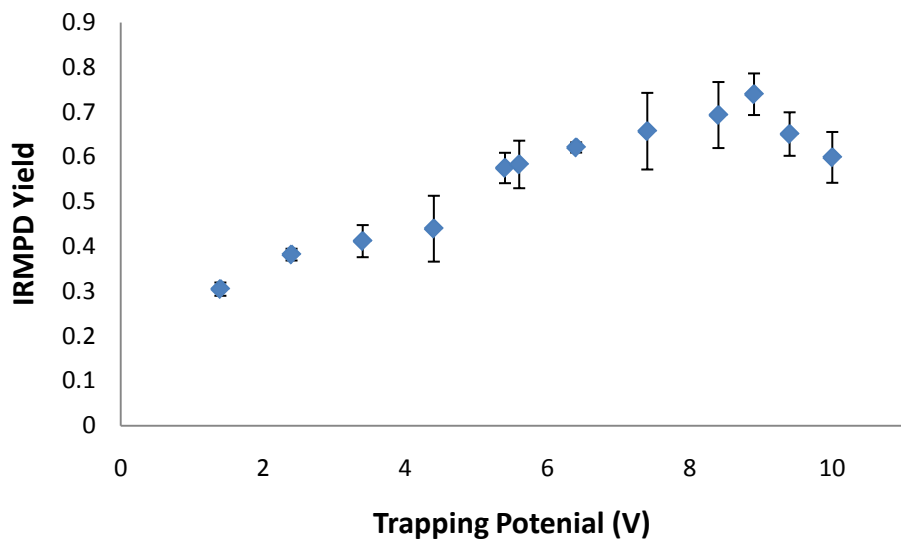


Figure 5-8. A plot of fragmentation yield of the Ba^{2+}Met complex versus the trapping potential applied to the trapping plate PV1 while holding PV2 constant at 1.40V. Irradiation was performed for 10 s with a fixed OPO frequency of 3345 cm^{-1} .

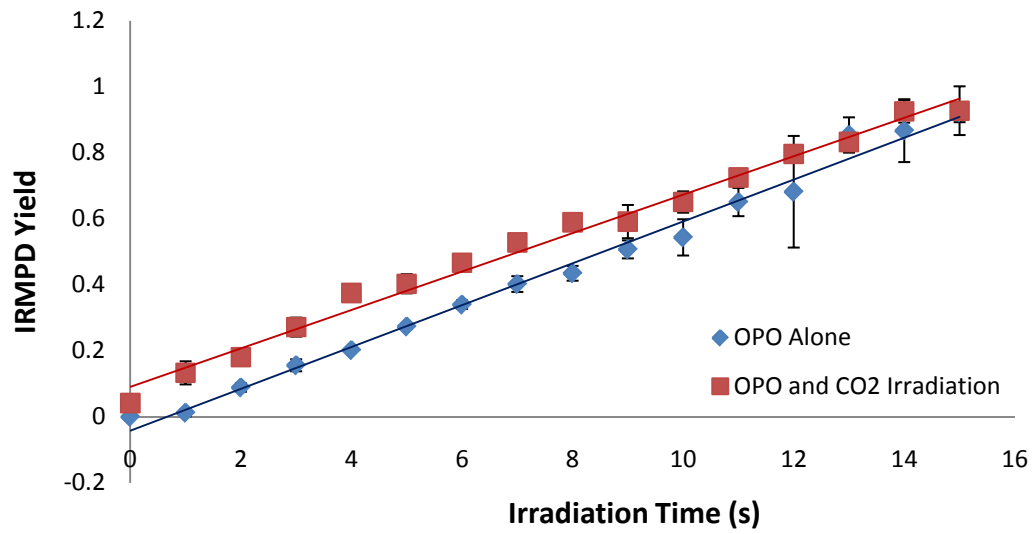


Figure 5-9. A plot of the IRMPD yield of the Ba^{2+}Met complex versus the irradiation time for experiments using the OPO laser alone or using a combination of the OPO and CO₂ lasers. The OPO irradiation was 3345 cm^{-1} .

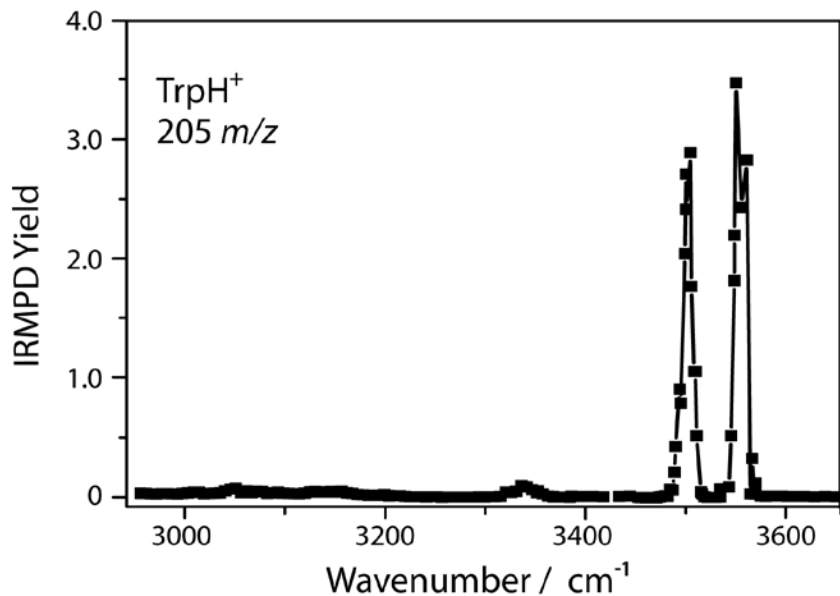


Figure 5-10. The full experimental IRMPD spectrum of TrpH^+ from 2950 cm^{-1} to 3650 cm^{-1} recorded in the Penning trap of the FT-ICR mass spectrometer. The OPO irradiation time was fixed at 10 s and was followed by irradiation with the CO_2 laser for 500 ms.

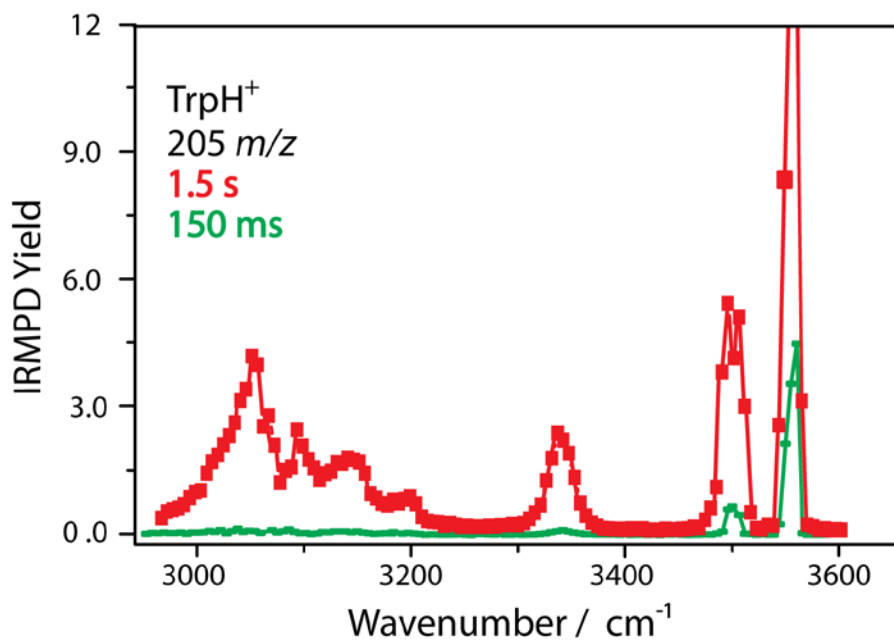


Figure 5-11. The full experimental IRMPD spectrum of TrpH^+ from 2950 cm^{-1} to 3650 cm^{-1} recorded in the QIT of the custom built mass spectrometer. The OPO irradiation time was fixed to 1.5 s (red) and 150 ms (green).

Table 5-2. Summary of centroid band positions and spectral assignments for the experimental IRMPD spectra

band position cm ⁻¹	assignment
TrpH ⁺	
3555	carboxylic acid OH stretch
3500	indole NH stretch
3340	asymmetric NH ₃ ⁺ stretch
3195, 3140, 3090, 3050	NH ₃ ⁺ stretches
[Trp+H-NH ₃] ⁺	
3560	carboxylic acid OH stretch
3425	indole NH stretch
3125	CH stretch
[Trp+H-NH ₃ -CH ₂ CO] ⁺	
3600	OH stretch
3440	indole NH stretch

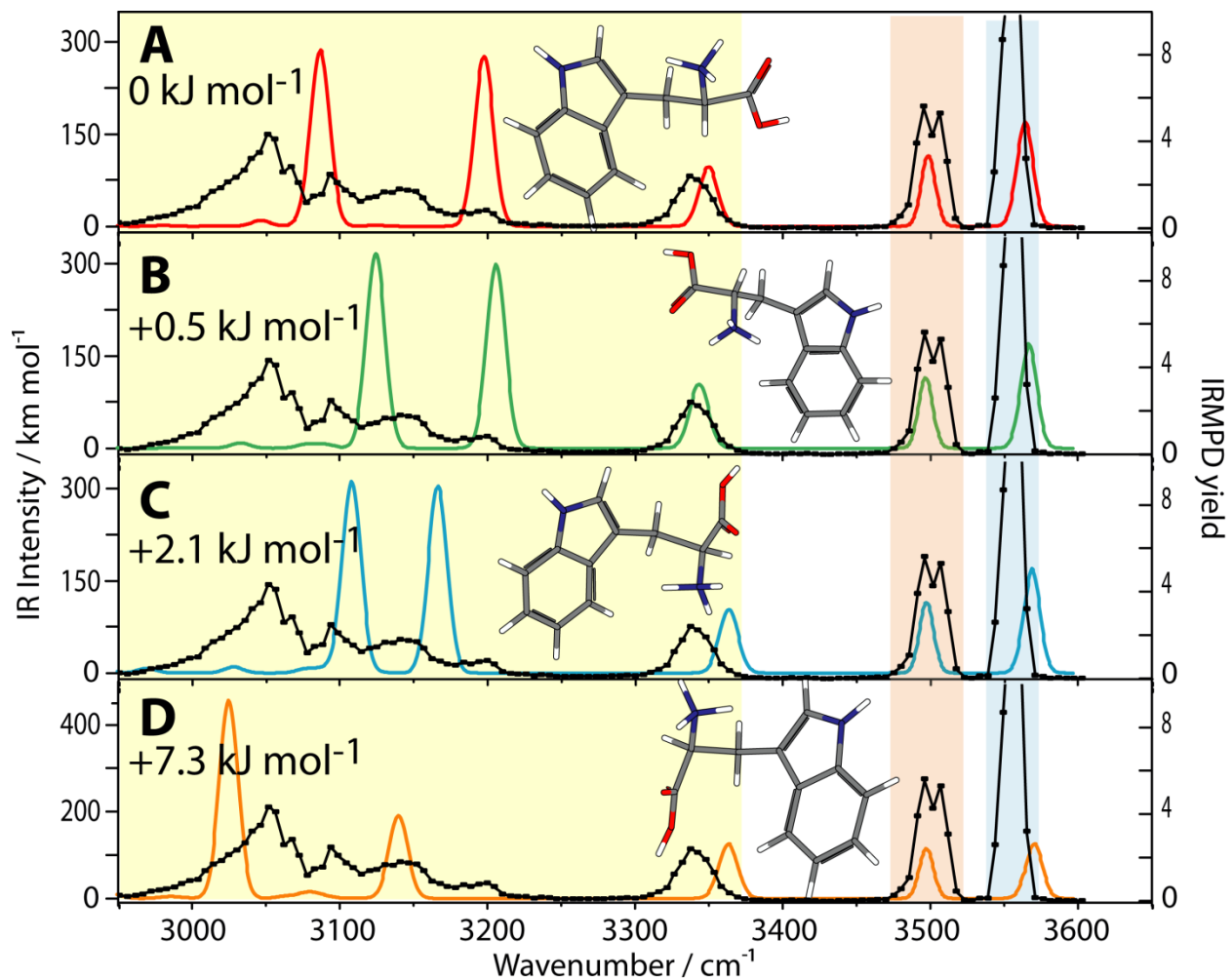


Figure 5-12. Experimental IRMPD spectrum of TrpH^+ (m/z 205) recorded in the QIT (black) compared computational spectra (colors) of four lowest energy conformers (A–D). [Taken with permission from ACS publishing. Mino Jr., W. K.; Gulyuz, K.; Wang, D.; Stedwell, C. N.; Polfer, N. C. Gas-Phase Structure and Dissociation Chemistry of Protonated Tryptophan Elucidated by Infrared Multiple-Photon Dissociation Spectroscopy. *J. Phys. Chem. Lett.* (Volume 2, Pages 299–304)]

Table 5-3. Electronic, zero-point corrected and Gibbs free energies calculated by density functional theory.

	B3LYP			m052x			MP2		
	Hartrees	ZPE kj mol-1	GFE kj mol-1	Hartrees	ZPE kj mol-1	GFE kj mol-1	Hartrees	ZPE kj mol-1	GFE kj mol-1
TrpH⁺									
Fig 5-12									
A	-686.76174	0.000	0.000	-686.68491	2.765	0.627	-682.56524	4.012	3.355
B	-686.76170	0.536	0.536	-686.68443	1.405	3.880	-682.56500	2.045	2.024
C	-686.76097	2.114	2.114	-686.68620	0.000	0.000	-682.56420	0.000	0.000
D	-686.75890	7.341	7.341	-686.68252	8.845	7.848	-682.56080	7.073	13.503
Fig 5-13									
A	-686.76174	0.000	0.000	-686.68491	2.765	0.627	-682.56524	4.012	3.355
B	-686.75379	20.426	20.426	-686.67804	21.177	20.702	-682.55584	17.588	23.422
C	-686.75075	28.274	27.219	-686.67280	34.525	31.981	-682.55469	N/A	N/A
D	-686.75024	29.734	29.734	-686.67360	32.244	31.104	-682.55435	N/A	N/A
TrpH⁺ - NH₃									
Fig 5-16									
A	-630.13190	81.782	81.645						
B	-630.15989	9.757	9.848						
C	-630.16351	0.000	0.000						
D	-630.13598	72.561	72.810						
Fig 5-18									
A	-630.17946	-42.491	-46.327						
B	-630.17822	-40.385	-46.311						
TrpH⁺ -NH₃ - CH₂CO									
Fig 5-19									
A	-477.52127	0.000	0.000	-477.46255	0.000	0.000			
B	-477.51846	6.664	6.364	-477.45994	7.126	7.273			
C	-477.51690	10.788	10.056	-477.45841	10.691	9.930			
D	-477.51198	23.370	22.816	-477.45841	24.601	24.349			

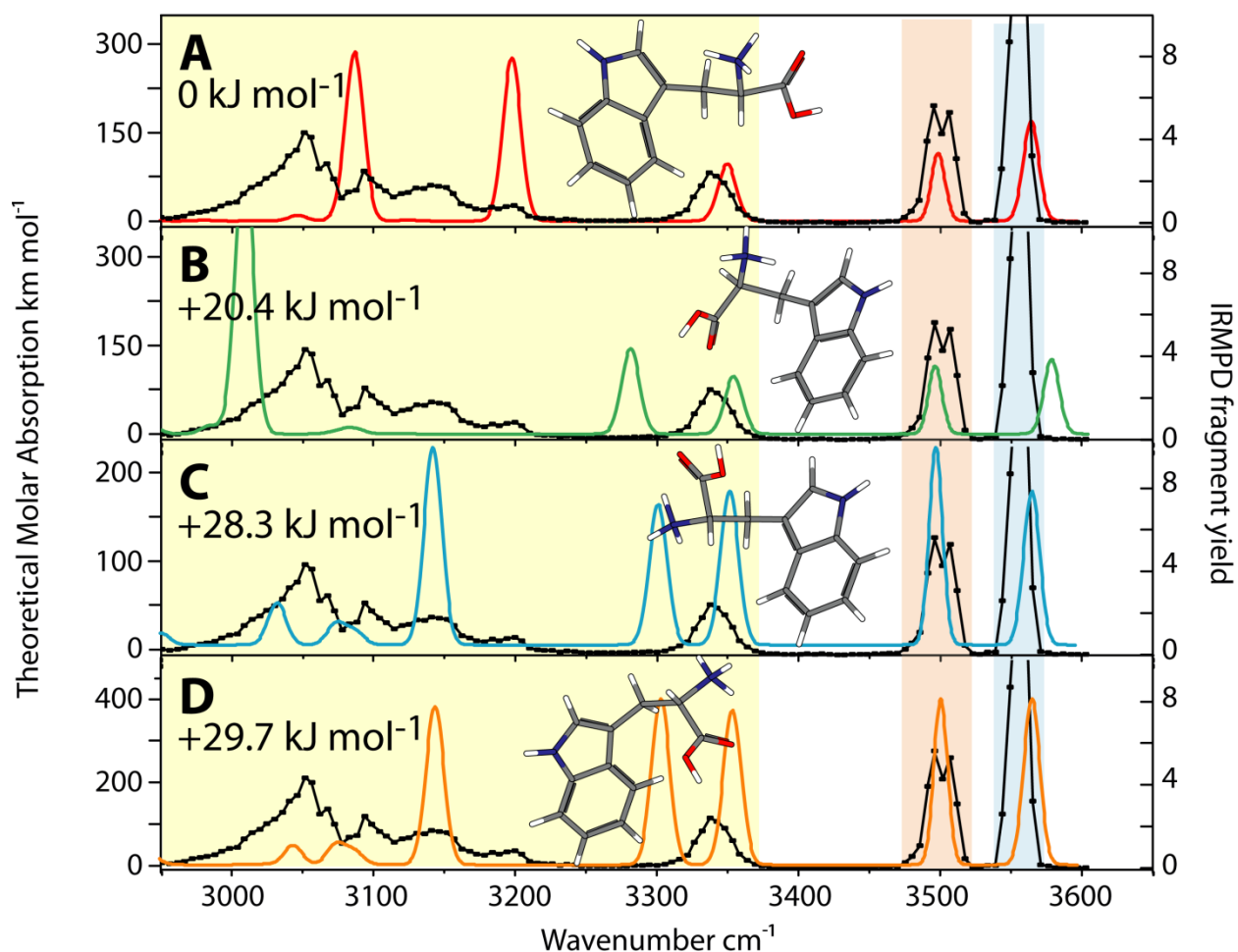


Figure 5-13. Experimental IRMPD spectrum of TrpH^+ (m/z 205) recorded in the QIT (black) compared computational spectra (colors) of the lowest energy conformer and three other low energy conformers (A–D). [Taken with permission from ACS publishing. Mino Jr., W. K.; Gulyuz, K.; Wang, D.; Stedwell, C. N.; Polfer, N. C. Gas-Phase Structure and Dissociation Chemistry of Protonated Tryptophan Elucidated by Infrared Multiple-Photon Dissociation Spectroscopy. *J. Phys. Chem. Lett.* (Volume 2, Pages 299–304)]

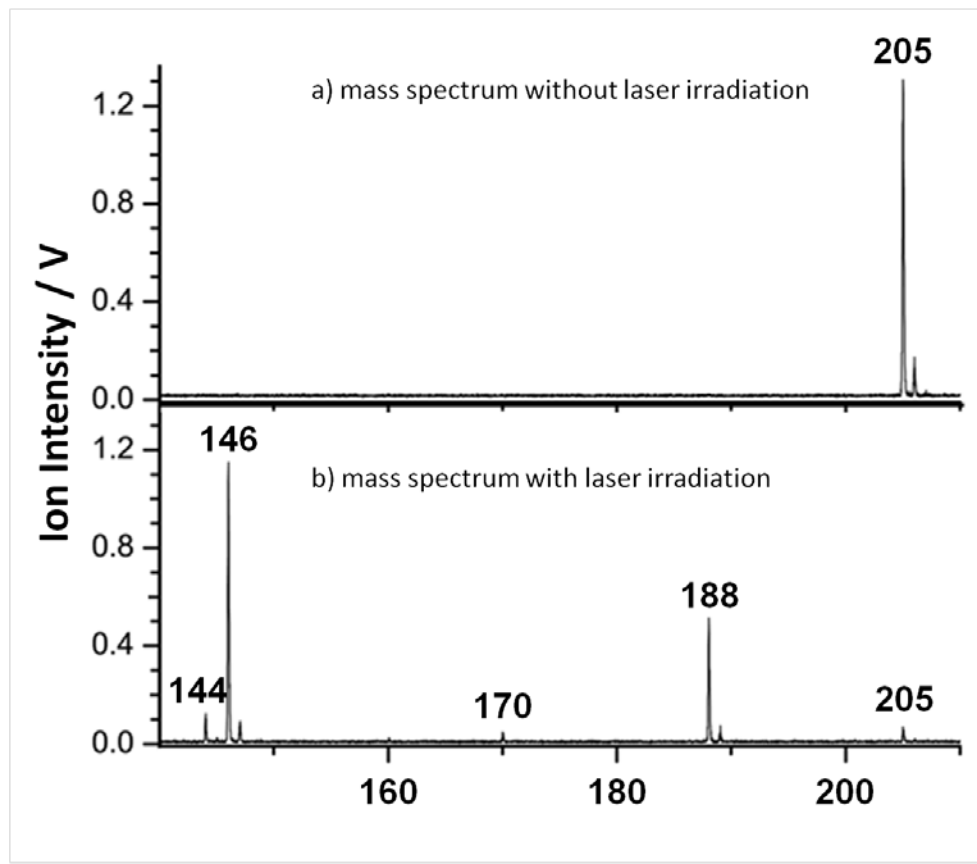


Figure 5-14. The mass spectrum of TrpH^+ (a) without and (b) with laser irradiation. The precursor TrpH^+ ion at m/z 205 is photodissociated to $[\text{Trp}+\text{H}-\text{NH}_3]^+$ at m/z 188, $[\text{Trp}+\text{H}-\text{NH}_3-\text{H}_2\text{O}]^+$ at m/z 170, $[\text{Trp}+\text{H}-\text{NH}_3-\text{CH}_2\text{CO}]^+$ at m/z 146 and $[\text{Trp}+\text{H}-\text{NH}_3-\text{HCOOH}]^+$ at m/z 144.

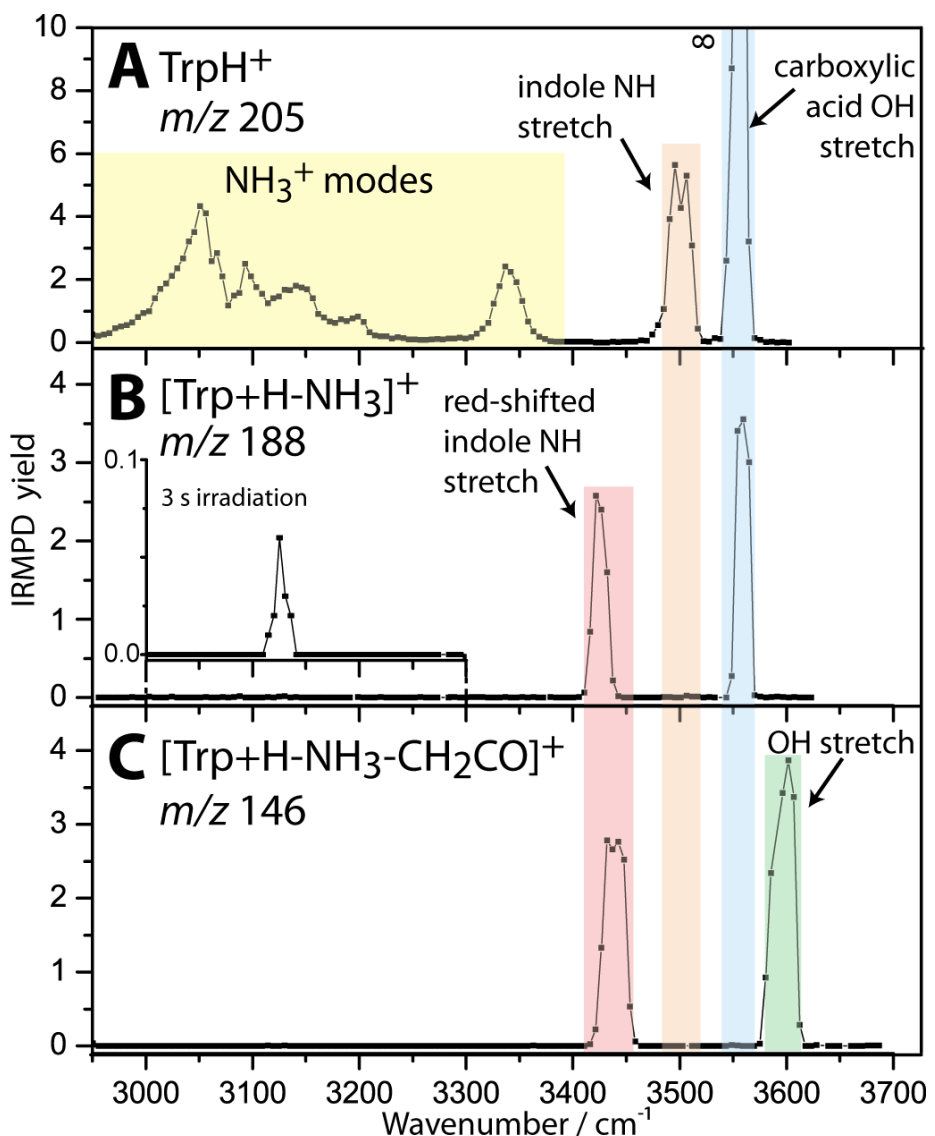


Figure 5-15. Experimental IRMPD spectra of (A) \mathbf{TrpH}^+ (m/z 205), (B) $[\mathbf{Trp}+\mathbf{H}-\mathbf{NH}_3]^+$ (m/z 188), and (C) $[\mathbf{Trp}+\mathbf{H}-\mathbf{NH}_3-\mathbf{CH}_2\mathbf{CO}]^+$ (m/z 146). The vibrational modes are assigned and color-coded. Each spectra was recorded using an irradiation time of 1.5 s, except for the inset in B, the region from 3000 cm^{-1} to 3300 cm^{-1} was recorded using an irradiation time of 3 s. [Taken with permission from ACS publishing. Mino Jr., W. K.; Gulyuz, K.; Wang, D.; Stedwell, C. N.; Polfer, N. C. Gas-Phase Structure and Dissociation Chemistry of Protonated Tryptophan Elucidated by Infrared Multiple-Photon Dissociation Spectroscopy. *J. Phys. Chem. Lett.* (Volume 2, Pages 299–304)]

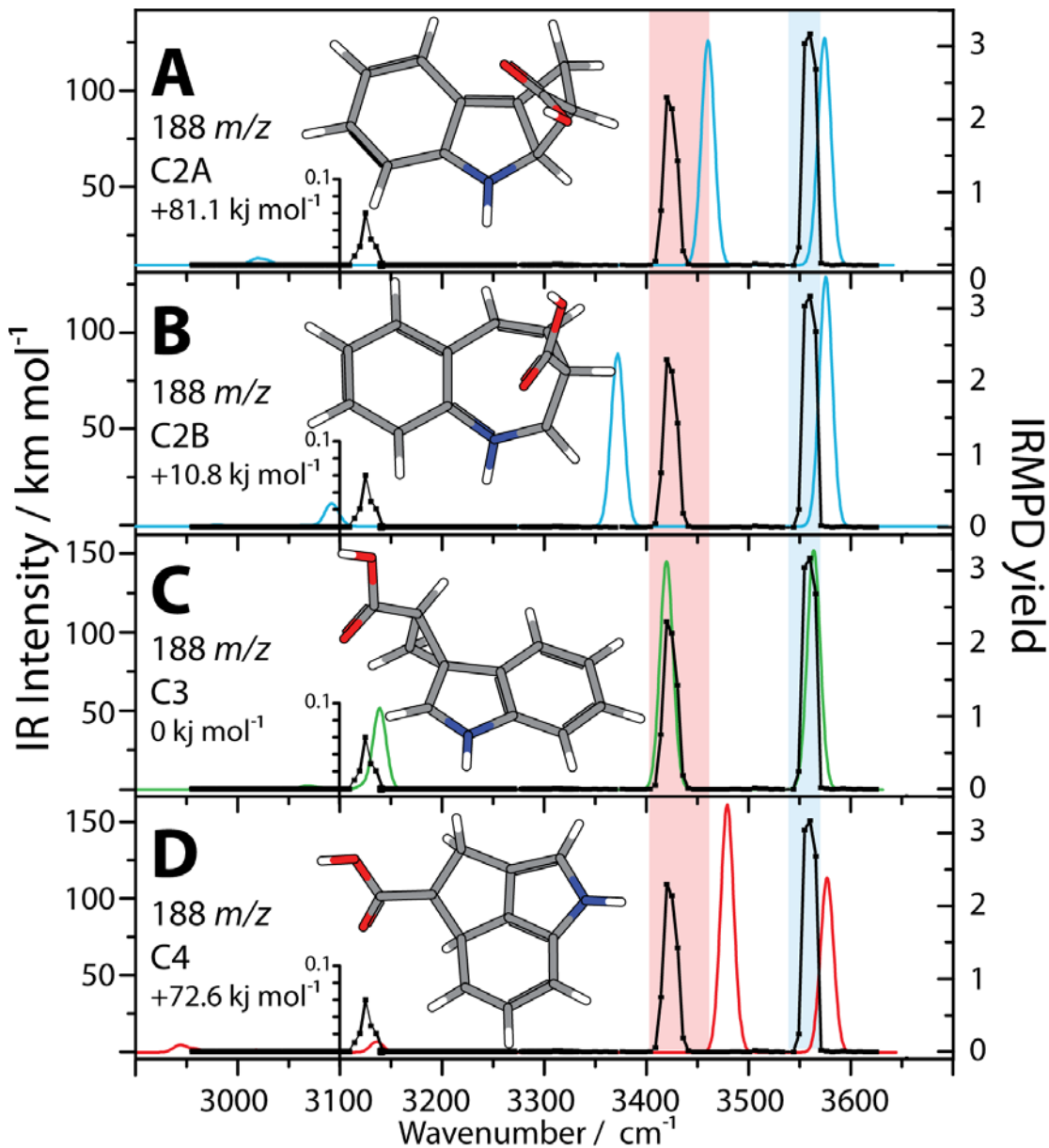


Figure 5-16. Experimental IRMPD spectrum of $[\text{Trp}+\text{H}-\text{NH}_3]^+$ (m/z 188) (in black) compared to the computational spectra of the lowest energy structural conformers (A) C2A, (B) C2B, (C) C3, and (D) C4. The fragmentation pathways can be seen in Figure 5-11. Note that the band at 3125 cm^{-1} in the experimental spectrum is on a different IRMPD scale. [Taken with permission from ACS publishing. Mino Jr., W. K.; Gulyuz, K.; Wang, D.; Stedwell, C. N.; Polfer, N. C. Gas-Phase Structure and Dissociation Chemistry of Protonated Tryptophan Elucidated by Infrared Multiple-Photon Dissociation Spectroscopy. *J. Phys. Chem. Lett.* (Volume 2, Pages 299–304)]

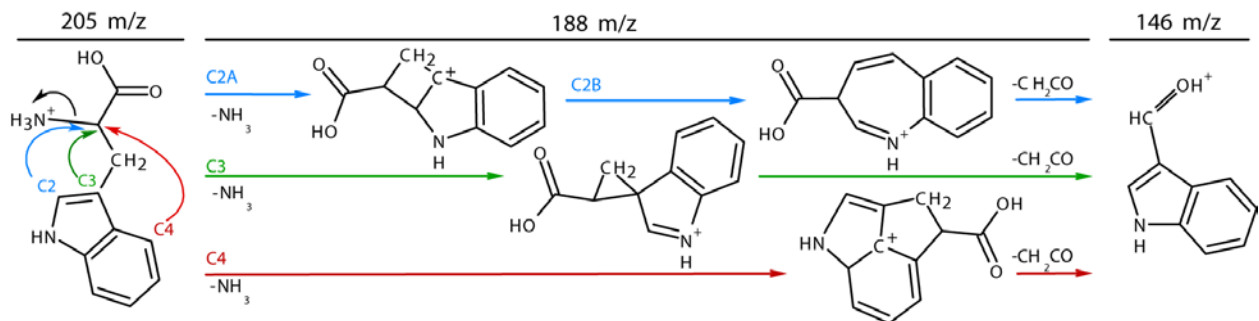


Figure 5-17. Schematic representation of suggested dissociation pathways for NL of NH_3 from the precursor TrpH^+ ion (m/z 205 \rightarrow m/z 188). Nucleophilic attack is shown from the C2, C3 or C4 carbons. For the case of C2, the initial structure (C2A) was proposed to isomerize to a lower energy structure (C2B). Subsequent CH_2CO loss results in a proposed ion (m/z 146). [Taken with permission from ACS publishing. Mino Jr., W. K.; Gulyuz, K.; Wang, D.; Stedwell, C. N.; Polfer, N. C. Gas-Phase Structure and Dissociation Chemistry of Protonated Tryptophan Elucidated by Infrared Multiple-Photon Dissociation Spectroscopy. *J. Phys. Chem. Lett.* (Volume 2, Pages 299–304)]

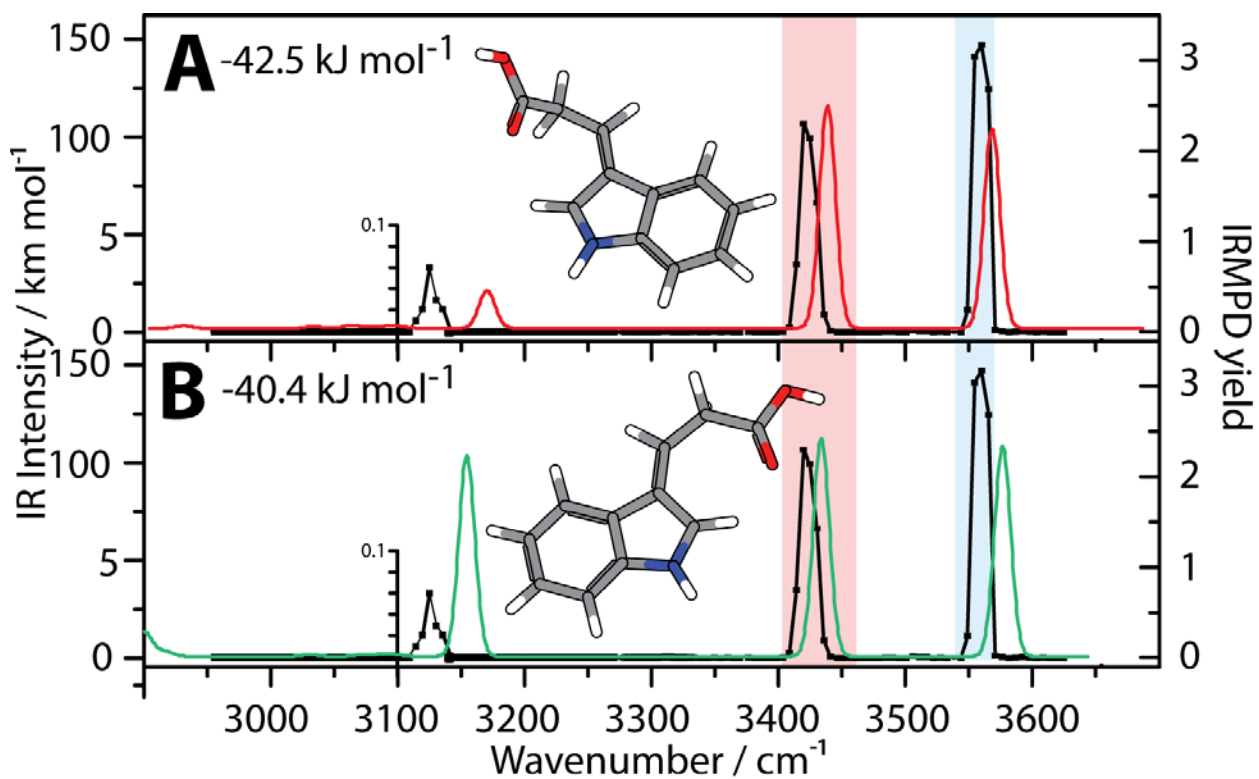


Figure 5-18. Experimental IRMPD spectrum of $[\text{Trp}+\text{H}-\text{NH}_3]^+$ (m/z 188) (in black) compared to the computational spectra of the lowest energy structure predicted by theory. [Taken with permission from ACS publishing. Mino Jr., W. K.; Gulyuz, K.; Wang, D.; Stedwell, C. N.; Polfer, N. C. Gas-Phase Structure and Dissociation Chemistry of Protonated Tryptophan Elucidated by Infrared Multiple-Photon Dissociation Spectroscopy. *J. Phys. Chem. Lett.* (Volume 2, Pages 299–304)]

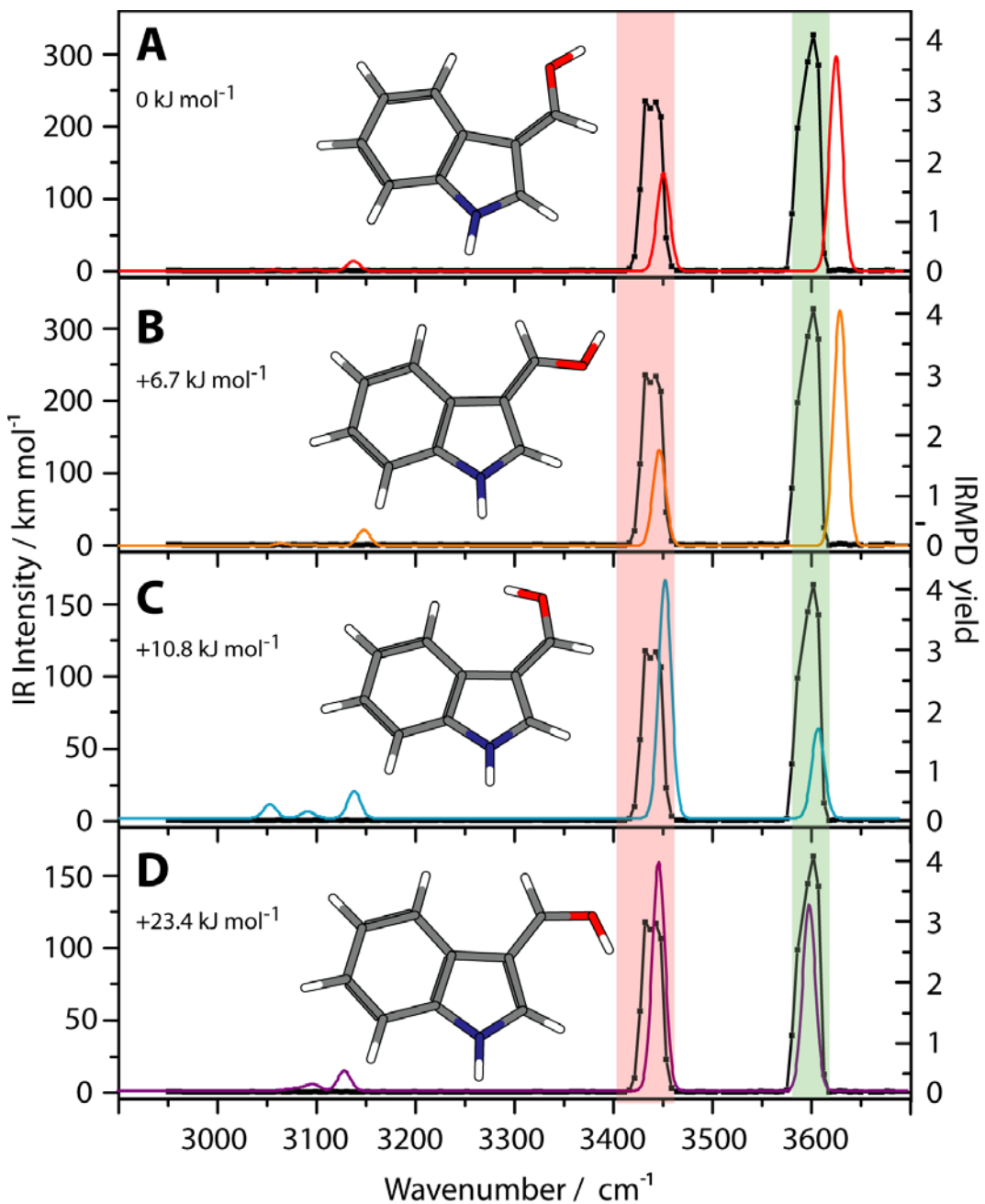


Figure 5-19. Experimental IRMPD spectrum of $[\text{Trp}+\text{H}-\text{NH}_3^+-\text{CH}_2\text{CO}]^+$ (m/z 146) (in black) compared to the computational spectra of the lowest energy rotational conformers. [Taken with permission from ACS publishing. Mino Jr., W. K.; Gulyuz, K.; Wang, D.; Stedwell, C. N.; Polfer, N. C. Gas-Phase Structure and Dissociation Chemistry of Protonated Tryptophan Elucidated by Infrared Multiple-Photon Dissociation Spectroscopy. *J. Phys. Chem. Lett.* (Volume 2, Pages 299–304)]

CHAPTER 6

STRUCTURAL ELUCIDATION OF METAL-TAGGED PEPTIDES VIA LOW-ENERGY RESONANT COLLISION-INDUCED DISSOCIATION

Introduction

In Chapters 3 and 4, it was shown that metal adduction affects the chemical structures of amino acids, and that charge solvated and zwitterionic structures could be distinguished. In the work reported in this chapter the fragmentation chemistry of metal-adducted peptides was studied in a custom-built multiple-quadrupole time-of-flight mass spectrometer (mQ-ToF-MS).¹⁹¹ The ions are fragmented by collision-induced dissociation (CID) which is a “slow” heating technique, as is IRMPD.

Slow Heating Techniques

Tandem MS is an essential tool for structural characterization. Tandem MS incorporates dissociation techniques, which can be classified as either selective or nonselective. For selective dissociation, the precursor ion is targeted, thus no additional energy is supplied to the fragment ions. Sustained off-resonance irradiation (SORI)¹⁹² and on-resonance CID in ion cyclotron resonance (ICR) cells¹⁹³ are examples of such selective methods. On the other hand, nonselective techniques excite the precursor ion as well as primary fragment ions. Infrared multiple photon dissociation (IRMPD) and its variations,^{194,195} as well as blackbody infrared dissociation (BIRD) are nonselective techniques.¹⁹⁶ Both selective and nonselective techniques fall under the *slow heating* category. These methods are termed *slow heating* because the time scale of energy activation is slow compared to the time scaled dissociation. Collisions involve a static target^{6,197-201} or with a mobile target, such as an inert gas.²⁰²

Multiple-resonance CID can be performed as either a selective or nonselective technique.¹⁹¹ In either case the precursor ion is selected in a quadrupole and collided

with background N₂ gas in a succeeding quadrupole. For selective CID, low amplitude excitation is applied to the second quadrupole, resulting in dissociation of the precursor ions and the resulting fragments cooled to the center of the trap (via non-energetic collisions with the background gas). Thus, no secondary fragmentation occurs. For non-selective CID, large excitation amplitudes can be applied to the second quadrupole along with higher q-values. Through energetic collisions with the background gas, the primary fragments formed via CID can undergo secondary fragmentation. Furthermore, the potential applied to the quadrupole can be varied; and the precursor ion can be driven into the second quadrupole with different kinetic energies, resulting in different fragmentation pathways. For the purpose of these experiments, low amplitude, or selective multiple-resonance CID was utilized. Coupled with a ToF mass analyzer, this instrumentation offers high resolving power over a large mass-to-charge (*m/z*) range.

Disulfide Bond Cleavages in Mass Spectrometry

Disulfide bonds play a key role in both defining and stabilizing the secondary and tertiary structure of folded proteins.²⁰¹ An intramolecular disulfide bond between two different cysteine residues is a characteristic of many biologically relevant peptides. These disulfide bond containing peptides are often difficult to sequence using tandem MS. For example, incomplete sequencing of two intramolecular linkages was found via CID in multiply protonated insulin.²⁰³ Only the part of the backbone that does not contain the sulfur-sulfur linkage could be sequenced, which significantly reduced the amount of structural information extracted from the mass spectra.

Recently, Mihalca et. al. coupled SORI-CID with Fourier transform-ion cyclotron resonance mass spectrometry to study the effects of disulfide bond cleavage within

peptides.²⁰⁴ The cleavage efficiency of complexation with different transition metal cations (Zn^{2+} , Cu^{2+} , and Co^{2+}) compared with the protonated peptide was reported.

Oxytocin (OT) was chosen as the peptide for this work due to the characteristic, disulfide bond situated across the cysteine residues located at amino acid positions 1 and 6. For OT, the region of the peptide closed by the disulfide bond is known as the *tocin ring* and the remaining part is labeled as the *tail*. For the purpose of this Chapter, the corresponding regions will be referred to in this way.

Rationale for Experiments

OT is biologically activated by essential elements, such as Zn^{2+} , Cu^{2+} and Fe^{2+} , and has been linked to smooth muscle contractions of the uterus during lactation,²⁰⁵ maternal behavior, infant separation distress,³⁶ and memory storage and learning.²⁰⁵ The presence of a metal ion could alter the peptide conformation, altering receptor binding, and thus changing the function of the peptide. Previous experiments of coupling OT to its receptor showed that Zn^{2+} , Ni^{2+} , and Co^{2+} enhanced binding, but the presence of Cu^{2+} had no effect.²⁰⁶

Experimental

All the experiments were performed on a mQ-ToF-MS in positive ion mode at Analytica of Branford (Branford, CT).^{191,207} A schematic of this instrument is shown in Figure 6-1. Ions were generated via ESI, operated at a flow rate of 0.4 mL/hr and injected directly into the glass capillary of the mass spectrometer. The ESI emitter needle was held at ground (~0 V) and a potential of -2100 V was applied to the capillary. Oxytocin (OT) (Sigma, St. Louis, MO) was dissolved in de-ionized water at an analyte concentration of 200 μ M. The complexes of $Cu(NO_3)_2$, $Zn(NO_3)_2$, $FeCl_2$ and $Fe(NO_3)_3$ (Fisher Chemical, Pittsburgh, PA) were each prepared separately at 1.00 mM

in de-ionized water. The solutions were mixed and diluted in 50:50 water/methanol to a final concentration of 20 μM and 100 μM for OT and the metal ion, respectively. In order to compare differences in fragmentation patterns, OT was dissolved in absence of the metal cation in 50:50 methanol/water with 0.1% acetic acid by volume.

Mass spectra displayed a prominent peak for two different types of precursor ions. A doubly charged peptide-metal complex $[\text{OT+Me}]^{2+}$ and a singly charge peptide-metal complex $[\text{OT+Me-2H}]^+$, were detected for the Me^{2+} and Me^{3+} , respectively. These precursor peptide-metal complexes were isolated in the first analytical quadrupole (AQ), where the pressure was maintained around 5×10^{-5} Torr. Once the precursor ion was selected, it was then moved to the collisional quadrupole (CQ), where the pressure was maintained at approximately 10^{-2} Torr. Axial translational energy moved the precursor ions from the AQ to the CQ. Based on the offset voltage applied to precursor ions, the ions are accelerated into the CQ where they collide with the background, N_2 , gas, which led to dissociation. The fragments were then analyzed by the ToF mass analyzer with a linear reflectron and detected with a microchannel plate. The ToF-MS data were collected and monitored using software provided by Analytica of Branford.²⁰⁸

Results and Discussion

Nomenclature

Roepstorff-Fohlman-Biemann nomenclature is utilized to identify the peptide fragments.^{209,210,25} Briefly, backbone cleavages observed with the charge residing at the N-terminus are labeled as **a**, **b** or **c** fragments; if the charge resides on the C-terminus, the fragmentation is denoted as an **x**, **y**, or **z** fragment. Figure 6-2 illustrates typical fragmentation paths and naming schemes.

For the fragmentation of the peptide between residues 1 and 6, the *tocin ring*, the disulfide bond between the two cysteine groups must be cleaved. The most common cleavage is across the sulfur-sulfur bond; however, it is possible to cleave the sulfur-carbon (S-C) bond of the cysteine groups. S-C bond cleavage leads to fragments that either have a single sulfur loss or an extra sulfur attached and are referred to as –S and +S, respectively.

After isolation of the metalated OT, the fragments show that the metal ion is typically still attached, and it will be noted when this is not the case. Finally, internal loss by multiple cleavage of the precursor ion backbone is labeled with the three letter code of the amino acid/s lost.

Product Ions From CID Spectra

Multiple resonance excitation CID tandem mass spectra of OT complexed with 2H^+ , Cu^{2+} , Zn^{2+} , Fe^{2+} and Fe^{+3} are shown in Figure 6-3, Figure 6-4, Figure 6-5, Figure 6-6, and Figure 6-7 respectively. As depicted in Figure 6-8, the four types of product ions of the aforementioned spectra will be discussed. The first type is a result of single, or multiple, neutral loss(es) (NL) from the precursor ion, typically NH_3 , CO, or H_2O are seen as NLs. The second type is **b/y** fragmentation of the tail; this cleavage does not require a break in the *tocin ring*. The third type is **b/y** fragments within the *tocin ring*. In this case, to see these fragments, not only must a backbone cleavage occur, but the disulfide bond must also be cleaved. The fourth fragmentation pathway is through internal loss. This fragmentation requires at least two bond cleavages; however, instead of one backbone and one disulfide cleavage as mentioned in type 3, both breaks occur on the backbone. Note that the pathway type does not indicate the order of

fragmentation. For example, to see y_4 -CO fragments, the peptide backbone could cleave first, leading to the y_4 fragment, followed by a NL of CO, or *vice versa*.

In Table 6-1, the identified product ions are organized into their appropriate fragmentation pathway (type 1–4). The intensity values for the product ion fragments are a summation of all isotopic peaks associated with that fragment. For Cu^{2+} , Fe^{2+} and Fe^{3+} complexed peptides, at least three isotopic peaks were summed together as the total ion signal. For the case of Zn^{2+} , at least four isotopic peaks were utilized. Thus, the product ion intensity relative to the total intensity of the spectra was obtained. The relative intensities for each of the fragmentation pathways are also depicted in Table 6-1.

Neutral loss from the precursor ion (1)

Neutral loss (NL) of NH_3 , CO, and H_2O is observed in all four OT-metal spectra (type 1 fragments in Table 6-1). However, the relative abundance of each NL varies from metal to metal, and for the case of Fe^{2+} and Fe^{3+} , the relative abundance also varied between the two different charge states. The most abundant NL from the precursor ion was observed for the $[\text{OT}+\text{Cu}^{2+}]^{2+}$ complex, and the least abundant NL was seen for $[\text{OT}+\text{Zn}^{2+}]^{2+}$. Furthermore, NL was also seen from product ions of type 2, 3 and 4. The b/y fragments with a NL make up about 25% of the total ion intensity of the other three types, but these fragments remain characterized as b/y fragments in Table 6-1. Another NL that occurred was the loss of the disulfide bridge in the MS/MS spectra of $[\text{OT}+\text{Fe}^{3+}-2\text{H}]^+$. Only the triply charged metal was able to cleave the disulfide bridge in its entirety. Although this is classified as a NL, the detail of this cleavage is discussed further in the ‘Cleavage of the Disulfide Bridge (3)’ section.

Fragmentation from the peptide backbone tail (2)

Fragmentation of the backbone through **b/y** cleavage of the tail ranged from 30% of the total production ion intensity in $[OT+Cu^{2+}]^{2+}$ and up to 64% of the total ion intensity in $[OT+2H]^{2+}$. The doubly protonated OT had the largest relative intensity of type 2 fragmentation, due to the lack of type 3 cleavage. This was expected since there is little to no cleavage of the disulfide bond without complexation of a metal cation. The observed product ions seen are the **b₆**, **b₇**, **b₈**, and **y₃** fragments. The only two mass spectra that contained all of the tail fragments were from the $[OT+2H]^{2+}$ and the $[OT+Zn^{2+}]^{2+}$ complexes.

The **y₃** fragment was the most intense fragment for all complexes. Its high intensity is attributed to the importance of proline in the destabilization of amino acid sequences. The **b₆** fragment was seen in all five spectra as well, but with lower relative abundance for the metal-complexed OT compared with the doubly protonated OT. Due to the weakened disulfide bridge, across the 1 and 6 cysteines, the metal cation gives more possible fragmentation pathways, lowering the overall intensity of the **b₆** fragment. Moreover, the **y₃** fragment for all species was in the singly charged protonated form. There was no metal found on the **y₃** fragment in any of the spectra. From this observation, it is concluded that the metal cation resides between the 1 and 6 cysteine groups and is interacting with the disulfide bond. In addition, this is in agreement with finding the metal bound on all **b₆** fragments of the metal complexed OT.

Cleavage of the disulfide bridge (3)

Type 3 product ions require a two-step cleavage process. Fragmentation within the *tocin ring* requires disulfide bond (or an S-C bond) cleavage and cleavage along the peptide backbone. From spectra of the four metal complexed ions, **b₂**, **b₄**, **b₅**, **y₅**, **y₇**,

and y_8 fragments were observed, which are indicative of disulfide bond cleavage. A lack of type 3 ions show that the *tocin ring* remains intact for the doubly protonated OT; this trend can be seen in Table 6-1. These results are in agreement with previous studies,^{204,203} where the disulfide bridge was shown to be responsible for incomplete peptide sequencing via MS/MS. Upon the addition of a metal cation, the disulfide bond can be broken through MS/MS leading to more coverage of the peptide sequence.

Another interesting result is the comparison of the Fe^{2+} and Fe^{3+} metal complexed OT fragmentation spectra. Although Fe^{3+} displayed less fragmentation than its Fe^{2+} counterpart, Fe^{3+} was the only metal that produced a NL of H_2S_2 . This loss was not only observed for the precursor ion, but was observed in the b_6 fragment as well. While loss of H_2S was observed for several of the product ions (b_4 , b_5 and y_8) for Cu^{2+} Zn^{2+} and Fe^{2+} , this only shows that a single (S-C) bond on a cysteine was cleaved, not both.

It is also important to note that the total intensity for the product ions from Fe^{3+} was much lower compared to the three other divalent metal cations. This trend is depicted in Table 6-2. The structure and biological activity of OT has been shown to change based on interactions with different metal cations.²⁰⁶ Although we can only hypothesize as to why the complexation of Fe^{3+} causes the loss of H_2S_2 , it is possible that the greater charge and stronger binding of the metal stabilize the complex and OT no longer needs the disulfide bridge to retain structure.

Loss of internal amino acids through b/y fragmentation (4)

The loss of internal amino acids is a result of a double cleavage along the peptide backbone. Typically, internal loss occurs when the disulfide bond is not cleaved. These fragments are seen in the $[\text{OT}+\text{Zn}^{2+}]^{2+}$ and $[\text{OT}+\text{Cu}^{2+}]^{2+}$ spectra, in the form of [OT-Tyr], [OT-Tyr-Gly] and [OT-Tyr-CO] and [b_8 -Tyr]. The loss of the Tyr fragment indicates that

the disulfide bond was not successfully cleaved; however, these internal fragments are not seen unless a metal ion is attached. No type 4 fragments were detected for the $[OT+Fe^{3+}-2H]^+$ spectra. Conceivably, the trivalent complexed metal and the loss of two hydrogens significantly alter the secondary structure of OT and an internal loss is not possible due to structural changes. However, to confirm this other trivalent metals must be studied.

Conclusions

Sequencing of peptides containing disulfide bridges was achieved via multiple-resonance CID. Complexation of transition metal ions lead to four types of fragmentation pathways. The first type, NL accounted for 8 % ($[OT+Zn^{2+}]^{2+}$) to 33 % ($[OT+Fe^{3+}-2H]^+$) of the total product ion intensity. Typically, NL resulted from H_2O , NH_3 and CO ; however, the $[OT-Fe^{3+}-2H]^+$ was the only complex to show a NL of H_2S_2 . The second type, fragmentation of the tail region, ranged from 30 % ($[OT+Fe^{2+}]^{2+}$) to 62 % ($[OT+2H]^{2+}$) of the total ion intensity. For the metal-complexed OT, the b_6/y_3 ion pair suggested that the metal was bound to the *tocin ring*. The third type, fragmentation of the *tocin ring*, was only seen for OT complexed with a metal ion. The total ion intensity ranged from 0 % ($[OT+2H]^{2+}$) to 48 % ($[OT+Fe^{2+}]^{2+}$). The fourth type, internal loss, was seen in all of the OT spectra except for the $[OT+Fe^{3+}-2H]^+$. Internal loss was 0 % ($[OT+Fe^{3+}-2H]^+$) through 17 % ($[OT+Cu^{2+}]^{2+}$) of the total ion intensity; however, the lack of internal loss seen for the $[OT+Fe^{3+}-2H]^+$ complex was unexpected.

The dissociation of metal-chelated peptides was shown to be useful in obtaining sequence information on disulfide-bridged peptides; however, the exact nature of metal cation interaction in these systems is not known. Thus, IRMPD spectroscopy of smaller

disulfide-bound peptides could give structural insights into the binding and dissociation pathways of metal bound peptides, which cannot be elucidated from tandem MS alone.

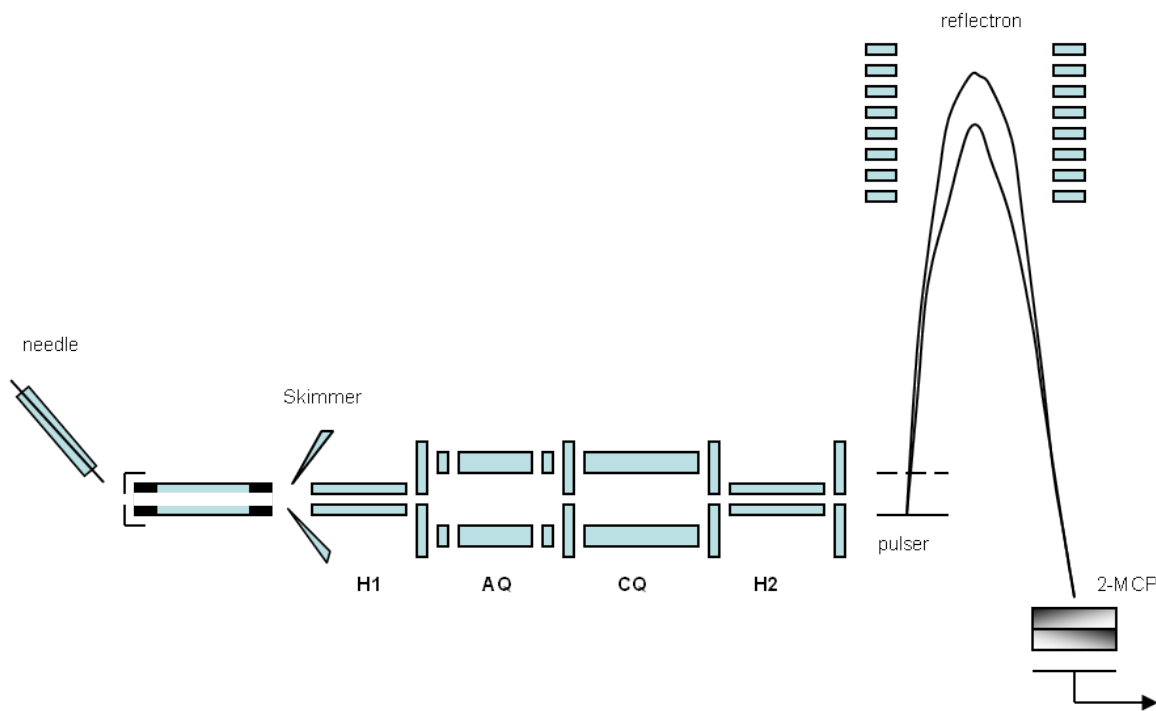


Figure 6-1. Illustration of a multiple-quadrupole ToF-MS instrument. The ESI source is equipped with a spray needle, glass capillary, and a sample skimmer. The ion guide is composed of a front hexapole (H1), followed by an analytical quadrupole (AQ), a collisional quadrupole (CQ), and a rear hexapole (H2) and a ToF drift tube for mass analysis. [Adapted with permission from Elsevier B. V. Rakov, V. S.; Borisov, O. V.; Whitehouse, C. M. *J. Am. Soc. Mass Spectrom.* (Volume 12, Pages 1794-1809)]

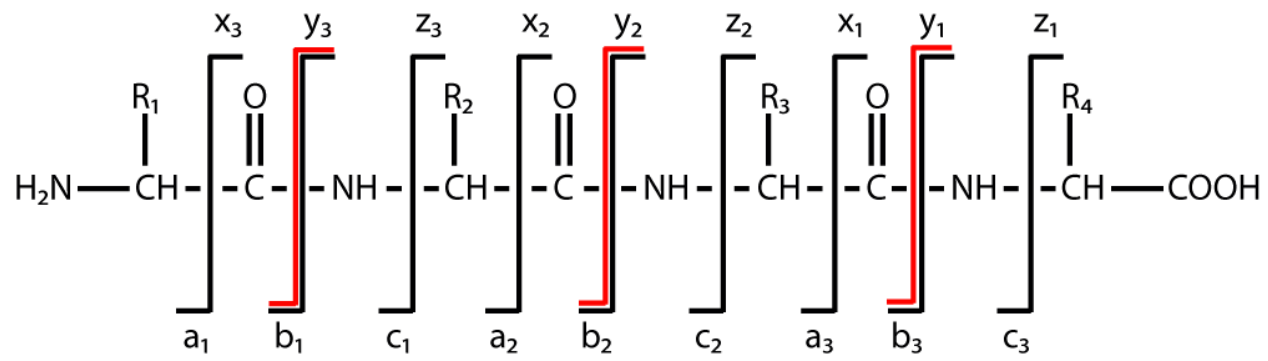


Figure 6-2. Diagram of possible cleavages along a peptide backbone labeled with Roepstorff-Fohlman-Biemann nomenclature. Black lines represent each typical amino acid cleavage point as well as the label associated with the corresponding cleavage. Red lines separate each full amino acid in the sequence.

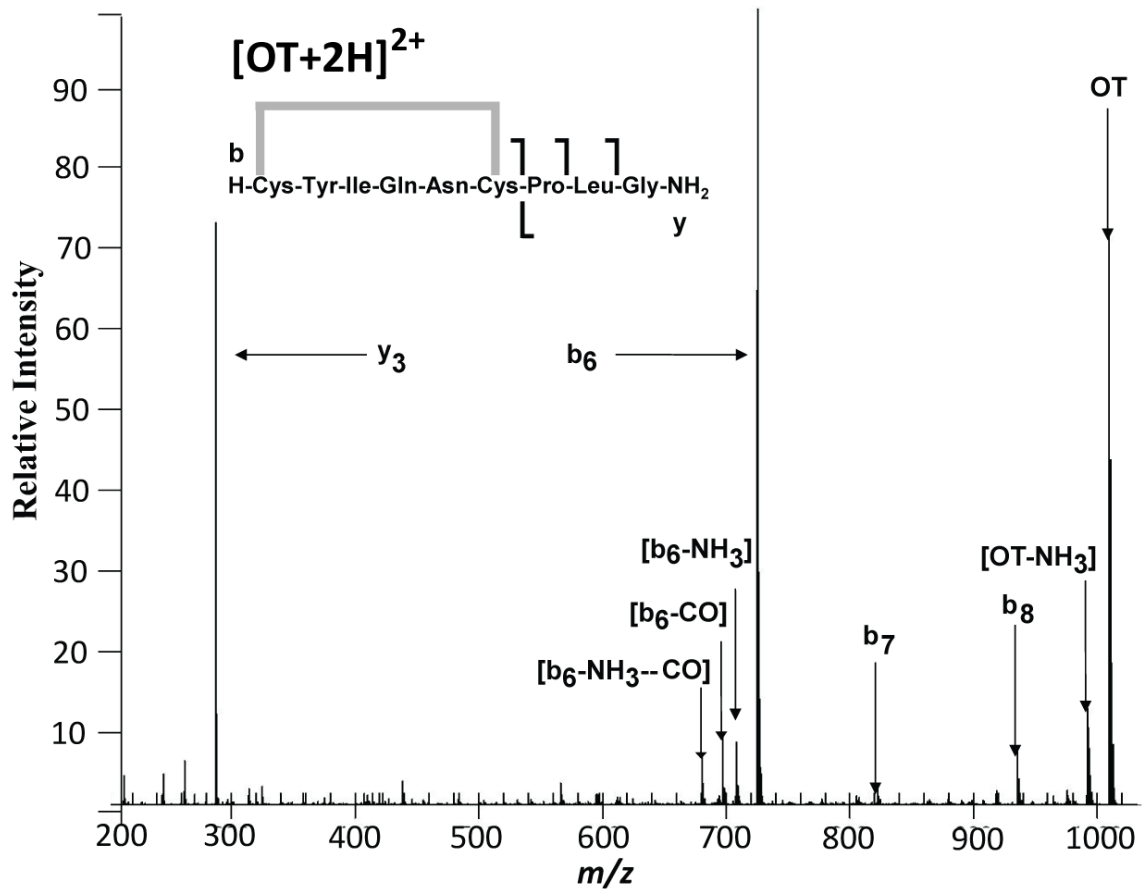


Figure 6-3. Low amplitude multiple resonance excitation CID tandem mass spectrum of $[\text{OT}+2\text{H}]^{2+}$.

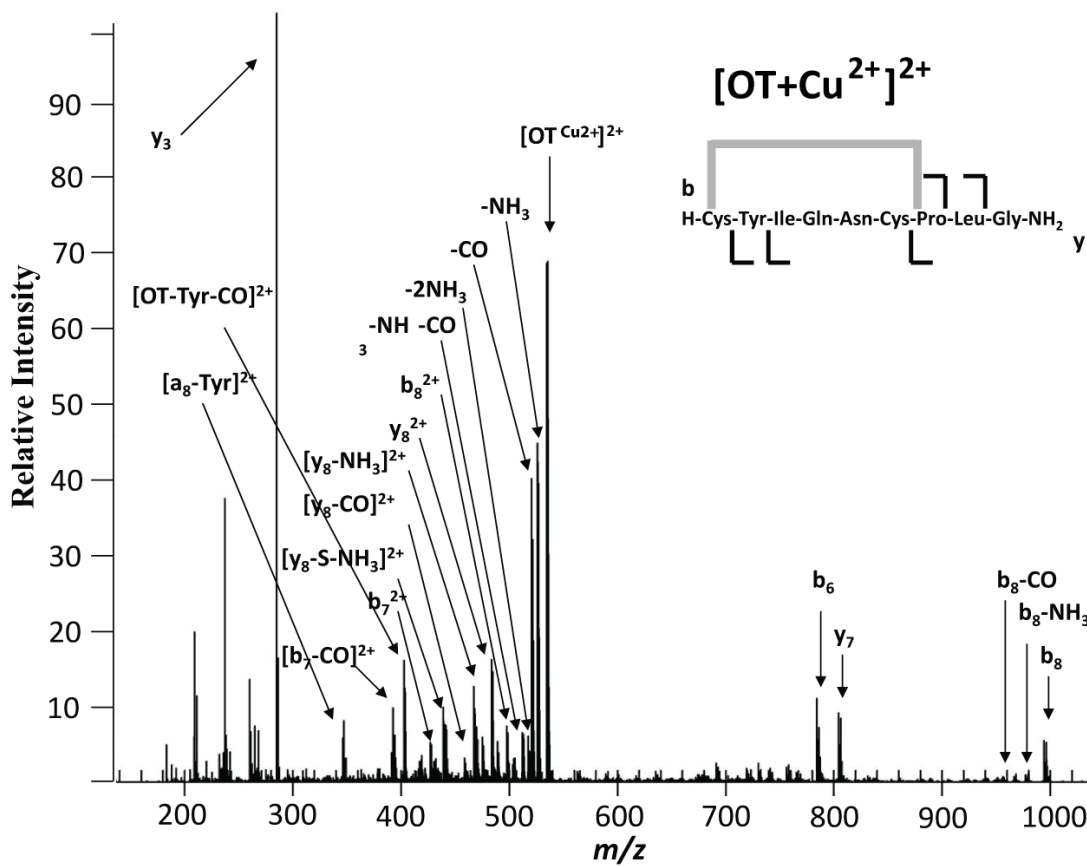


Figure 6-4. Low amplitude multiple resonance excitation CID tandem mass spectrum of $[\text{OT+Cu}^{2+}]^{2+}$.

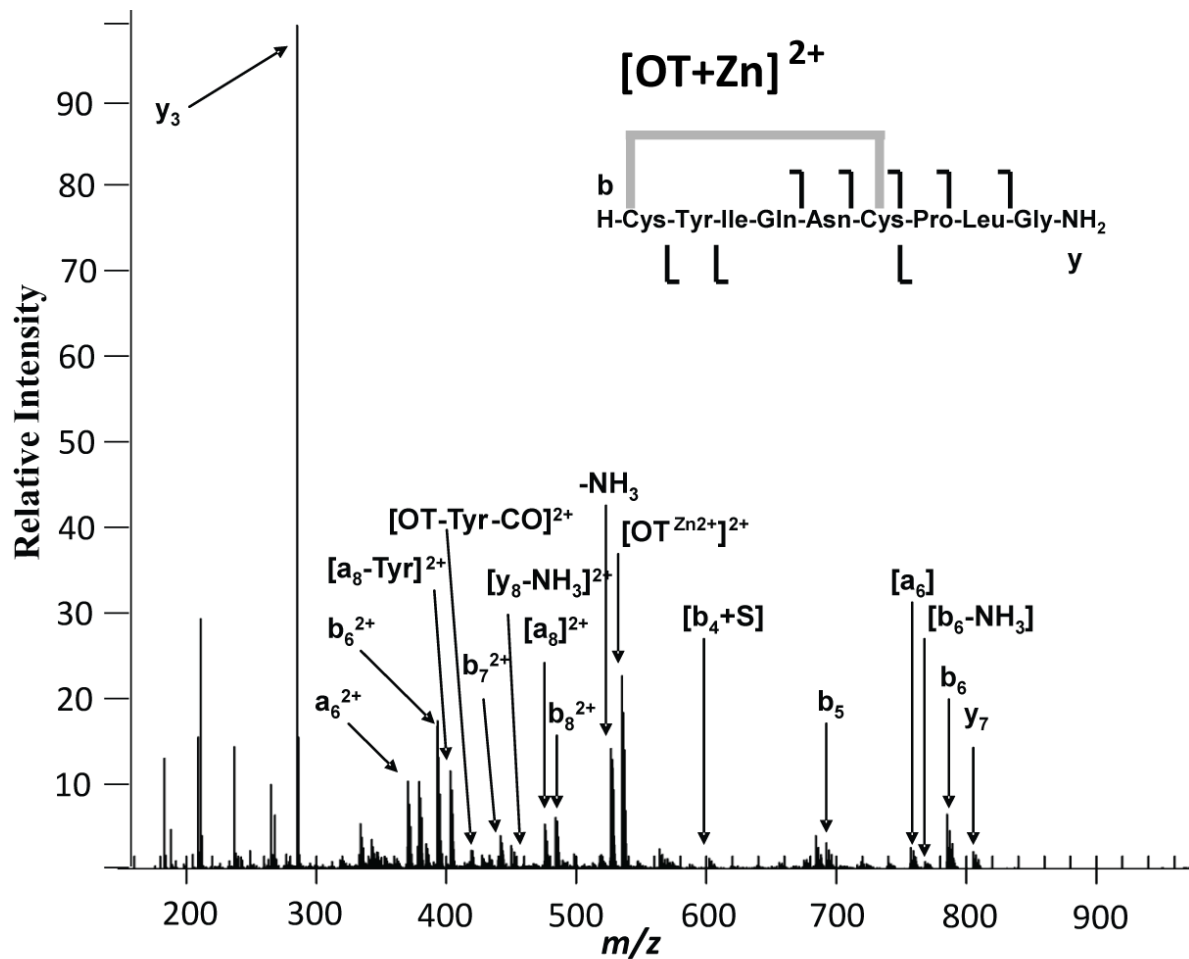


Figure 6-5. Low amplitude multiple resonance excitation CID tandem mass spectrum of $[OT+Zn^{2+}]^{2+}$.

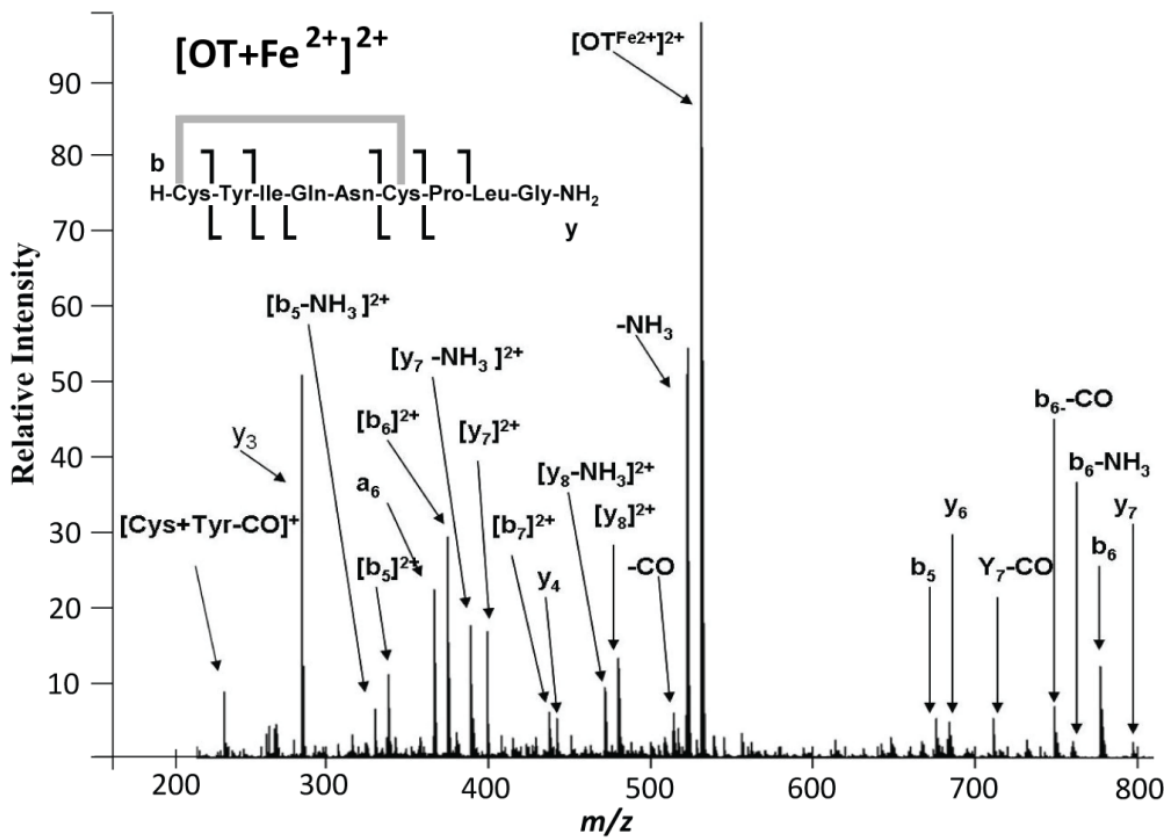


Figure 6-6. Low amplitude multiple resonance excitation CID tandem mass spectrum of $[\text{OT}+\text{Fe}^{2+}]^{2+}$.

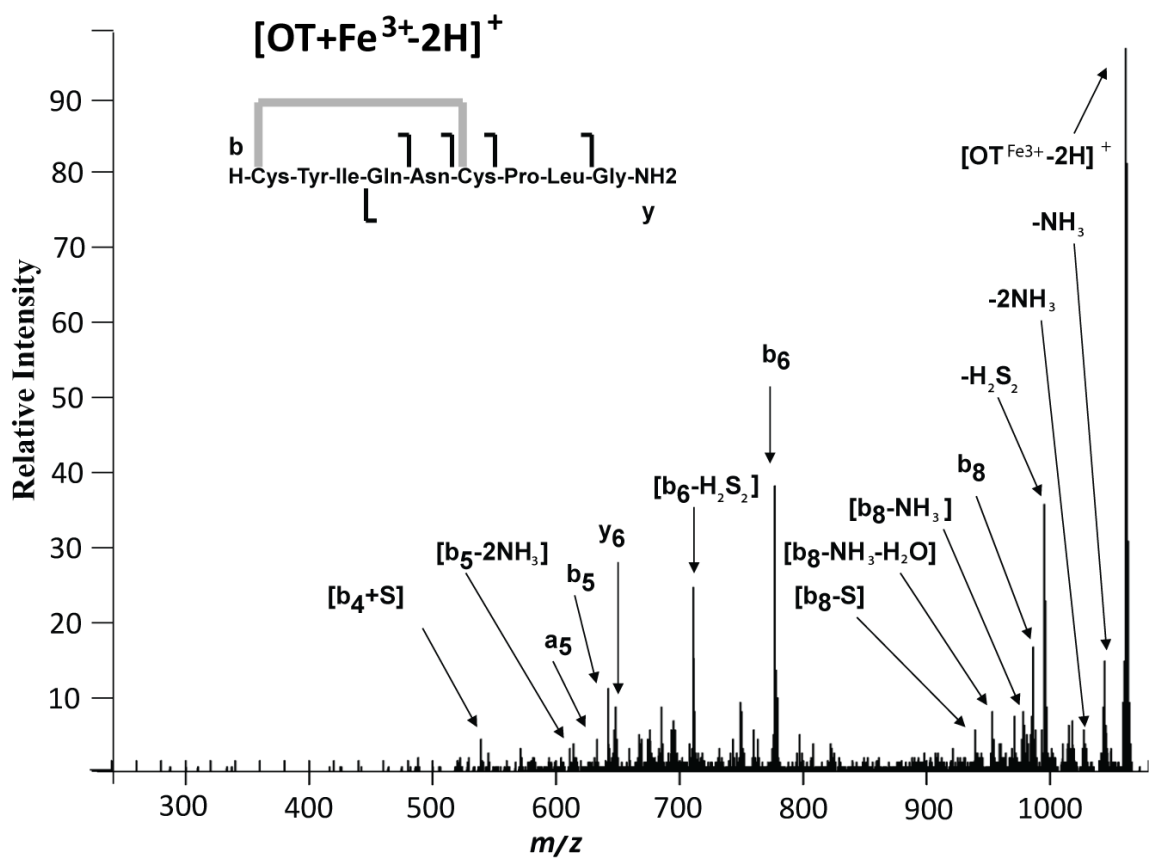


Figure 6-7. Low amplitude multiple resonance excitation CID tandem mass spectrum of $[\text{OT}+\text{Fe}^{3+}-2\text{H}]^+$.

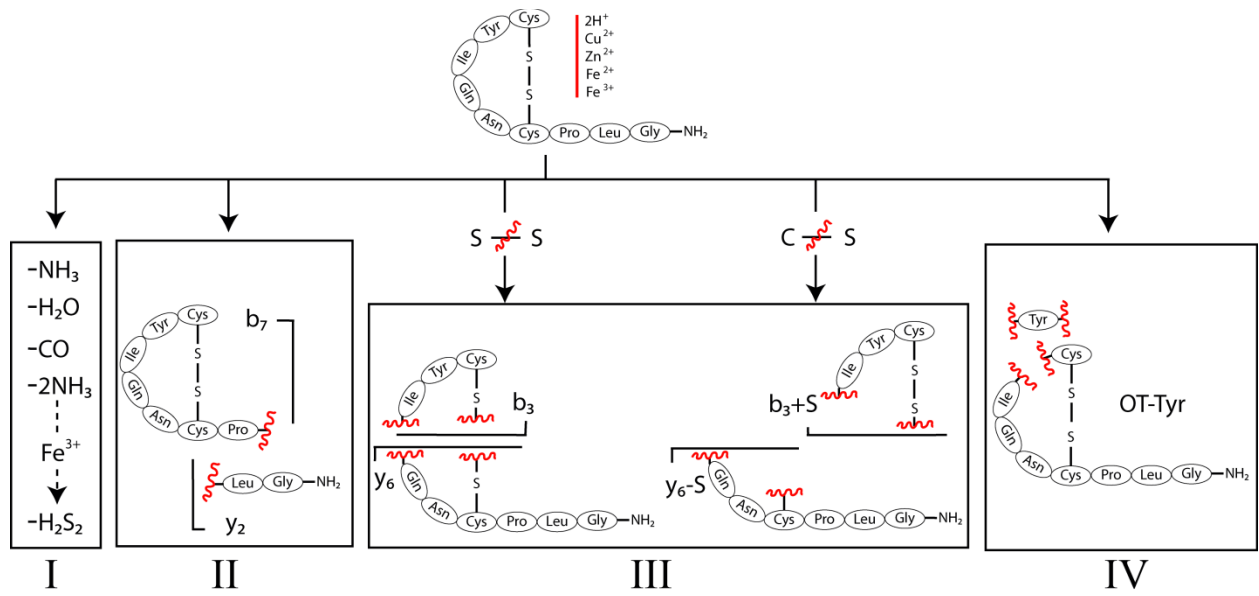


Figure 6-8. An overview of typical fragmentation observed in CID of metal-complexed OT. Note that the sequence of events is chosen arbitrarily and does not indicate order of cleavages. [Adapted with permission from John Wiley & Sons, Ltd. Mihalca, R.; van der Burgt, Y. E. M.; Heck, A. J. R.; Heeren, R. M. A. 2007. Disulfide bond cleavages observed in SORI-CID of three nonapeptides complexed with divalent transition-metal cations. *J. Mass Spectrom.* (Volume 42 Pages 450-458)]

Table 6-1. Relative product ion intensities for the five CID spectra of oxytocin.

Peptide	Assignment fragments (no.)	Assignment fragments (%PII)	1 (neutral loss)	2 (tail b/y)	3 (ring b/y)	4 (internal loss)
$[OT+2H]^{2+}$	16	90%	25%	62%	0%	13%
$[OT+Zn^{2+}]^{2+}$	13	50%	8%	46%	31%	15%
$[OT+Cu^{2+}]^{2+}$	18	72%	22%	33%	28%	17%
$[OT+Fe^{2+}]^{2+}$	23	82%	13%	30%	48%	9%
$[OT+Fe^{3+}]^+$	12	57%	33%	33%	33%	0%

Table 6-2. Relative ion intensities for the five CID spectra of oxytocin

Peptide	Percentage of total ion intensity
$[OT+2H]^{2+}$	39%
$[OT+Zn^{2+}]^{2+}$	33%
$[OT+Cu^{2+}]^{2+}$	16%
$[OT+Fe^{2+}]^{2+}$	10%
$[OT+Fe^{3+}]^+$	2%

CHAPTER 7

CONCLUSIONS AND FUTURE DIRECTIONS

It has been shown that irradiation with the infrared output of the optical parametric oscillator laser is useful for identifying the chemical structures of gas phase analytes. By performing infrared multiple photon dissociation (IRMPD) spectroscopy in the 2900 cm^{-1} – 3700 cm^{-1} region, the presence or absence of diagnostic N-H and O-H peaks offers more chemical information than fragmentation pathways (alone).

Metal-complexed dimers of tryptophan and methionine were investigated for trends in zwitterionic stabilization based on metal size. Opposite trends were found for both systems, which show that multiple factors play a role in favoring gas-phase zwitterions. It is suggested that steric effects can be important, and this might explain the unusual behavior in the tryptophan dimer complexes. The density functional theory calculations qualitatively agree with the experimental spectra and hence confirm ion structures. Nonetheless, the relative energetics are often found to be a poor indicator of which structures are in fact favored.

IRMPD spectroscopy experiments in the Fourier transform ion cyclotron resonance mass spectrometer were limited to more weakly bound species. For protonated tryptophan, many of the lower-frequency bands were not observed. In order to overcome this problem, a custom-built mass spectrometer was utilized, where mass-selected ions are photodissociated in a reduced-pressure (10^{-5} Torr) quadrupole ion trap. The enhanced IRMPD yield is due to the increased photon flux on the ion cloud, as the tightly focused OPO beams were overlapped with a more compact ion cloud. This increase in the IRMPD efficiency is observed despite the higher pressures in the ion trap compared to the Penning trap (10^{-5} Torr versus 10^{-10} Torr).

IRMPD spectroscopy is particularly well suited to confirm the fragmentation chemistry of peptides, on the basis of diagnostic vibrations. By monitoring frequency shifts and comparing experimental spectra with theoretical spectra, for protonated tryptophan, the NH₃ loss channel was confirmed to involve a nucleophilic attack from C3 on the indole side chain, as opposed to nucleophilic attack from C2 or C4. These are the first reported IRMPD spectra of CID products from amino acid/peptide systems. As these experiments are now becoming routine, it is expected that a whole range of CID products from protonated amino acids and peptides can be structurally characterized.

Future experiments should include investigating the CID chemistry of other amino acid systems. Nucleophilic attacks from the aromatic side chain in order to facilitate NH₃ loss may also be involved for phenylalanine or tyrosine. Studying amino acids and small peptides would have the advantage that a database of expected frequencies for vibrational modes could be established. In the long run, this would eliminate the need for detailed quantum-chemical calculations. For the larger peptides, the number of conformations becomes prohibitively large, and hence it would be more useful to focus on diagnostic modes for structural identification.

Another area of gas-phase reaction chemistry pertains to the dissociation chemistry of metal-adducted peptides. Collision induced dissociation of oxytocin had shown that metals can have an effect on the dissociation patterns an ion undergoes. The strong polarizing effect of metals when binding to amino acid or peptide ligands can give rise to more unusual bond cleavages, such as breaking disulfide bonds. IRMPD spectra of such species could for instance confirm the interactions of the metal with the disulfide bond prior to and after bond dissociation.

With respect to larger peptides it is not clear yet what the upper limit in molecular size will be for IRMPD characterization. Due to the higher degrees of freedom of larger molecules and increased collisional cooling rate, this limit may be reached for moderately sized peptides. In this case, other ‘tricks’ may have to be employed, such as using a CO₂ laser for boosting the IRMPD yield, or carrying out a less endothermic reaction than a dissociation, such as a proton transfer reaction to a neutral background molecule.

Although challenges still remain with the technique, such as long analysis times and low sensitivity, IRMPD spectroscopy offers a unique advantage of differentiating isomeric species in a mass spectrometer. The CID product of tryptophan study illustrates the ability of IRMPD spectroscopy to differentiate between several isomer reactants: C2, C3, or C4. Hence, the long term goal of these studies would be to apply IRMPD spectroscopy to elucidate molecular isomer conformation, where information beyond mass is required.

LIST OF REFERENCES

- (1) Zubarev, R. A.; Kelleher, N. L.; McLafferty, F. W. *J. Am. Chem. Soc.* **1998**, *120*, 3265-3266.
- (2) McLafferty, F. W.; Horn, D. M.; Breuker, K.; Ge, Y.; Lewis, M. A.; Cerdá, B.; Zubarev, R. A.; Carpenter, B. K. *J. Am. Soc. Mass Spectrom.* **2001**, *12*, 245-249.
- (3) Syka, J. E. P.; Coon, J. J.; Schroeder, M. J.; Shabanowitz, J.; Hunt, D. F. *Proc. Natl. Acad. Sci. USA* **2004**, *101*, 9528 -9533.
- (4) Mikesh, L. M.; Ueberheide, B.; Chi, A.; Coon, J. J.; Syka, J. E.; Shabanowitz, J.; Hunt, D. F. *Biochim. Biophys. Acta* **2006**, *1764*, 1811-1822.
- (5) McLuckey, S. A.; Stephenson, J. L. *Mass Spectrom. Rev.* **1998**, *17*, 369-407.
- (6) Wells, J. M.; McLuckey, S. A. *Meth. Enzymol.* **2005**, *402*, 148-85.
- (7) Sleno, L.; Volmer, D. A. *J. Mass Spectrom.* **2004**, *39*, 1091-1112.
- (8) Laskin, J.; Futrell, J. H. *Mass Spectrom. Rev.* **2005**, *24*, 135-167.
- (9) Little, D. P.; Speir, J. P.; Senko, M. W.; O'Connor, P. B.; McLafferty, F. W. *Anal. Chem.* **1994**, *66*, 2809-2815.
- (10) Woodin, R. L.; Bomse, D. S.; Beauchamp, J. L. *J. Am. Chem. Soc.* **1978**, *100*, 3248-3250.
- (11) Bagratashvili, V. N.; Letokhov, V. S.; Makarov, A. A.; Ryabov, E. A. *Laser Chem.* **1984**, *5*, 53-105.
- (12) Baykut, G.; Watson, C. H.; Weller, R. R.; Eyler, J. R. *J. Am. Chem. Soc.* **1985**, *107*, 8036-8042.
- (13) Shin, S. K.; Beauchamp, J. L. *J. Am. Chem. Soc.* **1990**, *112*, 2057-2066.
- (14) Atrill, S. R.; Stace, A. J. *Phys. Chem. Chem. Phys.* **2000**, *2*, 823-830.
- (15) Polfer, N. C.; Oomens, J. *Phys. Chem. Chem. Phys.* **2007**, *9*, 3804.
- (16) Garrett, R. H.; Grisham, C. M. *Biochemistry*; 2nd ed.; Saunders College Publishing: Fort Worth, **1999**.
- (17) Domon, B.; Aebersold, R. *Science* **2006**, *312*, 212-217.
- (18) Anderson N. L.; Anderson N.G. *Electrophoresis* **1998**, *19*, 1853–61.

- (19) Blackstock W. P.; Weir M.P. *Trends Biotechnol.* **1999**, *17*, 121–7.
- (20) Edman P. *Acta Chem. Scand.* **1950**, *4*, 283-293.
- (21) Niall H. D. *Meth. Enzymol.* **1973**, *27*, 942–1010.
- (22) Fenn, J.; Mann, M.; Meng, C.; Wong, S.; Whitehouse, C. *Science* **1989**, *246*, 64-71.
- (23) Karas, M.; Hillenkamp, F. *Anal. Chem.* **1988**, *60*, 2299-2301.
- (24) Hillenkamp, F.; Karas, M.; Beavis, R. C.; Brian, T. *Anal. Chem.* **1991**, *63*, 24.
- (25) Steen, H.; Mann, M. *Nat. Rev. Mol. Cell Biol.* **2004**, *5*, 699-711.
- (26) Berthod, A.; Crank, J. A.; Rundlett, K. L.; Armstrong, D. W. *Rapid Commun. Mass Spectrom.* **2009**, *23*, 3409-3422.
- (27) Standing, K. G. *Curr. Opin. Struct. Biol.* **2003**, *13*, 595-601.
- (28) Ge, Y.; Lawhorn, B. G.; ElNaggar, M.; Strauss, E.; Park, J.; Begley, T. P.; McLafferty, F. W. *J. Am. Chem. Soc.* **2002**, *124*, 672-678.
- (29) Horn, D. M.; Zubarev, R. A.; McLafferty, F. W. *Proc. Natl. Acad. Sci. USA* **2000**, *97*, 10313 -10317.
- (30) Ge, Y.; ElNaggar, M.; Sze, S. K.; Oh, H. B.; Begley, T. P.; McLafferty, F. W.; Boshoff, H.; Barry, C. E. *J. Am. Soc. Mass Spectrom.* **2003**, *14*, 253-261.
- (31) Skoog, D. A.; Holler, F. J.; Crouch, S. R. *Instrumental Analysis*; Thomson Brooks/Cole: Belmont, **2007**.
- (32) Loo, J. A.; DeJohn, D. E.; Du, P.; Stevenson, T. I.; Loo, R. R. *Med. Res. Rev.* **1999**, *19*, 307–319.
- (33) Kelleher, N. L. *Chem. Biol.* **2000**, *7*, R37-R45.
- (34) McLafferty, F. W.; Fridriksson, E. K.; Horn, D. M.; Lewis, M. A.; Zubarev, R. A. *Science* **1999**, *284*, 1289–90.
- (35) Fenn, J. B.; Mann, M.; Meng, C. K.; Wong, S. F.; Whitehouse, C. M. *Mass Spectrom. Rev.* **1990**, *9*, 37-70.
- (36) de Hoffmann, E.; Stroobant, V. *Mass Spectrometry: Principles and Applications*; Wiley-Interscience: Toronto, **2005**.

- (37) Rockwood, A. L.; Busman, M.; Udseth, H. R.; Smith, R. D. *Rapid Commun. Mass Spectrom.* **1991**, *5*, 582–585.
- (38) Cech, N. B.; Enke, C. G. *Anal. Chem.* **2001**, *73*, 4632–4639.
- (39) Iribarne, J. V.; Thomson, B. A. *J. Chem. Phys.* **1976**, *64*, 2287.
- (40) de la Mora, J. F.; *Anal. Chim. Acta* **2000**, *406*, 93–104.
- (41) Busch, K. L.; Cooks, R. G.; McLafferty, F. W. *Tandem Mass Spectrometry*; John Wiley: New York **1983**, 11–39.
- (42) Louris, J. N.; Wright, L. G.; Cooks, R. G.; Schoen, A. E. *Anal. Chem.* **1985**, *57*, 2918–2924.
- (43) Basov, N. G.; Markin, E. P.; Oraevskii, A. N.; Pankratov, A. V. *Sov. Phys. Dokl.* **1971**, *16*, 445.
- (44) Woodin, R.; Bomse, D.; Beauchamp, J. *J. Chem. Phys. Lett.* **1979**, *63*, 630-636.
- (45) Bomse, D. S.; Woodin, R. L.; Beauchamp, J. L. *J. Am. Chem. Soc.* **1979**, *101*, 5503–5512.
- (46) Grant, E. R.; Schulz, P. A.; Sudbo, A. S.; Shen, Y. R.; Lee, Y. T. *Phys. Rev. Lett.* **1978**, *40*, 115.
- (47) Lehmann, K. K.; Scoles, G.; Pate, B. H. *Annu. Rev. Phys. Chem.* **1994**, *45*, 241-274.
- (48) Black, J. G.; Yablonovitch, E.; Bloembergen, N.; Mukamel, S. *Phys. Rev. Lett.* **1977**, *38*, 1131.
- (49) Meyer, F. K.; Jasinski, J. M.; Rosenfeld, R. N.; Brauman, J. I. *J. Am. Chem. Soc.* **1982**, *104*, 663-667.
- (50) Peiris, D. M.; Cheeseman, M. A.; Ramanathan, R.; Eyler, J. R. *J. Phys. Chem.* **1993**, *97*, 7839-7843.
- (51) Kirkwood, D. A.; Stace, A. J. *J. Am. Chem. Soc.* **1998**, *120*, 12316-12326.
- (52) Valle, J. J.; Eyler, J. R.; Oomens, J.; Moore, D. T.; van der Meer, A. F. G.; von Helden, G.; Meijer, G.; Hendrickson, C. L.; Marshall, A. G.; Blakney, G. T. *Rev. Sci. Instrum.* **2005**, *76*, 023103.
- (53) Eyler, J. R. *Mass Spectrom. Rev.* **2009**, *28*, 448-467.
- (54) Lawrence, E. O.; Livingston, M. S. *Phys. Rev.* **1932**, *40*, 19.

- (55) Sommer, H.; Thomas, H. A.; Hipple, J. A. *Phys. Rev.* **1951**, *82*, 697.
- (56) Wobschall, D. *Rev. Sci. Instrum.* **1965**, *36*, 466.
- (57) Cooley, J. W.; Tukey, J. W. *Math. Comp.* **1965**, *19*, 297-301.
- (58) Comisarow, M. B.; Marshall, A. G. *Chem. Phys. Lett.* **1974**, *26*, 489-490.
- (59) Marshall, A. G.; Comisarow, M. B.; Parisod, G. *J. Chem. Phys.* **1979**, *71*, 4434.
- (60) Marshall, A. G.; Hendrickson, C. L.; Jackson, G. S. *Mass Spectrom. Rev.* **1998**, *17*, 1-35.
- (61) Noest, A.; Kort, C. *Comput. Chem.* **1983**, *7*, 81-86.
- (62) Schweikhard, L.; Marshall, A. G. *J. Am. Soc. Mass Spectrom.* **1993**, *4*, 433-452.
- (63) Dehmelt, H. *Rev. Mod. Phys.* **1990**, *62*, 525.
- (64) Amster, J. I. *J. Mass Spectrom.* **1996**, *31*, 1325-1337.
- (65) Ledford, E. B.; Rempel, D. L.; Gross, M. L. *Anal. Chem.* **1984**, *56*, 2744-2748.
- (66) Jeffries, J.; Barlow, S.; Dunn, G. *Int. J. Mass Spectrom. Ion Process.* **1983**, *54*, 169-187.
- (67) Schaub, T. M.; Hendrickson, C. L.; Horning, S.; Quinn, J. P.; Senko, M. W.; Marshall, A. G. *Anal. Chem.* **2008**, *80*, 3985-3990.
- (68) Paul, D. W.; Steinwedel, D. H. Apparatus for separating charged particles of different specific charges. German patent 944,900 **1956**; U.S. patent 2,939,952 **1960**.
- (69) McLachlan, N. W.; McLachlan, N. W. *Theory and Application of Mathieu Functions*; Dover: New York, **1962**.
- (70) Dawson, P. H. *Mass Spectrom. Rev.* **1986**, *5*, 1-37.
- (71) Welling, M.; Schuessler, H. A.; Thompson, R. I.; Walther, H. *Int. J. Mass Spectrom. Ion Process.* **1998**, *172*, 95-114.
- (72) Paul, W.; Steinwedel, H. *Z. Naturforsch. Teil A* **1953**, *8*, 448-450.
- (73) March, R. E.; Hughes, R. J. *Quadrupole Storage Mass Spectrometry*; John Wiley: New York, **1989**.
- (74) March, R. E. *Rapid Commun. Mass Spectrom.* **1998**, *12*, 1543-1554.

- (75) March, R. E. *Int. J. Mass Spectrom.* **2000**, *200*, 285-312.
- (76) Yoshinari, K. *Rapid Commun. Mass Spectrom.* **2000**, *14*, 215-223.
- (77) March, R. E.; Todd, J. F. J. *Practical Aspects of Ion Trap Mass Spectrometry: Chemical, Environmental, and Biomedical Applications*; CRC Press: Boca Raton **1995**.
- (78) Stephens, W. E. *Phys. Rev.* **1946**, *69*, 691.
- (79) Gohlke, R. S. *Anal. Chem.* **1959**, *31*, 535-541.
- (80) Gohlke, R. S.; McLafferty, F. W. *J. Am. Soc. Mass Spectrom.* **1993**, *4*, 367-371.
- (81) Franken, P. A.; Hill, A. E.; Peters, C. W.; Weinreich, G. *Phys. Rev. Lett.* **1961**, *7*, 118.
- (82) Kingston, R. H. *Proc. IRE* **1962**, *50*, 472.
- (83) Moeller, G.; Rigden, J. D. *Appl. Phys. Lett.* **1965**, *7*, 274-276.
- (84) Witteman, W. *Quantum Electron.* **1969**, *5*, 92-97.
- (85) Kroll, N. M. *Phys. Rev.* **1962**, *127*, 1207-1211.
- (86) Akhmanov, S. A.; Khokhlov, R. V. *J. Expt. Theor. Phys.* **1963**, *16*, 252-254.
- (87) Wang, C. C.; Racette, G. W. *Appl. Phys. Lett.* **1965**, *6*, 169-171.
- (88) Giordmaine, J. A.; Miller, R. C. *Phys. Rev. Lett.* **1965**, *14*, 973-976.
- (89) Yang, S. T.; Eckardt, R. C.; Byer, R. L. *J. Opt. Soc. Am. B* **1993**, *10*, 1684-1695.
- (90) Eckardt, R. C.; Nabors, C. D.; Kozlovsky, W. J.; Byer, R. L. *J. Opt. Soc. Am. B* **1991**, *8*, 646-667.
- (91) Gale, G. M.; Cavallari, M.; Hache, F. *J. Opt. Soc. Am. B* **1998**, *15*, 702-714.
- (92) Butterworth, S. D.; Girard, S.; Hanna, D. C. *J. Opt. Soc. Am. B* **1995**, *12*, 2158-2167.
- (93) Bosenberg, W. R.; Drobshoff, A.; Alexander, J. I.; Myers, L. E.; Byer, R. L. *Opt. Lett.* **1996**, *21*, 713-715.
- (94) Arbore, M. A.; Fejer, M. M. *Opt. Lett.* **1997**, *22*, 151-153.
- (95) Batchko, R. G.; Weise, D. R.; Plettner, T.; Miller, G. D.; Fejer, M. M.; Byer, R. L. *Opt. Lett.* **1998**, *23*, 168-170.

- (96) Dunn, M. H.; Ebrahimzadeh, M. *Science* **1999**, 286, 1513-1517.
- (97) Lefort, L.; Puech, K.; Butterworth, S. D.; Svirko, Y. P.; Hanna, D. C. *Opt. Lett.* **1999**, 24, 28-30.
- (98) Mueller, F. 4000 Operating Manual **2007**.
- (99) Harris, S. *Proc. IEEE* **1969**, 57, 2096-2113.
- (100) Maiman, T. H. *Nature* **1960**, 187, 493-494.
- (101) Boyd, R. W. *Nonlinear Optics*; Academic Press: New York, 1992.
- (102) Myers, L. E.; Eckardt, R. C.; Fejer, M. M.; Byer, R. L.; Bosenberg, W. R.; Pierce, J. W. *J. Opt. Soc. Am. B* **1995**, 12, 2102-2116.
- (103) Myers, L. E.; Miller, G. D.; Eckardt, R. C.; Fejer, M. M.; Byer, R. L.; Bosenberg, W. R. *Opt. Lett.* **1995**, 20, 52-54.
- (104) Bloembergen, N. *Appl. Phys. Lett.* **1970**, 17, 483-486.
- (105) Fejer, M.; Magel, G.; Jundt, D.; Byer, R. *Quantum Electron.* **1992**, 28, 2631-2654.
- (106) Laurell, F. *Opt. Mater.* **1999**, 11, 235-244.
- (107) Pound, R. V. *Rev. Sci. Instrum.* **1946**, 17, 490-506.
- (108) Drever, R. W. P.; Hall, J. L.; Kowalski, F. V.; Hough, J.; Ford, G. M.; Munley, A. J.; Ward, H. *Appl. Phys. B* **1983**, 31, 97-105.
- (109) Wallace, B. A. *BioEssays* **2000**, 22, 227-234.
- (110) Doyle, D. A.; Cabral, J. M.; Pfuetzner, R. A.; Kuo, A.; Gulbis, J. M.; Cohen, S. L.; Chait, B. T.; MacKinnon, R. *Science* **1998**, 280, 69-78.
- (111) Venkataraman, P.; Lamb, R. A.; Pinto, L. H. *J. Biol. Chem.* **2005**, 280, 21463-21472.
- (112) Cotten, M.; Tian, C.; Busath, D. D.; Shirts, R. B.; Cross, T. A. *Biochemistry* **1999**, 38, 9185-9197.
- (113) Hu, W.; Cross, T. A. *Biochemistry* **1995**, 34, 14147-14155.
- (114) Buck, D. *Biophys. J.* **2000**, 79, 2454-2462.
- (115) Dunbar, R. C.; Steill, J. D.; Polfer, N. C.; Oomens, J. *J.Phys. Chem. A* **2009**, 113, 845-851.

- (116) Oomens, J.; Sartakov, B. G.; Meijer, G.; von Helden, G. *Int. J. Mass Spectrom.* **2006**, 254, 1-19.
- (117) Polfer, N. C.; Oomens, J. *Mass Spectrom. Rev.* **2009**, 28, 468-494
- (118) Fridgen, T. D. *Mass Spectrom. Rev.* **2009**, 28, 586-607.
- (119) Schäfer, M.; Drayss, M. K.; Blunk, D.; Purcell, J. M.; Hendrickson, C. L.; Marshall, A. G.; Mookherjee, A.; Armentrout, P. B. *J. Phys. Chem. A* **2009**, 113, 7779-7783.
- (120) Kapota, C.; Lemaire, J.; Maitre, P.; Ohanessian, G. *J. Am. Chem. Soc.* **2004**, 126, 1836-1842.
- (121) Jockusch, R. A.; Price, W. D.; Williams, E. R. *J. Phys. Chem. A* **1999**, 103, 9266-9274.
- (122) Polfer, N. C.; Oomens, J.; Moore, D. T.; von Helden, G.; Meijer, G.; Dunbar, R. C. *J. Am. Chem. Soc.* **2006**, 128, 517-525.
- (123) Polfer, N. C.; Oomens, J.; Dunbar, R. C. *Phys. Chem. Chem. Phys.* **2006**, 8, 2744-2751.
- (124) Talley, J. M.; Cerda, B. A.; Ohanessian, G.; Wesdemiotis, C. *Chem. Eur. J.* **2002**, 8, 1377-1388.
- (125) Forbes, M. W.; Bush, M. F.; Polfer, N. C.; Oomens, J.; Dunbar, R. C.; Williams, E. R.; Jockusch, R. A. *J. Phys. Chem. A* **2007**, 111, 11759-11770.
- (126) Polfer, N. C.; Paizs, B.; Snoek, L. C.; Compagnon, I.; Suhai, S.; Meijer, G.; von Helden, G.; Oomens, J. *J. Am. Chem. Soc.* **2005**, 127, 8571-8579.
- (127) Kish, M. M.; Ohanessian, G.; Wesdemiotis, C. *Int. J. Mass Spectrom.* **2003**, 227, 509-524.
- (128) Marino, T.; Russo, N.; Toscano, M. *J. Phys. Chem. B* **2003**, 107, 2588-2594.
- (129) Shoeib, T.; Siu, K. W. M.; Hopkinson, A. C. *J. Phys. Chem. A* **2002**, 106, 6121-6128.
- (130) Lemoff, A. S.; Bush, M. F.; Williams, E. R. *J. Phys. Chem. A* **2005**, 109, 1903-1910.
- (131) Lemoff, A. S.; Bush, M. F.; Wu, C.; Williams, E. R. *J. Am. Chem. Soc.* **2005**, 127, 10276-10286.
- (132) Cerda, B. A.; Wesdemiotis, C. *Int. J. Mass Spectrom.* **1999**, 185-187, 107-116.
- (133) Lesarri, A.; Cocinero, E. J.; López, J. C.; Alonso, J. L. *Angew. Chem. Int. Ed.* **2004**, 43, 605-610.

- (134) Armentrout, P. B.; Rodgers, M. T.; Oomens, J.; Steill, J. D. *J. Phys. Chem. A* **2008**, *112*, 2248-2257.
- (135) Rodgers, M. T.; Armentrout, P. B.; Oomens, J.; Steill, J. D. *J. Phys. Chem. A* **2008**, *112*, 2258-2267.
- (136) Bush, M. F.; O'Brien, J. T.; Prell, J. S.; Saykally, R. J.; Williams, E. R. *J. Am. Chem. Soc.* **2007**, *129*, 1612-1622.
- (137) Bush, M. F.; Prell, J. S.; Saykally, R. J.; Williams, E. R. *J. Am. Chem. Soc.* **2007**, *129*, 13544-13553.
- (138) Bush, M. F.; Oomens, J.; Williams, E. R. *J. Phys. Chem. A* **2009**, *113*, 431-438.
- (139) Carl, D. R.; Cooper, T. E.; Oomens, J.; Steill, J. D.; Armentrout, P. B. *Phys. Chem. Chem. Phys.* **2010**, *12*, 3384-3398.
- (140) Dunbar, R. C.; Polfer, N. C.; Oomens, J. *J. Am. Chem. Soc.* **2007**, *129*, 14562-14563.
- (141) Bush, M. F.; Oomens, J.; Saykally, R. J.; Williams, E. R. *J. Phys. Chem. A* **2008**, *112*, 8578-8584.
- (142) Armentrout, P. B.; Gabriel, A.; Moision, R. M. *Int. J. Mass Spectrom.* **2009**, *283*, 56-68.
- (143) Bush, M. F.; Oomens, J.; Saykally, R. J.; Williams, E. R. *J. Am. Chem. Soc.* **2008**, *130*, 6463-6471.
- (144) Oh, H.; Lin, C.; Hwang, H. Y.; Zhai, H.; Breuker, K.; Zabrouskov, V.; Carpenter, B. K.; McLafferty, F. W. *J. Am. Chem. Soc.* **2005**, *127*, 4076-4083.
- (145) Kong, X.; Tsai, I.; Sabu, S.; Han, C.; Lee, Y. T.; Chang, H.; Tu, S.; Kung, A. H.; Wu, C. *Angew. Chem. Int. Ed.* **2006**, *45*, 4130-4134.
- (146) Roscioli, J. R.; McCunn, L. R.; Johnson, M. A. *Science* **2007**, *316*, 249-254.
- (147) Headrick, J. M. *Science* **2005**, *308*, 1765-1769.
- (148) Walters, R. S.; Jaeger, T. D.; Duncan, M. A. *J. Phys. Chem. A* **2002**, *106*, 10482-10487.
- (149) Duncan, M. A. *Int. J. Mass Spectrom.* **2008**, *272*, 99-118.
- (150) Lisy J. M. *Int. Rev. Phys. Chem.* **1997**, *16*, 267-289.
- (151) Lisy, J. M. *J. Chem. Phys.* **2006**, *125*, 132302-132321.

- (152) Goebbert, D. J.; Wende, T.; Bergmann, R.; Meijer, G.; Asmis, K. R. *J. Phys. Chem. A* **2009**, *113*, 5874-5880.
- (153) O'Brien, J. T.; Prell, J. S.; Steill, J. D.; Oomens, J.; Williams, E. R. *J. Am. Chem. Soc.* **2009**, *131*, 3905-3912.
- (154) Rizzo, T.; Stearns, J.; Boyarkin, O. *Int. Revs. Phys. Chem.* **2009**, *28*, 481-515.
- (155) Cagmat, E. B.; Szczepanski, J.; Pearson, W. L.; Powell, D. H.; Eyler, J. R.; Polfer, N. C. *Phys. Chem. Chem. Phys.* **2010**, *12*, 3474-3479.
- (156) Yeh, L. I.; Price, J. M.; Lee, Y. T. *J. Am. Chem. Soc.* **1989**, *111*, 5597-5604.
- (157) Peiris, D. M.; Cheeseman, M. A.; Ramanathan, R.; Eyler, J. R. *J. Phys. Chem.* **1993**, *97*, 7839-7843.
- (158) Frisch, M.; Trucks, G.; Schlegel, H.; Scuseria, G.; Robb, M.; Cheeseman, J.; Montgomery, J.; Vreven, T.; Kudin, K.; Burant, J.; Millam, J.; Iyengar, S.; Tomasi, J.; Barone, V.; Mennucci, B.; Cossi, M.; Scalmani, G.; Rega, N.; Petersson, G.; Nakatsuji, H.; Hada, M.; Ehara, M.; Toyota, K.; Fukuda, R.; Hasegawa, J.; Ishida, M.; Nakajima, T.; Honda, Y.; Kitao, O.; Nakai, H.; Klene, M.; Li, X.; Knox, J.; Hratchian, H.; Cross, J.; Bakken, V.; Adamo, C.; Jaramillo, J.; Gomperts, R.; Stratmann, R.; Yazyev, O.; Austin, A.; Cammi, R.; Pomelli, C.; Ochterski, J.; Ayala, P.; Morokuma, K.; Voth, G.; Salvador, P.; Dannenberg, J.; Zakrzewski, V.; Dapprich, S.; Daniels, A.; Strain, M.; Farkas, O.; Malick, D.; Rabuck, A.; Raghavachari, K.; Foresman, J.; Ortiz, J.; Cui, Q.; Baboul, A.; Clifford, S.; Cioslowski, J.; Stefanov, B.; Liu, G.; Liashenko, A.; Piskorz, P.; Komaromi, I.; Martin, R.; Fox, D.; Keith, T.; Al-Laham, M.; Peng, C.; Nanayakkara, A.; Challacombe, M.; Gill, P.; Johnson, B.; Chen, W.; Wong, M.; Gonzalez, C.; Pople, J. *Gaussian 03, Revision B.03; Gaussian, Inc.: Wallingford, CT 06492 USA*, **2004**.
- (159) Hu, P.; Loo, J. A. *J. Am. Chem. Soc.* **1995**, *117*, 11314-11319.
- (160) Chen, H.; Xu, R.; Chen, H.; Cooks, R. G.; Ouyang, Z. *J. Mass Spectrom.* **2005**, *40*, 1403-1411.
- (161) Blades, A. T.; Jayaweera, P.; Ikonomou, M. G.; Kebarle, P. *Int. J. Mass Spectrom. Ion Process.* **1990**, *101*, 325-336.
- (162) Tsierkezos, N. G.; Schröder, D.; Schwarz, H. *Int. J. Mass Spectrom.* **2004**, *235*, 33-42.
- (163) Beyer, M.; Williams, E. R.; Bondybey, V. E. *J. Am. Chem. Soc.* **1999**, *121*, 1565-1573.
- (164) Drayß, M. K.; Armentrout, P.; Oomens, J.; Schäfer, M. *Int. J. Mass Spectrom.* **2010**, *297*, 18-27.
- (165) Schweet, R.; Heintz, R. *Annu. Rev. Biochem.* **1966**, *35*, 723-758.

- (166) Webster, L. T. *J. Biol. Chem.* **1966**, *241*, 5504 -5510.
- (167) Schoner, W. *Angew. Chem. Int. Ed. Engl.* **1971**, *10*, 882-889.
- (168) Taylor, E. W. *Annu. Rev. Biochem.* **1972**, *41*, 577-616.
- (169) Morrison, J. F.; Heyde, E. *Annu. Rev. Biochem.* **1972**, *41*, 29-54.
- (170) Walsh, M.; Stevens, F. C. *Biochemistry* **1977**, *16*, 2742-2749.
- (171) Rüdiger, H. *FEBS Lett.* **1973**, *35*, 295-298.
- (172) Maître, P.; Le Caér, S.; Simon, A.; Jones, W.; Lemaire, J.; Mestdagh, H.; Heninger, M.; Mauclaire, G.; Boissel, P.; Prazeres, R.; Glotin, F.; Ortega, J. *Nucl. Instrum. Meth. A* **2003**, *507*, 541-546.
- (173) Oh, H.; Breuker, K.; Sze, S. K.; Ge, Y.; Carpenter, B. K.; McLafferty, F. W. *P. Natl. Acad. Sci. USA* **2002**, *99*, 15863-15868.
- (174) Chen, X.; Yu, L.; Steill, J. D.; Oomens, J.; Polfer, N. C. *J. Am. Chem. Soc.* **2009**, *131*, 18272-18282.
- (175) Chen, X.; Steill, J. D.; Oomens, J.; Polfer, N. C. *J. Am. Soc. Mass Spectrom.* **2010**, *21*, 1313-1321.
- (176) Lemoff, A. S.; Bush, M. F.; Williams, E. R. *J. Am. Chem. Soc.* **2003**, *125*, 13576-13584.
- (177) Rajabi, K.; Fridgen, T. D. *J. Phys. Chem. A* **2008**, *112*, 23-30.
- (178) Wu, R.; McMahon, T. B. *J. Am. Chem. Soc.* **2007**, *129*, 4864-4865.
- (179) Mino Jr., W. K.; Szczepanski, J.; Pearson, W. L.; Powell, D. H.; Dunbar, R. C.; Eyler, J. R.; Polfer, N. C. *Int. J. Mass Spectrom.* **2010**, *297*, 131-138.
- (180) Allouche, A. R. *J. Comput. Chem.* **2011**, *32*, 174–182.
- (181) Merrick, J. P.; Moran, D.; Radom, L. *J. Phys. Chem. A* **2007**, *111*, 11683-11700.
- (182) Brodbelt, J. S.; Wilson, J. J. *Mass Spectrom. Rev.* **2009**, *28*, 390-424.
- (183) Polfer, N. C.; Oomens, J.; Suhai, S.; Paizs, B. *J. Am. Chem. Soc.* **2007**, *129*, 5887-5897.
- (184) Oomens, J.; Young, S.; Molesworth, S.; van Stipdonk, M. *J. Am. Soc. Mass Spectrom.* **2009**, *20*, 334-339.

- (185) Perkins, B. R.; Chamot-Rooke, J.; Yoon, S. H.; Gucinski, A. C.; Somogyi, A.; Wysocki, V. H. *J. Am. Chem. Soc.* **2009**, *131*, 17528-17529.
- (186) Bythell, B. J.; Erlekam, U.; Paizs, B.; Maître, P. *Chem. Phys. Chem.* **2009**, *10*, 883-885.
- (187) Nicely, A. L.; Miller, D. J.; Lisy, J. M. *J. Am. Chem. Soc.* **2009**, *131*, 6314-6315.
- (188) Dahl, D. A. *Int. J. Mass Spectrom.* **2000**, *200*, 3-25.
- (189) Lioe, H.; O'Hair, R. A. J.; Reid, G. E. *J. Am. Soc. Mass Spectrom.* **2004**, *15*, 65-76.
- (190) El Aribi, H.; Orlova, G.; Hopkinson, A. C.; Siu, K. W. M. *J. Phys. Chem. A* **2004**, *108*, 3844-3853.
- (191) Rakov, V. S.; Borisov, O. V.; Whitehouse, C. M. *J. Am. Soc. Mass Spectrom.* **2004**, *15*, 1794-1809.
- (192) Gauthier, J. W.; Trautman, T. R.; Jacobson, D. B. *Anal. Chim. Acta* **1991**, *246*, 211-225.
- (193) Katritzky, A. R.; Watson, C. H.; Dega-Szafran, Z.; Eyler, J. R. *Org. Mass Spectrom.* **1989**, *24*, 1017-1021.
- (194) Dunbar, R. C.; Zaniewski, R. C. *J. Chem. Phys.* **1992**, *96*, 5069.
- (195) Freitas, M. A.; Hendrickson, C. L.; Marshall, A. G. *Rapid Commun. Mass Spectrom.* **1999**, *13*, 1639-1642.
- (196) Dunbar, R. C.; McMahon, T. B.; Thoelmann, D.; Tonner, D. S.; Salahub, D. R.; Wei, D. *J. Am. Chem. Soc.* **1995**, *117*, 12819-12825.
- (197) Laskin, J.; Denisov, E.; Futrell, J. H. *Int. J. Mass Spectrom.* **2002**, *219*, 189-201.
- (198) Laskin, J.; Futrell, J. H. *Mass Spectrom. Rev.* **2003**, *22*, 158-181.
- (199) Laskin, J.; Futrell, J. H. *J. Am. Soc. Mass Spectrom.* **2003**, *14*, 1340-1347.
- (200) Williams, E. R.; Henry, K. D.; McLafferty, F. W.; Shabanowitz, J.; Hunt, D. F. *J. Am. Soc. Mass Spectrom.* **1990**, *1*, 413-416.
- (201) Creighton, T. E. *Bioessays* **1988**, *8*, 57-63.
- (202) Mirgorodskaya, E.; O'Connor, P. B.; Costello, C. E. *J. Am. Soc. Mass Spectrom.* **2002**, *13*, 318-324.
- (203) Wells, J. M.; Stephenson, J. L.; McLuckey, S. A. *Int. J. Mass Spectrom.* **2000**, *203*, A1-A9.

- (204) Mihalca, R.; van der Burgt, Y. E. M.; Heck, A. J. R.; Heeren, R. M. A. *J. Mass Spectrom.* **2007**, *42*, 450-458.
- (205) Barberis, C.; Tribollet, E. *Crit. Rev. Neurobiol.* **1996**, *10*, 119-154.
- (206) Liu, D.; Seuthe, A. B.; Ehrler, O. T.; Zhang, X.; Wyttenbach, T.; Hsu, J. F.; Bowers, M. T. *J. Am. Chem. Soc.* **2005**, *127*, 2024-2025.
- (207) Rakov, V. S.; Whitehouse, C. M. *Eur. J. Mass Spectrom.* **2004**, *10*, 173-186.
- (208) Analytica of Branford Corsair MS and Avitor Software Manual **2003**.
- (209) Roepstorff, P.; Fohlman, J. *Biomed. Mass Spectrom.* **1984**, *11*, 601.
- (210) Biemann, K. *Annu. Rev. Biochem.* **1992**, *61*, 977-1010.

BIOGRAPHICAL SKETCH

Warren Karl Mino, Jr. was born in New Hyde Park, New York to Warren K. Mino, Sr. and Patricia Ann Mino. The oldest of four children, he grew up in Glen Head, NY until he was 12. His family moved to Salt Lake City, UT where he spent three years of his life, until he moved with his family back to the east coast, and settled in Brookfield, CT. He finished his secondary education at Brookfield High School. He then attended the University of Connecticut and graduated with a Bachelor of Science in chemistry. It was during his career at the University of Connecticut that he gained an interest in chemistry by working on a project to develop commercial-grade electrochromic goggles. His interest in chemistry led him to pursue a Doctorate of Philosophy in Chemistry at the University of Florida, focusing on mass spectrometric instrumentation and infrared multiple photon dissociation spectroscopy method development. He received his Doctor of Philosophy degree from the University of Florida in May 2011.